Mechanistic studies on the OH-initiated atmospheric oxidation of selected aromatic hydrocarbons

Sascha Nehr

Member of the Helmholtz Association

JÜLICH
FORSCHUNGSZENTRUM

Schriften des Forschungszentrums Jülich
Reihe Energie & Umwelt / Energy & Environment Band / Volume 145

Forschungszentrum Jülich GmbH
Institute of Energy and Climate Research (IEK)
Troposphere (IEK-8)

Mechanistic studies on the OH-initiated atmospheric oxidation of selected aromatic hydrocarbons

Sascha Nehr

Schriften des Forschungszentrums Jülich
Reihe Energie & Umwelt / Energy & Environment Band / Volume 145

ISSN 1866-1793 ISBN 978-3-89336-804-4

Bibliographic information published by the Deutsche Nationalbibliothek.
The Deutsche Nationalbibliothek lists this publication in the Deutsche Nationalbibliografie; detailed bibliographic data are available in the Internet at http://dnb.d-nb.de.

Publisher and Distributor:	Forschungszentrum Jülich GmbH Zentralbibliothek 52425 Jülich Phone +49 (0) 24 61 61-53 68 · Fax +49 (0) 24 61 61-61 03 e-mail: zb-publikation@fz-juelich.de Internet: http://www.fz-juelich.de/zb
Cover Design:	Grafische Medien, Forschungszentrum Jülich GmbH
Printer:	Grafische Medien, Forschungszentrum Jülich GmbH
Copyright:	Forschungszentrum Jülich 2012

Schriften des Forschungszentrums Jülich
Reihe Energie & Umwelt / Energy & Environment Band / Volume 145

D 468 (Diss., Wuppertal, Univ., 2012)

ISSN 1866-1793
ISBN 978-3-89336-804-4

The complete volume is freely available on the Internet on the Jülicher Open Access Server (JUWEL) at http://www.fz-juelich.de/zb/juwel

Abstract

Benzene, toluene, the xylenes, and the trimethylbenzenes are among the most abundant aromatic trace constituents of the atmosphere mainly originating from anthropogenic sources. The OH-initiated atmospheric photo-oxidation of aromatic hydrocarbons is the predominant removal process resulting in the formation of O_3 and secondary organic aerosol. Therefore, aromatics are important trace constituents regarding air pollution in urban environments. Our understanding of aromatic photo-oxidation processes is far from being complete. This work presents novel approaches for the investigation of OH-initiated atmospheric degradation mechanisms of aromatic hydrocarbons.

Firstly, pulsed kinetic studies were performed to investigate the prompt HO_2 formation from OH + aromatic hydrocarbon reactions under ambient conditions. For these studies, the existing OH reactivity instrument, based on the flash photolysis/laser-induced fluorescence (FP/LIF) technique, was extended to the detection of HO_2 radicals. The experimental design allows for the determination of HO_2 formation yields and kinetics. Results of the pulsed kinetic experiments complement previous product studies and help to reduce uncertainties regarding the primary oxidation steps.

Secondly, experiments with aromatic hydrocarbons were performed under atmospheric conditions in the outdoor atmosphere simulation chamber SAPHIR (Simulation of Atmospheric PHotochemistry In a large Reaction chamber) located at Forschungszentrum Jülich. The experiments were aimed at the evaluation of up-to-date aromatic degradation schemes of the Master Chemical Mechanism (MCMv3.2). The unique combination of analytical instruments operated at SAPHIR allows for a detailed investigation of HO_x and NO_x budgets and for the determination of primary phenolic oxidation product yields.

MCMv3.2 deficiencies were identified and most likely originate from shortcomings in the mechanistic representation of ring fragmentation channels. These shortcomings relate to the formation of peroxy radicals, the NO to NO_2 conversion, and the O_3 production. Conceptual ideas were presented to overcome these MCMv3.2 shortcomings and an improved reaction mechanism was constructed. However, major deficiencies still remain that require further investigations. Regarding the primary oxidation steps, the results of this work confirm the current MCMv3.2 recommendations. Proposed primary oxidation products are, e.g., phenols and epoxides. Phenol yields are in line with the MCMv3.2 values. The results of the complementary pulsed kinetic studies are consistent with the proposed combined formation yields of phenols plus epoxides. So far, epoxides have only been identified tentatively and the results of this work provide more quantitative information.

Kurzfassung

Benzol, Toluol, die Di- und Trimethylbenzole gehören zu den häufigsten Vertretern aromatischer Kohlenwasserstoffe in der Atmosphäre und werden vorwiegend von anthropogenen Quellen freigesetzt. Die OH-initiierte Photo-Oxidation ist der vorherrschende Abbauprozess, der zur Bildung von O_3 und sekundärem organischen Aerosol führt. Daher beeinflussen Aromaten vor allem die Luftqualität in urbanen Räumen. Die Photo-Oxidationsprozesse von Aromaten sind nicht vollständig aufgeklärt und diese Arbeit stellt neue experimentelle Ansätze zur Untersuchung der Reaktionsmechanismen vor.

Zunächst wurde in gepulsten kinetischen Experimenten die prompte HO_2-Bildung aus den Reaktionen von OH mit Aromaten untersucht. Die Studien wurden unter atmosphärischen Bedingungen mit dem OH-Reaktivitäts-Instrument durchgeführt. Die Methode basiert auf der Blitzlichtphotolyse gekoppelt mit der Laser-induzierten Fluoreszenz zum Nachweis von OH. In dieser Arbeit wurde das vorhandene Instrument auf den Nachweis von HO_2-Radikalen erweitert. Die Experimente ermöglichen die Bestimmung der Reaktionskinetik und Ausbeute der HO_2-Bildung. Diese Untersuchungen stellen einen komplementären Ansatz zu früheren Produktstudien dar und reduzieren die Unsicherheiten bezüglich primärer Oxidationsschritte.

Weiterhin wurden Experimente mit Aromaten in der Atmosphärensimulationskammer SAPHIR (Simulation of Atmospheric PHotochemistry In a large Reaction chamber) am Forschungszentrum Jülich durchgeführt. Diese Experimente dienen der Bewertung aktueller photochemischer Modelle des „Master Chemical Mechanism“(MCMv3.2). SAPHIR ist mit einer einzigartigen Kombination analytischer Instrumente ausgestattet, die eine detaillierte Auswertung von HO_x- und NO_x-Budgets sowie die Bestimmung primärer Ausbeuten an Phenolen ermöglicht.

Es wurde gezeigt, dass der MCMv3.2 gravierende Mängel aufweist, die auf Unsicherheiten in der mechanistischen Repräsentation der Ringfragmentierung zurückzuführen sind. Diese Unzulänglichkeiten betreffen vor allem die Bildung von Peroxyradikalen, die Konversion von NO zu NO_2 sowie die O_3-Produktion. Konzeptionelle Ideen zur Beseitigung dieser Mängel sowie ein verbesserter Mechanismus wurden vorgestellt. Eine perfekte Übereinstimmung von Modell und Messungen konnte allerdings nicht erzielt werden und weitere Untersuchungen sind erforderlich. Bezüglich der primären Ausbeuten von Phenolen und Epoxiden bestätigen die Ergebnisse dieser Arbeit die Empfehlungen des MCMv3.2. Ermittelte Phenolausbeuten befinden sich in guter Übereinstimmung mit den MCMv3.2-Werten und die komplementären Ergebnisse der gepulsten kinetischen Experimente bestätigen weiterhin die kombinierten Ausbeuten von Phenolen und Epoxiden.

Contents

1

Introduction

Various organic chemicals are released to the earth's atmosphere from both biogenic and anthropogenic sources. The estimated global emission rate of volatile organic compounds (VOCs) is on the order of 10^{12} g per year.[1,2] Emissions from the terrestrial vegetation, especially tropical forests, are the major source of biogenic VOCs. The predominant anthropogenic VOC sources are incomplete combustion processes in stationary and mobile engines, evaporation of solvents from industrial production plants, and residential wood burning.[3] The enormous emission rate of VOCs is balanced by an equally large destruction rate. Once emitted to the atmosphere, the VOCs are oxidized by hydroxyl (OH) and nitrate (NO_3) radical-initiated reactions, by ozonolysis, and by photolysis. For most of the VOCs, the OH-initiated tropospheric oxidation, involving a complex reaction sequence, is the main degradation process.[4,5] The oxidation of VOCs in the presence of nitrogen oxides NO_x (sum of NO and NO_2) results in the formation of oxygenated volatile organic compounds (OVOCs), oxidants like O_3 and inorganic acids, and short-lived radical species like hydroperoxy (HO_2) and organic peroxy (RO_2) radicals.[6] Compared to their organic precursor molecules, OVOCs have a reduced vapour pressure and an elevated water-solubility. Therefore they can be deposited at surfaces, washed out by precipitation, or can condense to form secondary organic aerosol (SOA).[7] However, they also exhibit considerable reactivity towards OH radicals. Many VOCs and OVOCs detected in ambient air are toxic or carcinogenic and might cause respiratory and cardiovascular diseases. Furthermore, airborne particulate matter has adverse health effects at exposures found in urban areas in both developed and developing countries.[8,9] On a global scale, CO_2, the fully oxidized end product of VOC degradation, impacts the earth's radiative balance by absorbing radiation in the infrared region. Aerosol particles also influence the radiation budget directly by scattering incoming solar radiation and indi-

rectly by altering cloud processes. Nowadays, air pollution and its relation to human health and climate change is a worldwide issue and plays a central role in atmospheric research.[10]

In the urban environment the organic emissions are dominated by the exploitation of fossil fuels (gas, oil, and coal). Petroleum products like gasoline and diesel fuel contain alkenes, alkanes, and up to 50% (by weight) of monocyclic and polycyclic aromatic hydrocarbons.[11] This large fraction of aromatics in motor fuels is also reflected by their abundance in urban air.[12,13] Up to 40 % of the OH consumption can be assigned to reactions with aromatic hydrocarbons.[14] Thus, aromatics, such as benzene[15], alkylbenzenes[16], and hydroxybenzenes[17,18] are strongly affecting atmospheric chemistry in cities, industrialized areas, and districts of dense traffic. However, because of their atmospheric lifetimes of up to several days[19], some aromatics can undergo long-range transport and also affect air quality on a regional scale.[20]

To assess the impact of air pollution by aromatics, a detailed understanding of their atmospheric fate is needed. In the last three decades a large number of studies on the OH-initiated oxidation of aromatics was published. The previous research focussed on reaction kinetics and product distributions and a comprehensive set of reaction rate constants and product yields is known. However, despite enormous efforts in recent years our knowledge is not complete. A large fraction of degradation products is identified but in many cases the measured formation yields are subject to substantial uncertainties.[14] At the beginning of the 1990s the available experimental information was used to build up an explicit representation of the degradation mechanisms of more than 100 VOCs including 18 aromatics. This explicit mechanistic representation, called Master Chemical Mechanism (MCM), aimed at the improved prediction of O_3 and OVOC formation.[21–23] Since 1997 MCM was continuously revised, partly based on validation against environmental chamber experiments with aromatics performed in the European Photoreactor (EUPHORE) located in Valencia, Spain.[24–28] For the current MCM (version 3.2) there are still outstanding issues that hinder its ability to describe the atmospheric fate of aromatic hydrocarbons correctly. The major MCM shortcomings found in chamber experiments are the overprediction of peak O_3 concentration and the underprediction of the OH radical production.[29]

The general aim of this work is to obtain a better understanding of the OH-initiated atmospheric oxidation of aromatic hydrocarbons. The employed approach is twofold:
(i) Pulsed kinetic laboratory studies based on the flash photolysis/laser-induced fluorescence (FP/LIF) technique are performed. This part of the work investigates the secondary formation of hydroperoxy (HO_2) radicals from the primary products of the OH + aromatic reaction with no preced-

ing NO reactions (so called prompt HO_2). HO_2 radicals play an important role in atmospheric chemistry since their ability to recycle OH in reactions with NO is connected with O_3 formation. Chapter 2 highlights the relevance of HO_2 in general and with special regard to the atmospheric chemistry of aromatics. The LIF-based OH reactivity instrument, previously developed for the measurement of total OH radical loss rate constants in ambient air, is used for the pulsed kinetic experiments. In this work the instrument is extended to the HO_x (sum of OH and HO_2) measurement mode. Chapter 3 depicts technical details of the instrument and the experimental setup. The modified instrument facilitates the alternating measurement of OH and HO_x decay curves after pulsed formation of OH in the presence of selected reactants. An experimental procedure is developed to extract HO_2 formation kinetics and formation yields from the OH and HO_x profiles by applying analytical solutions and curve fitting routines. This approach is complementary to previous product studies and can help to reduce budget uncertainties concerning the initial reaction steps of the OH-initiated oxidation of aromatic hydrocarbons. The results of the pulsed kinetic experiments are presented in chapter 4 and discussed in the context of available complementary literature data.
(ii) The second approach of this work is the investigation of aromatic compound degradation in the outdoor atmosphere simulation chamber SAPHIR (Simulation of Atmospheric PHotochemistry In a large Reaction chamber) located at the Forschungszentrum Jülich (FZJ), Germany. A large suite of analytical instruments is employed. The main objectives are the detection of stable organic oxidation products and short-lived radical intermediates. Determination of primary oxidation product yields is attempted rather than a quantification of all degradation products. Many primary oxidation products are formed via unique reaction channels. Thus, their formation yields give information about the extent of different degradation pathways. The SAPHIR instrumentation was recently extended to measure the total OH reactivity by means of the LIF-based instrument. This quantity, together with simultaneous measurement of OH, HO_2, and RO_2 radical concentrations, is a constraint for the conversion of OH to peroxy radicals. The idea behind is to calculate the total OH production and destruction rates from measured quantities and check whether the budget is balanced. Simulation chamber experiments are also evaluated by model-measurement comparison using a MCM-based numerical model and results are presented in chapter 5.

A brief summary of the outcome of this work is given in chapter 6. Moreover, the most important results are discussed with regard to their relevance for atmospheric chemistry.

2

Current state of knowledge

The atmospheric oxidative VOC degradation is driven by natural sunlight and proceeds via catalytic radical cycles. The general concept of tropospheric radical photochemistry is briefly presented in section 2.1. Section 2.2 gives more detailed information about the currently proposed OH-initiated photooxidation mechanisms of monocyclic aromatics.

2.1 Tropospheric photochemistry

The self-cleaning ability of our atmosphere mainly arises from OH radical-initiated oxidation processes of VOCs. In the troposphere, the most important primary OH source is the photolysis of ozone (O_3) at wavelengths below about 330 nm yielding electronically excited oxygen atoms, $O(^1D)$, that subsequently react with ubiquitous water vapour (H_2O) to give hydroxyl radicals.

$$O_3 + h\nu \longrightarrow O(^1D) + O_2 \qquad (\lambda < 330 \text{ nm}) \tag{R1}$$

$$O(^1D) + H_2O \longrightarrow 2\,OH \tag{R2}$$

Only about 10% of $O(^1D)$ formed via R1 react with H_2O to yield OH. The bulk of $O(^1D)$ is deactivated by collisional quenching with other molecules (M), mostly nitrogen (N_2) and oxygen (O_2), giving ground state $O(^3P)$.

$$O(^1D) + M \longrightarrow O(^3P) + M \tag{R3}$$

$O(^3P)$ recombines with O_2 to regenerate O_3:

$$O(^3P) + O_2 + M \longrightarrow O_3 + M \tag{R4}$$

OH does not react with the major constituents of air, N_2 and O_2, but it reacts with trace constituents like VOCs. During the daytime, the OH + VOC reaction is the most effective sink for ambient organic trace gases. The OH-initiated oxidation of VOCs proceeds via radical chain reactions where OH is not consumed, but regenerated in catalytic cycles. In the presence of O_2 and depending on the respective compound, the OH + VOC reaction yields hydroperoxy (HO_2) and/or organic peroxy (RO_2) radicals, collectively termed peroxy radicals.

$$OH + VOC + O_2 \longrightarrow HO_2 + \text{products} \tag{R5}$$

$$OH + VOC + O_2 \longrightarrow RO_2 \tag{R6}$$

R5 and R6 are not elementary reactions. The initial OH attack is followed by an O_2 reaction but the OH attack is rate determining. Here, R5 and R6 are treated as overall reactions. More details on the elementary reaction steps are given in section 2.2 for the atmospheric chemistry of aromatics. Peroxy radicals undergo radical-propagating reactions with nitrogen monoxide (NO) to form either OH or organic alkoxy radicals (RO).

$$HO_2 + NO \longrightarrow OH + NO_2 \tag{R7}$$

$$RO_2 + NO \longrightarrow RO + NO_2 \tag{R8}$$

The atmospheric fate of organic alkoxy radicals comprises a complex reaction sequence that is specific for each RO. Some RO undergo rapid decomposition to fragments. These fragments again react with O_2 yielding HO_2. Other RO directly react with O_2 to give HO_2.

$$RO \longrightarrow \text{fragments} \tag{R9}$$

$$RO/\text{fragments} + O_2 \longrightarrow HO_2 + \text{products} \tag{R10}$$

Details for RO stemming from aromatic compound degradation are addressed in the following section.

Finally, peroxy radicals undergo radical-terminating reactions yielding water, hydrogen peroxide (H_2O_2), organic hydroperoxides (ROOH), organic peroxides (ROOR), organic nitrates (RNO_3), and nitrous (HNO_2) as well as nitric acid (HNO_3).

$$OH + HO_2 \longrightarrow H_2O + O_2 \tag{R11}$$

$$HO_2 + HO_2 \longrightarrow H_2O_2 + O_2 \tag{R12}$$

$$HO_2 + RO_2 \longrightarrow ROOH + O_2 \tag{R13}$$

$$RO_2 + RO_2 \longrightarrow ROOR + O_2 \tag{R14}$$

$$RO_2 + NO \longrightarrow RNO_3 \tag{R15}$$

$$OH + NO + M \longrightarrow HNO_2 + M \tag{R16}$$

$$OH + NO_2 + M \longrightarrow HNO_3 + M \tag{R17}$$

These radical-terminating reactions act as a net sink of HO_x. Among them, the formation of HNO_3 via reaction R17 is the dominant sink in polluted regions.[30] This reaction is also a net loss of NO_x in contrast to R16 because HNO_2 can be photolysed to OH + NO.

Beside the recycling of radicals, reactions R7 and R8 are also forming NO_2. At wavelengths around 300−420 nm, NO_2 is photolysed to give NO and $O(^3P)$:

$$NO_2 + h\nu \longrightarrow NO + O(^3P) \qquad (\lambda = 300 - 420 \text{ nm}) \tag{R18}$$

$O(^3P)$ reacts with O_2 yielding O_3 via reaction R4. The formal transfer of an oxygen atom from peroxy radicals to O_2 mediated by NO (involving reactions R7, R8, R18, and R4) is the tropospheric O_3 production process. O_3, in turn, is photolysed to form OH via reactions R1 and R2.

2.2 OH-initiated oxidation of monocyclic aromatics

A large body of experimental studies on the OH-initiated atmospheric oxidation of aromatic hydrocarbons is available and fig. 2.1 shows the current understanding of the initial reaction steps using the example of 1,3,5-trimethylbenzene (1,3,5-TMB). The bulk of the OH + aromatic hydrocarbon reaction ($\geq 90\%$)[31] proceeds via reversible OH-addition to the ring yielding an aromatic-OH-adduct (in the following referred to as AOH, fig. 2.1, A). Minor reaction channels are the dealkylation[32] (fig. 2.1, I) and the H-atom abstraction from substituent alkyl groups finally yielding benzaldehydes (J, after NO reaction step).[33,34] Under atmospheric conditions the fate of AOH is dominated by reactions with O_2. The AOH + O_2 reactions have been widely studied and were found to proceed via reversible pathways forming a peroxy radical (B) and irreversible pathways.[35–42] Experimentally confirmed products of the AOH + O_2 reactions are phenols (C)[25,32,43–47], epoxides (E)[33,47–49], and a bicyclic peroxy radical (G).[33,49] This peroxy radical is formed after rearrangement and addition of another O_2 and is referred to as biRO_2. Formation of oxepins (H) was postulated[50,51] but was experimentally shown to be inoperative for OH + benzene.[52] Phenols, epoxides, and oxepins are assumed to be co-products of prompt HO_2 (i.e. no preceding NO reaction step required) whereas the formation of biRO_2 is not associated with prompt HO_2. For most of the aromatic compounds, the only quantified HO_2 co-products are phenols. An upper limit for the combined yields of epoxides and oxepins can be obtained by comparing measured prompt HO_2 yields to phenol yields reported in the literature.

The bicyclic peroxy radical biRO_2 is considered to be a major product of the OH + aromatic reaction with formation yields of $> 50\%$ for alkylbenzenes.[27,28] Fig. 2.2 shows possible reaction pathways for the atmospheric fate of biRO_2. Radical-radical reactions are usually of minor importance in urban environments, but their impact on tropospheric photochemistry under low NO_x conditions is of growing interest. On the one hand, radical-radical reactions are assumed to proceed via terminating channels yielding bicyclic hydroperoxides (fig. 2.2, VI), bicyclic diols (VII), and bicyclic ketones (VIII).[33,49,55,56] These bicyclic species are assumed to exhibit considerable reactivity towards OH. Further, they are considered to be photolysed (as shown in fig. 2.2 for the bicyclic hydroperoxide (VI)). However, no experimental data for these reactions are reported in literature. On the other hand, it was recently speculated that the biRO_2 + HO_2 reaction could also recycle an OH radical plus the bicyclic alkoxy radical (biRO, I).[33,49] A similar

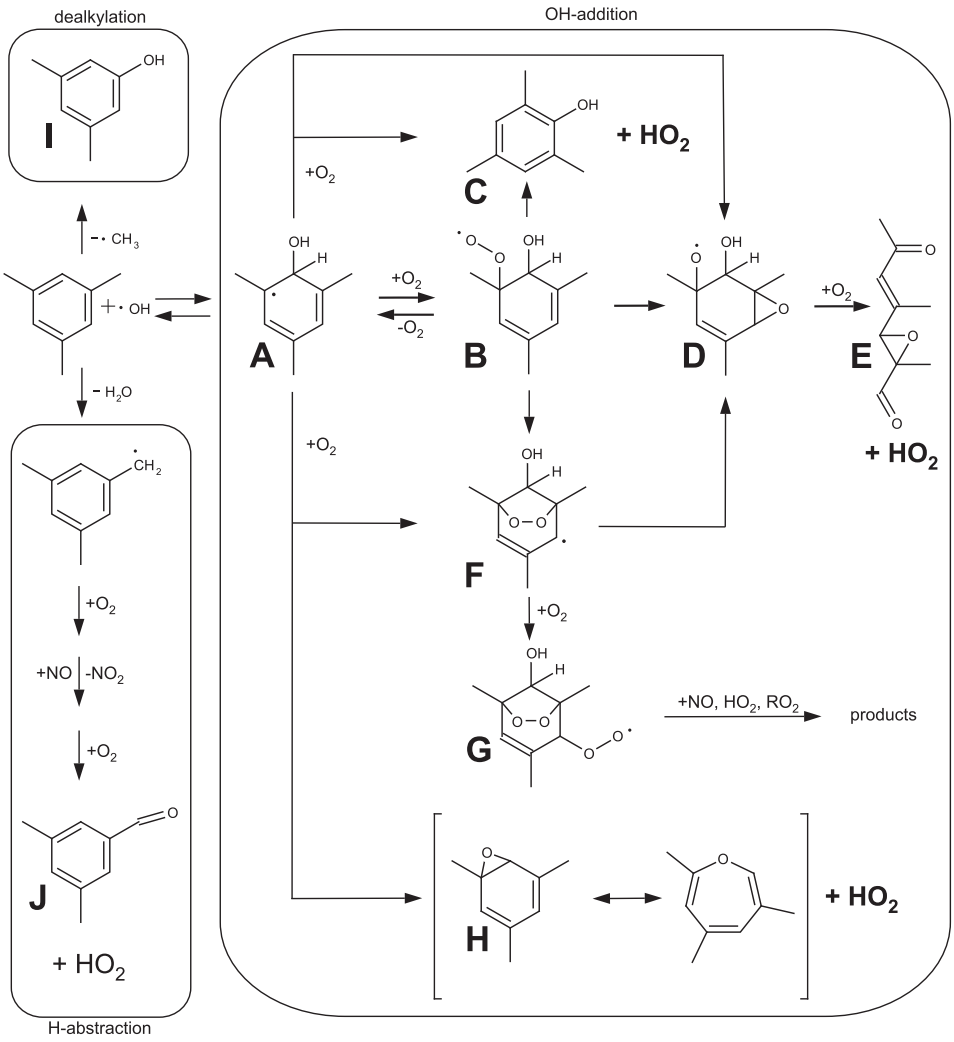

Figure 2.1: Postulated reaction pathways of the OH-initiated oxidation of 1,3,5-TMB.[14,32,53,54] For convenience, different resonance structures and possible isomers are not shown. HO_2 formed without preceding NO reaction steps is indicated in bold face.

recycling of radicals is assumed to be operative for the $biRO_2$ + RO_2 reactions. In reactions with NO, $biRO_2$ conventionally either forms biRO plus NO_2 or a bicyclic nitrate ($biRNO_3$, II). Species with molecular weights corresponding to bicyclic nitrates have been observed in chamber experiments.[56] However, recent research showed that this nitrate forming pathway is of minor importance (<0.1)[57] and the bulk of the $biRO_2$ + NO reaction proceeds via biRO that subsequently reacts with O_2 yielding ring fragmentation products and HO_2. The ring scission forms either α-dicarbonyls (α-DCs, III) plus unsaturated γ-dicarbonyls (γ-DCs, IV) or α-dicarbonyls plus furanones (V). Depending on the structure of the aromatic, several combinations of coproducts are possible. α-DCs[24,44,45,58] (glyoxal, methylglyoxal, and dimethylglyoxal) and γ-DCs[46,59–61] (e.g. butenedial, 4-oxo-2-pentenal, etc.) are the experimentally confirmed primary oxidation products of aromatics resulting from ring fragmentation. In contrast, furanones (V) have only been identified tentatively.[55,56,62,63] Nevertheless, furanones were observed as major products of γ-DC photolysis.[64] An important difference between γ-DCs and furanones is their subsequent atmospheric degradation. Part of the acyclic peroxy radicals from the OH + γ-DC reaction is considered to form peroxyacetylnitrate (PAN) derivatives in reactions with NO_2. Such a storage of reactive NO_x is not considered for the cyclic peroxy radicals stemming from OH + furanone.[27,28]

Finally, it should be noted that bicyclic nitrates, hydroperoxides, and ketones[56,65] as well as ring fragmentation products like α-DCs, γ-DCs, and furanones contribute to the formation and growth of SOA.[66–68]

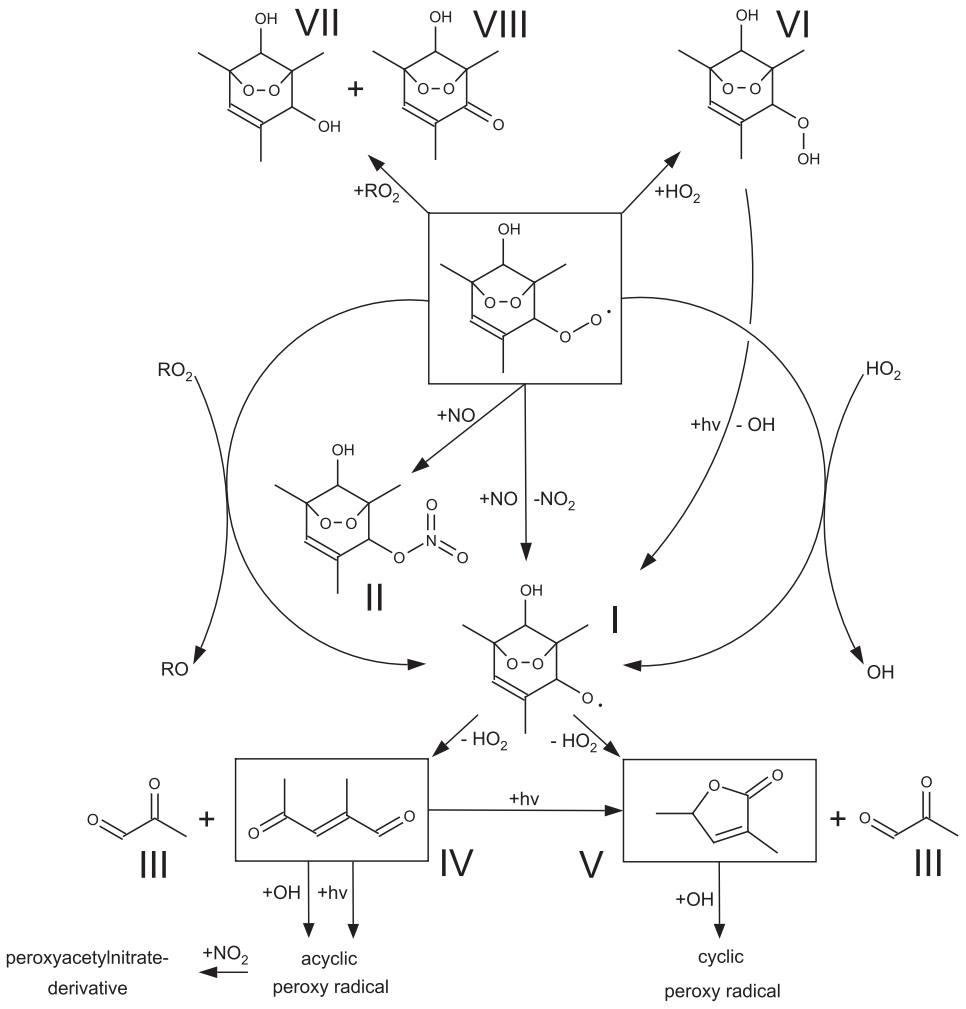

Figure 2.2: Simplified reaction scheme for the atmospheric fate of the bicyclic peroxy radical stemming from the OH-initiated oxidation of 1,3,5-TMB.[49,55,62] For convenience, not all possible peroxy radical reactions are presented.

3

LIF-based OH reactivity instrument

This chapter highlights the concept of OH reactivity measurements. Furthermore, the instrument and technical modifications are presented. Two experimental approaches are adopted to investigate the OH-initiated atmospheric oxidation of aromatic hydrocarbons. Firstly, the LIF-based OH reactivity instrument is extended to the detection of HO_2 radicals for the first time to investigate HO_2 formation upon the OH + aromatic hydrocarbon reactions under ambient conditions in the absence of NO. Secondly, the degradation of aromatics is studied under atmospheric conditions in the outdoor simulation chamber SAPHIR at FZJ. In these experiments the LIF-based OH reactivity instrument is used to measure the total OH loss rate constant within the chamber. The OH loss rate constant is a key constraint for the investigation of the HO_x budget in chamber experiments.

3.1 Measurement principle

Atmospheric OH is very short-lived owing to its reactivity towards a variety of trace constituents. The total OH reactivity k_{OH}, which is equivalent to the inverse atmospheric OH lifetime τ_{OH}^{-1}, is a pseudo-first-order rate constant:

$$k_{OH} = \tau_{OH}^{-1} = \sum k_{X_i+OH}[X_i] \tag{3.1}$$

$[X_i]$ denotes the concentration of a reactive trace constituent and k_{X_i+OH} is the respective second-order rate constant. The fundamental principle of LIF-based OH reactivity measurements is the time-resolved recording of OH decay curves[69–71] where an initial OH concentration, $[OH]_0$, is produced artificially.

Under these conditions, the following differential equation applies:

$$-\frac{\mathrm{d[OH]}}{\mathrm{d}t} = \sum k_{\mathrm{X_i+OH}}[\mathrm{X_i}][\mathrm{OH}] \tag{3.2}$$

Assuming a large excess of reactants $\mathrm{X_i}$, integration of this equation leads to an exponential expression for the decay of OH:

$$[\mathrm{OH}] = [\mathrm{OH}]_0 \times \exp(-\sum k_{\mathrm{X_i+OH}}[\mathrm{X_i}]t) \tag{3.3}$$

k_{OH} is obtained by fitting eq. 3.3 to measured OH decay curves.

The instrument used in this work was originally developed to measure k_{OH} in ambient air.[72,73] It employs the flash photolysis/laser-induced fluorescence (FP/LIF) technique that was first realized by Calpini et al.[69] and later by Sadanaga et al.[71]. A schematic of the OH reactivity instrument is shown in fig. 3.1 and technical details are listed in table 3.1. Basically, it consists of a tube-shaped reaction volume operated at atmospheric pressure and a temperature of 298 K. Synthetic air containing traces of O_3 and H_2O as OH precursors is sampled through the gas inlet into the reaction volume. A frequency-quadrupled Nd:YAG laser is used for the pulsed production of OH at 266 nm (R1, R2). If the sampled air contains reactive trace gases (e.g. VOCs), OH is consumed yielding peroxy radicals (HO_2 and/or RO_2) or other products. The detection of OH radicals is performed downstream of the tube inlet by the laser-induced fluorescence technique after gas-expansion. Air is sampled from the center of the reaction volume through a sub-mm nozzle into a low pressure detection cell. OH fluorescence is induced at 308 nm and focused onto a gated photomultiplier. By adding a small flow of pure NO into the expanding gas upstream of the detection zone, HO_2 formed in the reaction volume can be partly converted to OH (R7) and detected as additional fluorescence signal (HO_x measurement mode). Switching between the OH and HO_x measurement modes is possible within a few minutes.

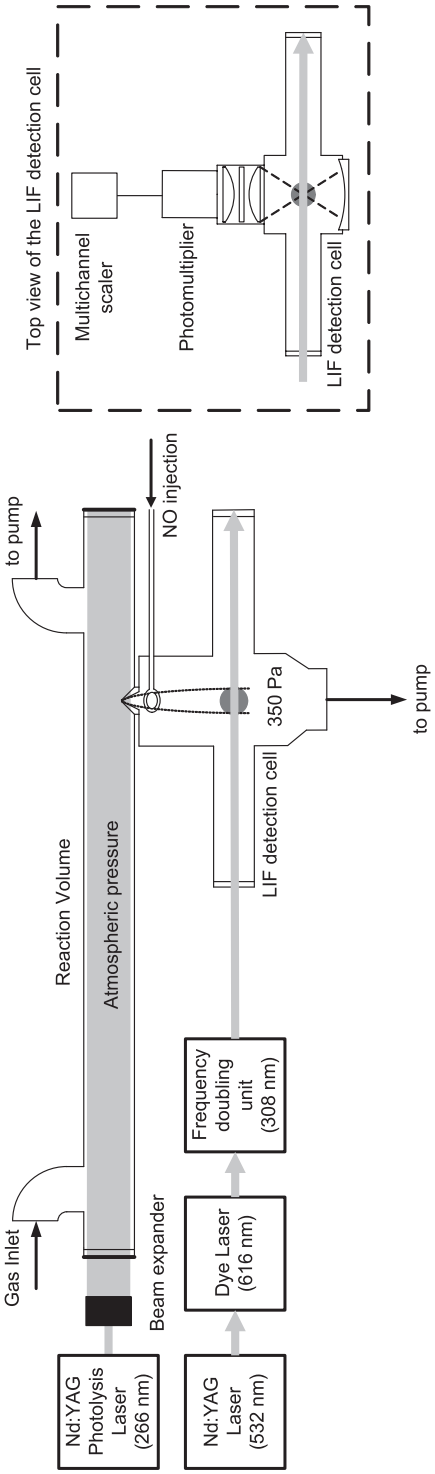

Figure 3.1: Scheme of the LIF-based OH reactivity instrument. The shaded area indicates the volume illuminated by the pulsed 266 nm photolysis laser. Time-resolved OH detection is made in a gas expansion in the attached low pressure LIF detection cell.

Table 3.1: Technical details of the LIF-based OH reactivity instrument.

Operating Parameter	Specification
Reaction volume	
Length	800 mm
Diameter	40 mm
Material	Black anodized aluminum
Temperature	298 K
Pressure	1000 mbar
Sampling flow rate[a]	20 L min^{-1}
Mean residence time	1.5 s
Detection cell	
Edge length	100 mm
Material	Black anodized aluminum
Pressure	3.5 mbar
Sampling nozzle	Conical nozzle (Beam Dynamics)
Sampling nozzle material	Nickel
Sampling nozzle diameter (pulsed kinetic studies)	0.2 mm
Sampling nozzle diameter (simulation chamber studies)	0.7 mm
Sampling flow rate[a]	0.25 L min^{-1} [c] / 3 L min^{-1} [d]
Sampling nozzle position[b]	500 mm
Mean residence time	240 μs
NO addition nozzle	Ring made of glass tubing (home-made); 6 orifices positioned downstream; orifice diameter $\approx$ 0.5 mm
Ring nozzle inner diameter	10 mm
Distance sampling nozzle − detection	100 mm
Distance ring nozzle − detection	60 mm

[a] At 298 K and 1013 mbar.
[b] Distance between gas inlet of the reaction volume and center of the sampling nozzle.
[c] For the 0.2-mm-nozzle.
[d] For the 0.7-mm-nozzle.

3.2 Reaction volume

The tube-shaped reaction volume made of black anodized aluminum is sealed by a quartz window (Heraeus, Suprasil anti-reflection coated) at each end to facilitate the transmission of the 266 nm laser flash. Gas inlet and outlet are installed perpendicular to the longitudinal axis of the reaction volume. A laminar flow of synthetic air is maintained using a membrane pump (Vacuubrand, MD-4C) and a calibrated mass flow controller (Bronkhorst, Low Δp). The O_3 mixing ratio is monitored at the gas inlet by a commercial photometer (Ansyco, O3 41M). Pressure (MKS, pressure transducer Baratron 622A), relative humidity as well as temperature (Vaisala, HMP 133) are continuously monitored at the gas outlet.

3.3 Detection cell

The detection of OH is performed in a low pressure cubical-shaped cell made of black anodized aluminum that is attached to the reaction volume 500 mm downstream of the gas inlet. The pressure in the detection cell is maintained at 3.5 mbar by a vacuum pump (BOC Edwards, IPX 500A) and continuously monitored by a pressure transducer (Setra 205-2). Air from the reaction volume is sampled in a supersonic expansion through a conically-shaped inlet nozzle (Beam Dynamics) with an opening angle of 70° and an orifice diameter of 0.2 mm (pulsed kinetic studies) or 0.7 mm (simulation chamber studies). The top of the nozzle is mounted a few millimeters below the center of the reaction volume. In addition to the sample flow from the reaction volume, 0.6 L min^{-1} of pure N_2 are introduced 30 mm downstream of the nozzle orifice as a sheath flow between the gas beam of the supersonic expansion and the wall. The sampled gas beam is directed vertically through the detection cell. Perpendicular to the sampled gas beam, the 308 nm probe laser beam is passed through the cell using baffle arms containing three baffles each and quartz windows (LINOS Photonics, anti-reflection coated). To avoid build up of trace gases, the baffle arms are continuously flushed with pure N_2 (0.2 L min^{-1} for each arm). At right angles to both, the sampled gas beam and the probe laser beam, the OH fluorescence emitted from the detection zone is focused onto a gated photomultiplier (Perkin Elmer, C 1943 P). Four quartz lenses (Thorlabs, anti-reflection coated, focal length = 150 mm) and an interference filter (Omega Optical) are placed in front of the photomultiplier to selectively collect the fluorescence signal. To enhance the collection efficiency, a concave mirror is mounted opposite to the photomultiplier. In order to convert HO_2 to OH in the detection cell via reaction R7, the NO

injection is implemented in the OH reactivity instrument for the first time. This technique was originally developed to measure atmospheric HO_2 concentrations.[74,75] Here it is applied to alternately measure OH and HO_x decay curves. In the HO_x measurement mode, a 10% mixture of NO (Linde, 99.5%) in N_2 is injected through a ring made of 6 mm glass tubing with small holes surrounding the expanding gas beam. The distance between NO addition and OH detection is about 60 mm. Prior to the injection, the NO passes a cartridge filled with sodium hydroxide coated silicate (Sigma-Aldrich, Ascerite) to remove impurities.

3.4 Photolysis laser system

A fourth harmonic Nd:YAG laser (Big Sky, CFR 200, 266 nm, pulse energy ≈15 mJ, pulse duration ≈10 ns) is passed longitudinally through the reaction volume. The Q-switched laser is pumped by a flashlamp operated at a repetition rate of 15 Hz. Typically, the laser is fired every 1.5−2.5 s to assure that the content of the reaction volume is exchanged completely between two laser shots. OH radicals are produced by pulsed photolysis of O_3 at 266 nm in the presence of H_2O. Typical O_3 and H_2O concentrations are 2×10^{12} cm^{-3} and 3×10^{17} cm^{-3}, respectively, resulting in OH starting concentrations of $\leq 8\times10^{9}$ cm^{-3} formed virtually instantaneously after the 266 nm laser flash. The photolysis laser beam is directed through the reaction volume using dielectric mirrors (LINOS Photonics, high-reflection coated). Its diameter of 6 mm is expanded to about 30 mm using an alignment of a biconcave quartz lens (LINOS Photonics, anti-reflection coated, focal length = −30 mm) and a plano-convex quartz lens (LINOS Photonics, anti-reflection coated, focal length = 150 mm). The expanded laser beam unavoidably hits the sampling nozzle of the detection cell since its orifice is mounted in the center of the reaction volume.

3.5 Probe laser system

In this work OH radicals are detected by excitation from the ground state ($X^2\Pi$, $\nu''=0$) to the state $A^2\Sigma^+$, $\nu'=0$, using the transition of the $Q_{11}(3)$ absorption line at 308.155 nm and subsequent relaxation via emission of a fluorescence photon within the same vibronic transition. A high repetition rate (8.5 kHz), diode pumped, frequency-doubled Nd:YAG laser (Spectra Physics, Navigator I) provides 532 nm radiation. The second harmonic of the Nd:YAG laser pumps a tunable dye laser. An ethanolic (Merck, 99.9%) solution of

80 mg L^{-1} Rhodamine 101 (Radiant Dyes) is used as active laser medium yielding an output at around 616 nm. Wavelength selection is done by angle tuning of a solid-state etalon inside the laser resonator. The 616 nm radiation is frequency-doubled to 308 nm using a β-bariumborate crystal. The UV probe laser beam is split by beam pick-off optics (New Focus). Part of the 308 nm radiation is coupled into the detection cell via an optical fibre (OZ Optics, QMMJ-5,5HPM-UVVIS-200/240). An UV photodiode (Gigahertz-Optik, SSO-BL100-2BNC) shielded by an optical filter (Schott, DUG-11) is mounted behind the exit quartz window of the detection cell to continuously monitor the 308 nm laser power. Another fraction of the 308 nm radiation is coupled into a reference cell operated at 60 mbar. This reference cell is continuously flushed with humidified argon (Linde, 99.9999%). Photolysis of H_2O at 185 nm ($H_2O + h\nu \longrightarrow OH + H$) using a low-pressure discharge mercury lamp produces high OH concentrations. By periodically tuning the probe laser on- (308.155 nm) and off-resonant ($\pm$0.005 nm) it is possible to distinguish between OH fluorescence and background signal. In case of a wavelength drift, possibly caused by thermal effects, the etalon position is automatically realigned. In this way, the wavelength scans assure that the probe laser system is always operated at the desired OH absorption line.

3.6 Air sampling and addition of trace gases

Highly purified synthetic air made from liquid samples of N_2 and O_2 (Linde, >99.9999%) is provided by a gas mixing system. The air is humidified using a temperature-controlled ($\approx$20°C) saturator filled with pure H_2O (Milli-Q). O_3 is produced in an ozonizer and then added to the main flow of synthetic air. The ozonizer is based on O_2 photolysis at 185 nm. Air is either sampled directly from the gas mixing system (for pulsed kinetic experiments) or from the atmosphere simulation chamber (SAPHIR experiments). During SAPHIR experiments the OH reactivity instrument (housed in an air-conditioned container below the chamber) is sampling through a teflon inlet line of approximately 7 m length. Temperature and pressure differences between SAPHIR chamber and reaction volume of the instrument are considered in the data analysis. An additional flow of synthetic air from the gas mixing system containing O_3 and/or H_2O is added to the air sampled from the SAPHIR chamber if O_3 mixing ratio and relative humidity drop below thresholds of 50 ppb and 60%, respectively, to assure a sufficient OH starting concentration after the photolysis laser flash. The resulting dilution of the gas flow sampled from the SAPHIR chamber is also taken into account in the data analysis.

Table 3.2: Hydrocarbons used in this work.

Hydrocarbon	Distributor	Purity / %
Benzene	Merck	99.8
Toluene	Merck	99.9
Ethylbenzene	Fluka	99.0
o-Xylene	Fluka	99.5
m-Xylene	Fluka	99.5
p-Xylene	BDH Prolabo	99.8
1,2,3-Trimethylbenzene	LGC	91.7
1,2,4-Trimethylbenzene	LGC	99.7
1,3,5-Trimethylbenzene	Sigma Aldrich	99.0
Hexamethylbenzene	Alfa Aesar	99.0
Phenol	Merck	99.0
o-Cresol	Sigma Aldrich	99.0
2,5-Dimethylphenol	Merck	99.0
2,4,6-Trimethylphenol	Acros Organics	98.0
Cyclohexane	Merck	99.5
Isoprene*	Aldrich	99.0

* Stabilized by 100 ppm of 4-*tert*-butylbenzene-1,2-diol.

For the investigation of OH + VOC reactions by pulsed kinetic experiments, several substances are injected to the main flow of synthetic air. Organic compounds are used as purchased and stated purities are listed in table 3.2. Microliter amounts of benzene, toluene, ethylbenzene, the xylenes, the trimethylbenzenes (TMB), *o*-cresol, cyclohexane, and isoprene are injected into silcosteel containers and pressurized to 3.3 bar with N_2. The gas mixture from the silcosteel container is then introduced with a calibrated mass flow controller (Brooks, 5850 TR) to the main gas flow. Milligramme amounts of hexamethylbenzene (HMB), phenol, 2,5-dimethylphenol, and 2,4,6-trimethylphenol are stored in temperature-controlled flasks that are continuously flushed by a small flow of pure N_2. The N_2 flux is regulated by a calibrated mass flow controller (Brooks, 5850 TR) and finally introduced to the main gas flow. The concentration of the respective organic compound is estimated from the measured OH reactivity. A 1% mixture of carbon monoxide (CO) in N_2 is used for experiments, when CO is added (Messer Griesheim, 99.997%).

3.7 OH and HO_x decay curves

OH excitation laser light (308 nm) and OH fluorescence (307−311 nm) cannot be resolved spectrally. Consequently, the LIF spectroscopy for OH resorts to a pulsed probe laser excitation to facilitate temporal discrimination between laser and fluorescence photons. This experimental technique requires a rigorous timing. Photolysis laser and probe laser are synchronized based on the probe laser trigger. The photolysis laser is operated at a low repetition rate of <1 Hz. However, the photolysis laser shot is inhibited by means of a voltage signal if the probe laser is at an off-resonant wavelength position. Once the photolysis laser is fired (see fig. 3.2 panel (a)), OH radicals are formed in the reaction volume provided that O_3 and H_2O are present. Thereafter OH can be consumed by reactive trace gases (see fig. 3.2 panel (b)). Air containing radicals is sampled into the detection cell and continuously probed by the 308 nm laser at a high repetition rate of 8.5 kHz (c). Gated photon counting using a photomultiplier is deployed to detect fluorescence photons after each probe laser pulse (d). When the laser pulse crosses the detection cell, the gain of the photomultiplier is gated (Photek, Fast High-Voltage Switch GM150-20) to avoid damage by laser stray light. After a delay of about 80 ns with respect to the probe laser pulse (pulse duration ≈20 ns), fluorescence photons are counted for 500 ns by a photon counter card (Becker&Hickl, PMS-400A) (e). Fluorescence is detected over a 1 s time interval and sequentially recorded at a resolution of 1 ms. Typically, 60 decay curves are accumulated to improve the signal-to-noise ratio. HO_x decay curves are recorded accordingly. The only difference is the additional flow of NO injected into the detection cell upstream of the detection zone. After operation in the HO_x mode, the NO injection nozzle is flushed with dry N_2 to remove remaining NO from the tubings.

A typical OH decay curve obtained in clean synthetic air with premixed O_3 and H_2O is shown in fig. 3.3. Although no OH reactant beside O_3 is added, a typical background OH reactivity of $k^0_{OH} = 1.5\ s^{-1}$ is observed. The contribution of the OH + O_3 reaction to k^0_{OH} is minor ($\approx 0.1\ s^{-1}$). Radical-radical reactions are of negligible importance because of the low radical concentrations. The background reactivity is probably dominated by non-chemical loss processes, i.e. by diffusion and wall losses. OH radicals may escape detection by radial diffusion because only part of the reaction volume (a column of 30 mm in diameter) is exposed to the photolysis laser flash. A fringe of 5 mm depth is not illuminated and a radial OH gradient exists. However, given an OH diffusion coefficient of 0.22 cm^2s^{-1} [76], radial diffusion is considered to account only for a fraction of the non-chemical OH loss. In the HO_x mode of the instrument a similar background loss for HO_2 radicals is observed

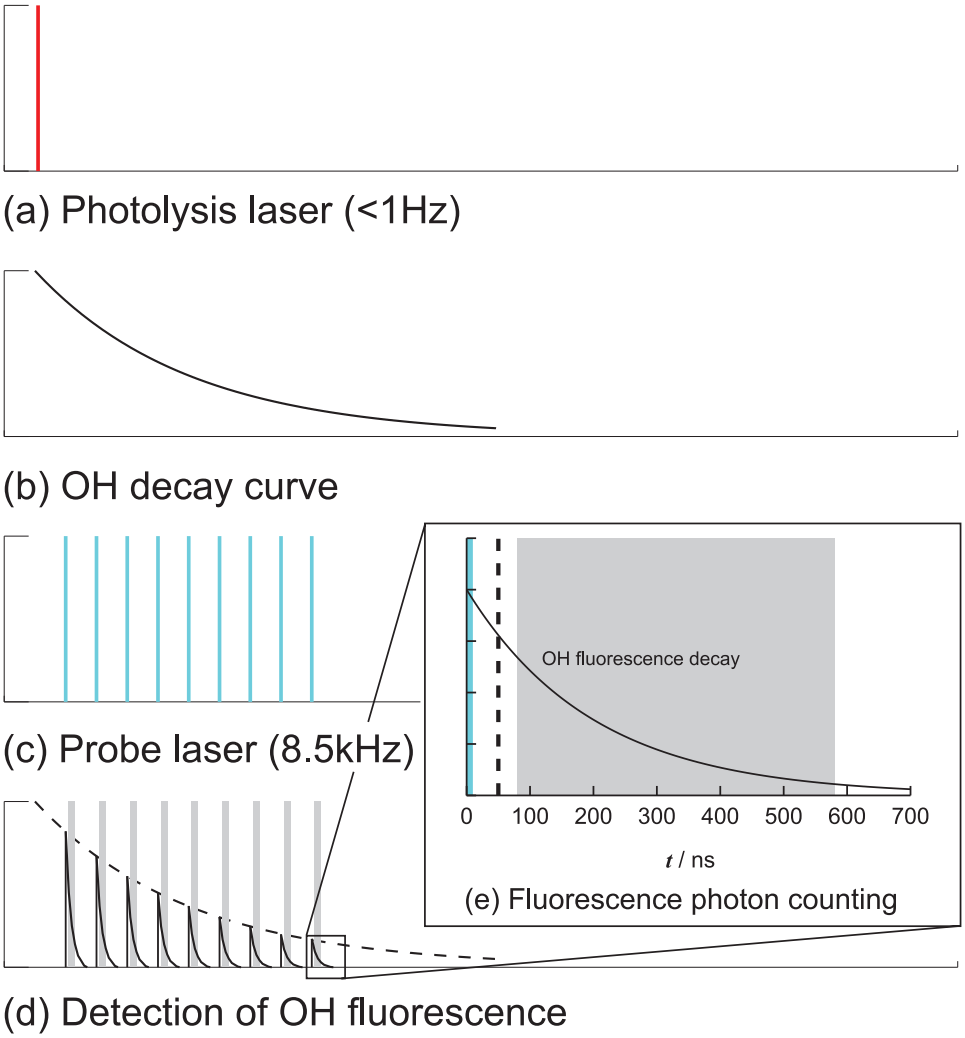

Figure 3.2: Timing concept of the FP/LIF technique for the measurement of k_{OH}. Please note that this is not a true-to-scale representation for the different panels. (a) The 266 nm photolysis laser is operated at a low repetition rate of <1 Hz. (b) An initial OH concentration is formed in the reaction volume virtually instantaneously after the photolysis laser pulse. OH is consumed by reactions with trace gases and decays exponentially. (c) The 308 nm probe laser is operated at a high repetition rate of 8.5 kHz. (d) In the detection cell, OH fluorescence is induced with each probe laser pulse. The dashed line represents the OH decay in the reaction volume that is recorded by time-resolved detection of the fluorescence signal. (e) Enhanced representation of delayed gated fluorescence photon counting (grey shaded area indicates the time slot of photon counting). The cyan vertical line marks the occurrence of the probe laser. The high voltage of the photomultiplier is switched on delayed with respect to the probe laser pulse (marked by the dashed vertical line)

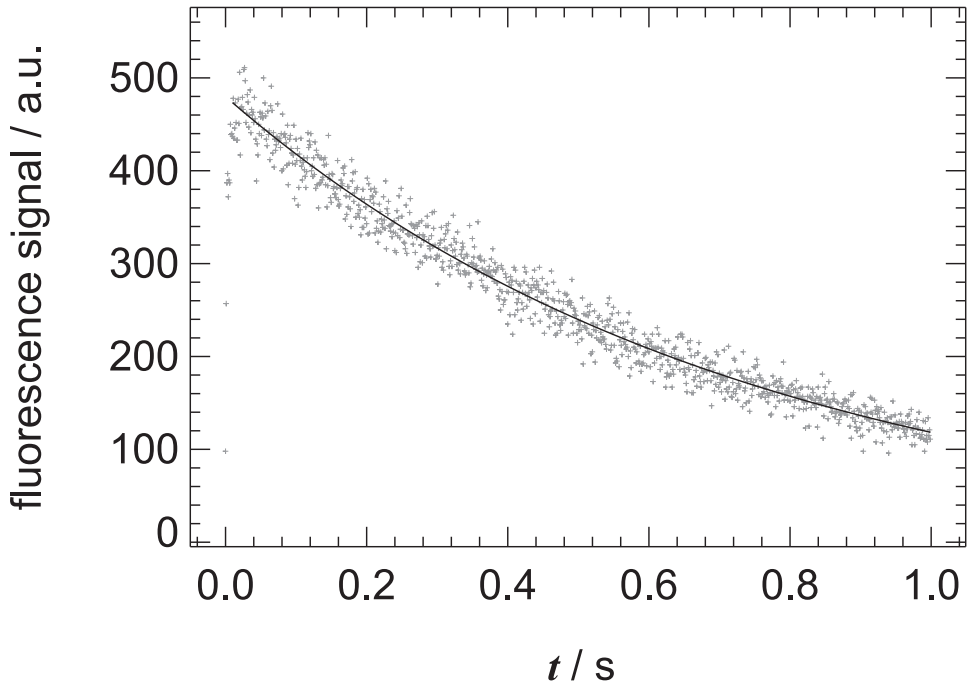

Figure 3.3: OH decay curve obtained in clean synthetic air with traces of O_3 (2×10^{12}cm^{-3}) and H_2O (3×10^{17}cm^{-3}). Crosses represent the recorded raw OH fluorescence signal at a time resolution of 1 ms. The line shows a fit of eq. 3.3 to the data and corresponds to $k_{OH} = 1.5$ s^{-1}. Data from the first 10 ms are not considered in the fit because the signal is not stable in this interval (see text).

($k^0_{HO_2} = 1.5$ s^{-1}) and also assigned to diffusion and wall losses. This HO_2 loss can be determined independently in experiments with CO (see sections 4.1 and 4.2). The nature of k^0_{OH} and $k^0_{HO_2}$ is of secondary importance for the data analysis. Measurements can be corrected for the radical background losses as long as they are reproducible and result in exponential decays. This is the case for the experiments presented here. As shown in fig. 3.3 the signal in the first ≈10 ms after the photolysis laser flash is not stable. This is possibly caused by laser profile inhomogeneities or the local influence of the sampling nozzle on the photolysis laser beam, i.e. the initial distribution of OH radicals, which is then diminished by diffusion and the gas flow through the reaction volume. Therefore, data from this interval immediately after the laser flash are not considered in the evaluation of radical decay curves.

3.8 Possible interferences

The major potential perturbation of the OH reactivity measurement is the formation of HO_2 radicals in the reaction volume and subsequent recycling of OH radicals, e.g. via reaction R7 in the presence of NO. Recycling of OH can result in an apparently smaller k_{OH} because the assumption of an exponential OH decay according to eq. 3.3 is no longer valid. HO_2 can either be formed by photolysis of VOCs at 266 nm or by secondary reactions following OH + VOCs (R5). Photolysis of VOCs results in a rapid HO_2 formation just after the photolysis laser pulse (see section 4.2 for details) whereas secondary reactions following OH + VOC form HO_2 at a comparatively slower rate. In both cases the resulting interference depends on the turnover rate of the HO_2 + NO reaction and thus on the NO concentration in the reaction volume of the OH reactivity instrument. The OH recycling interference can only occur during SAPHIR experiments because the pulsed kinetic studies are performed in the absence of NO in the reaction volume. During a few SAPHIR experiments the sampled air contains peak NO concentrations of 8 ppb. Under those conditions the highest OH recycling rates in the reaction volume and consequently biexponential OH decay curves are expected. A pseudo-first-order OH recycling rate constant of 1.6 s^{-1} (calculated using the NASA recommendation for the HO_2 + NO rate constant[77]) is obtained at the highest NO concentration of 8 ppb and numerical simulations show that the maximum error caused by the OH recycling interference is 8%. However, such high NO levels do not represent typical experimental conditions and only occurred for limited time periods prior to the injection of aromatics into the SAPHIR chamber (see chapter 5 for details). SAPHIR experiments are typically performed at NO concentrations well below 1 ppb where OH reactivity measurements are not perturbed by OH recycling.

4

Pulsed kinetic studies

Within the scope of this work, an experimental procedure and an approach for the data analysis were developed to determine HO_2 formation yields from OH + aromatic hydrocarbon reactions under atmospheric conditions. Briefly, OH and HO_x decay curves are measured alternately in the presence of aromatics using the modified OH reactivity instrument described in chapter 3. CO serves as chemical reference system because the OH + CO reaction is well-investigated and forms HO_2 with unity yield.[78] Prompt HO_2 yields from aromatic hydrocarbons are determined by comparison to CO reference experiments. The determination of HO_2 yields is done by applying analytical solutions and curve fitting procedures. The results of the pulsed kinetic studies on prompt HO_2 formation from aromatics have already been published.[79,80]

4.1 Data analysis and experimental procedure

During the pulsed kinetic experiments the OH reactivity instrument is sampling pure synthetic air from a gas mixing system and single OH reactants of interest are injected into the main gas flow (see section 3.6). In experiments with CO, the OH + CO reaction yields CO_2 and H atoms that are quantitatively converted to HO_2 virtually instantaneously on the time scale of the experiment ($k_{H+O_2} \times [O_2] \approx 6 \times 10^6 s^{-1}$ in air). Thus, OH is effectively converted to HO_2 and the following overall reaction applies:

$$OH + CO + O_2 \longrightarrow HO_2 + CO_2 \qquad \text{(R19)}$$

Generally, all reactants are used in excess over OH, so that pseudo-first-order conditions are assumed. Accordingly, OH is expected to decay exponentially whereas a biexponential expression applies for HO_2.

$$[\mathrm{OH}] = [\mathrm{OH}]_0 \times \exp(-k_{\mathrm{OH}}^{\mathrm{CO}} t) \tag{4.1}$$

$$[\mathrm{HO_2}] = \frac{[\mathrm{OH}]_0 (k_{\mathrm{OH}}^{\mathrm{CO}} - k_{\mathrm{OH}}^{0})}{k_{\mathrm{OH}}^{\mathrm{CO}} - k_{\mathrm{HO_2}}^{0}} \times \left\{ \exp(-k_{\mathrm{HO_2}}^{0} t) - \exp(-k_{\mathrm{OH}}^{\mathrm{CO}} t) \right\} \tag{4.2}$$

$k_{\mathrm{OH}}^{\mathrm{CO}}$ denotes the total OH reactivity in the presence of CO:

$$k_{\mathrm{OH}}^{\mathrm{CO}} = k_{\mathrm{OH+CO}}[\mathrm{CO}] + k_{\mathrm{OH}}^{0} \tag{4.3}$$

k_{OH}^{0} and $k_{\mathrm{HO_2}}^{0}$ are the background loss decay rate constants of OH and HO_2, respectively (see section 3.7). An HO_2 yield of unity for the OH + CO reference reaction is presumed in eq. 4.2.

For OH + VOC reactions in synthetic air similar expressions are derived for the time-dependence of OH and HO_2. Again, HO_2 formation (see reaction R5) is assumed to be effectively undelayed on the timescale of the experiments. This assumption is justified for all VOCs investigated in this work (see section 4.2.1 for details). For example, the intermediately formed AOH from OH + benzene, reacts rapidly with O_2 ($k_{\mathrm{AOH+O_2}} \times [\mathrm{O_2}] \approx 500\ \mathrm{s}^{-1}$ in air).[38] This reaction is even faster for AOH from substituted benzenes.[42] OH and HO_2 decays are described by:

$$[\mathrm{OH}] = [\mathrm{OH}]_0 \times \exp(-k_{\mathrm{OH}}^{\mathrm{VOC}} t) \tag{4.4}$$

$$[\mathrm{HO_2}] = \frac{[\mathrm{OH}]_0 (k_{\mathrm{OH}}^{\mathrm{VOC}} - k_{\mathrm{OH}}^{0}) \phi_{\mathrm{HO_2}}^{\mathrm{VOC}}}{k_{\mathrm{OH}}^{\mathrm{VOC}} - k_{\mathrm{HO_2}}^{0}} \times \left\{ \exp(-k_{\mathrm{HO_2}}^{0} t) - \exp(-k_{\mathrm{OH}}^{\mathrm{VOC}} t) \right\} + [\mathrm{HO_2}]_0 \times \exp(-k_{\mathrm{HO_2}}^{0} t) \tag{4.5}$$

A factor $\phi_{\mathrm{HO_2}}^{\mathrm{VOC}}$ accounts for the unknown yield of prompt HO_2 and a second term considers a potential photolytical formation of HO_2 with an initial concentration of $[\mathrm{HO_2}]_0$ (see section 3.8). Again $k_{\mathrm{OH}}^{\mathrm{VOC}}$ is the total OH reactivity in the presence of the organic compound:

$$k_{\mathrm{OH}}^{\mathrm{VOC}} = k_{\mathrm{OH+VOC}}[\mathrm{VOC}] + k_{\mathrm{OH}}^{0} \tag{4.6}$$

Formation of RO_2 radicals following the OH + VOC reaction (R6) is given by an analogous expression assuming the same background decay rate constant for HO_2 and RO_2 ($k^0_{HO_2} \approx k^0_{RO_2}$) and $\phi^{VOC}_{RO_2}$ instead of $\phi^{VOC}_{HO_2}$.

$$\begin{aligned}[RO_2] &\approx \frac{[OH]_0(k^{VOC}_{OH} - k^0_{OH})\phi^{VOC}_{RO_2}}{k^{VOC}_{OH} - k^0_{HO_2}} \\ &\times \left\{\exp(-k^0_{HO_2}t) - \exp(-k^{VOC}_{OH}t)\right\} \end{aligned} \tag{4.7}$$

Within this work it was found that the LIF detection technique for HO_2 features cross-sensitivity to specific organic peroxy radicals.[79,81] This cross-sensitivity is caused by the conversion of RO_2 to organic alkoxy radicals in the presence of NO in the LIF detection cell (R8). RO radicals resulting from OH + aromatics (biRO, fig. 2.2, I) undergo rapid decomposition to fragments (R9). These fragments again react rapidly with O_2 yielding HO_2 (R10). The potential for an additional LIF signal caused by conversion of RO_2 to HO_2 decreases with decreasing NO concentration in the LIF detection cell. Therefore, the NO concentration in the detection cell is varied over a wide range to identify experimental conditions where the RO_2 cross-sensitivity is widely suppressed. To carefully characterize the contribution of interfering RO_2 to the LIF signal during pulsed kinetic studies using the OH reactivity instrument, isoprene and cyclohexane are chosen as test reactants. Isoprene and cyclohexane are expected to form alkoxy radicals with very different behaviour with regard to HO_2 formation in secondary reactions (see section 4.2.1). Of course, the RO_2 cross sensitivity also affects atmospheric HO_2 measurements by LIF and consequently studies were stimulated investigating the potential interferences for a number of VOCs.[81] Furthermore, HO_2-LIF data obtained during recent field measurements[72,73] are subject to this RO_2 interference and were re-analysed accordingly.[82]

When the OH reactivity instrument is operated in the OH mode (absence of NO in the detection cell), the obtained LIF signal is proportional to the OH concentration.

$$S_{OH} \propto [OH] \tag{4.8}$$

The LIF signal obtained in the HO_x mode of the instrument (NO injected into the detection cell) is given by the sum of the OH signal, the additional signal from HO_2 to OH conversion (R7), and − depending on the experimental conditions and the VOC − the additional signal from RO_2 to OH

conversion (involving reactions R7, R8, R9, and R10).

$$S_{\mathrm{HO_x}} \propto f_{\mathrm{OH}}([\mathrm{OH}] + f_{\mathrm{HO_2}}([\mathrm{HO_2}] + \alpha_{\mathrm{RO_2}}[\mathrm{RO_2}])) \tag{4.9}$$

The factor f_{OH} considers the lower detection sensitivity of OH in the $\mathrm{HO_x}$ mode of the instrument that is possibly caused by formation of nitrous acid via reaction R16. The $\mathrm{HO_2}$ detection sensitivity is typically lower by a factor of $f_{\mathrm{HO_2}}$ compared to that for OH owing to incomplete $\mathrm{HO_2}$ conversion within the available reaction time in the detection cell. The last term in eq. 4.9 accounts for any contribution of interfering $\mathrm{RO_2}$ radicals. $\alpha_{\mathrm{RO_2}}$ depicts the ratio of the detection sensitivities of $\mathrm{RO_2}$ to $\mathrm{HO_2}$. By combining eqs. 4.5, 4.7, and 4.9 the following expression is derived (assuming $[\mathrm{HO_2}]_0 = 0$):

$$\begin{aligned} S_{\mathrm{HO_x}} &\propto f_{\mathrm{OH}}([\mathrm{OH}] + f_{\mathrm{HO_2}}[\mathrm{HO_2}](1 + \alpha_{\mathrm{RO_2}}\phi^{\mathrm{VOC}}_{\mathrm{RO_2}}/\phi^{\mathrm{VOC}}_{\mathrm{HO_2}})) \\ &= f_{\mathrm{OH}}([\mathrm{OH}] + f_{\mathrm{HO_2}}[\mathrm{HO_2}]\ F_{\mathrm{RO_2}}) \end{aligned} \tag{4.10}$$

Taking into account the amplification factor $F_{\mathrm{RO_2}}$, eq. 4.5 is also valid in the presence of interfering $\mathrm{RO_2}$ radicals. By decreasing the NO concentration in the LIF detection cell, the $\mathrm{RO_2}$ to OH conversion is effectively suppressed and $\alpha_{\mathrm{RO_2}}$ approaches zero whereas $F_{\mathrm{RO_2}}$ approaches unity. The product $F_{\mathrm{RO_2}} \times \phi^{\mathrm{VOC}}_{\mathrm{HO_2}} = \Phi^{\mathrm{VOC}}$ is determined by fitting eqs. 4.1, 4.2, 4.4, and 4.5 simultaneously to the respective decay curves obtained in the presence of CO and the VOC of interest. The fits are performed by a Levenberg-Marquardt least squares fitting procedure[83] using $k^0_{\mathrm{OH}} = 1.5\ \mathrm{s^{-1}}$ (measured separately) as constraint.

OH decay curves are recorded immediately before and after the $\mathrm{HO_x}$ decay curves to assure that experimental conditions remain constant. Therefore, the proportionality factors in eqs. 4.8 and 4.9 are identical and treated as a single fit parameter for each pair of S_{OH} and $S_{\mathrm{HO_x}}$. Accordingly, experiments with CO are performed immediately before and after experiments with VOCs to provide for constant experimental conditions in terms of the factors f_{OH} and $f_{\mathrm{HO_2}}$. The decay curves S_{OH} and $S_{\mathrm{HO_x}}$ obtained in the presence of CO basically define the factors f_{OH} and $f_{\mathrm{HO_2}}$ as well as the background loss rate constant $k^0_{\mathrm{HO_2}}$. S_{OH} mainly determine the pseudo-first-order rate constants $k^{\mathrm{CO}}_{\mathrm{OH}}$ and $k^{\mathrm{VOC}}_{\mathrm{OH}}$. $S_{\mathrm{HO_x}}$ recorded in the presence of the VOC determine Φ^{VOC}. Fitting all curves simultaneously assures that all experimental data and their uncertainties are considered adequately.

The fit quality is evaluated from the weighted summed squared residuals χ^2 divided by the degrees of freedom (DOF $\approx$ number of data points) that

should range around unity. Fitting the CO and VOC data together typically results in χ^2/DOF $\approx$ 1.3. The deviation from unity is acceptable and indicates that the errors of the data points that are estimated from Poisson statistics are slightly underestimated. To obtain error estimates for the fitted HO_2 yields, values of Φ^{VOC} are gradually changed and held fixed during the fits until the ratio of χ^2/DOF increases by a factor ($\approx$ 1.03). This factor is taken from a parameterization of the χ^2-distribution for the respective value of DOF to obtain a probability $\approx$0.68.[84] Resulting ranges were expected to correspond to 1σ errors of Φ^{VOC} but numerical simulations show that they represent significantly greater, rather conservative error estimates.

4.2 Results

Fig. 4.1 shows typical examples of S_{OH} and S_{HO_x} decay curves recorded in the presence of CO and several VOCs. The full lines correspond to fitted decays S_{OH} and S_{HO_x} incorporating eqs. 4.1 and 4.2 (panel (a)) as well as eqs. 4.4 and 4.5 (panels (b)-(f)). The red lines show the fitted contributions of HO_2 to S_{HO_x}. Besides the secondary formation following reactions of OH, HO_2 can also be formed by photolysis of aromatics in the presence of O_2. H-atom formation from the 248 nm photolysis of benzene and toluene and subsequent HO_2 formation via H + O_2 has been observed in previous studies.[85–87] Test experiments are performed in the absence of the OH precursor O_3 in order to check whether H-atoms (and subsequently HO_2 radicals) are formed by the 266 nm photolysis of the VOCs used in this work. No HO_2 formation from photolysis of benzene, alkylbenzenes, isoprene, and cyclohexane at 266 nm is observed and $[HO_2]_0$ in eq. 4.5 is set to zero (see section 4.2.1). In contrast, the 266 nm photolysis of hydroxybenzenes leads to instantaneous HO_2 formation as shown in panel (d) for the example 2,5-dimethylphenol (green points). This photolytically produced HO_2 is at significant levels compared to the secondarily formed HO_2 and is considered quantitatively in the evaluation of experiments with hydroxybenzenes (see section 4.2.2).

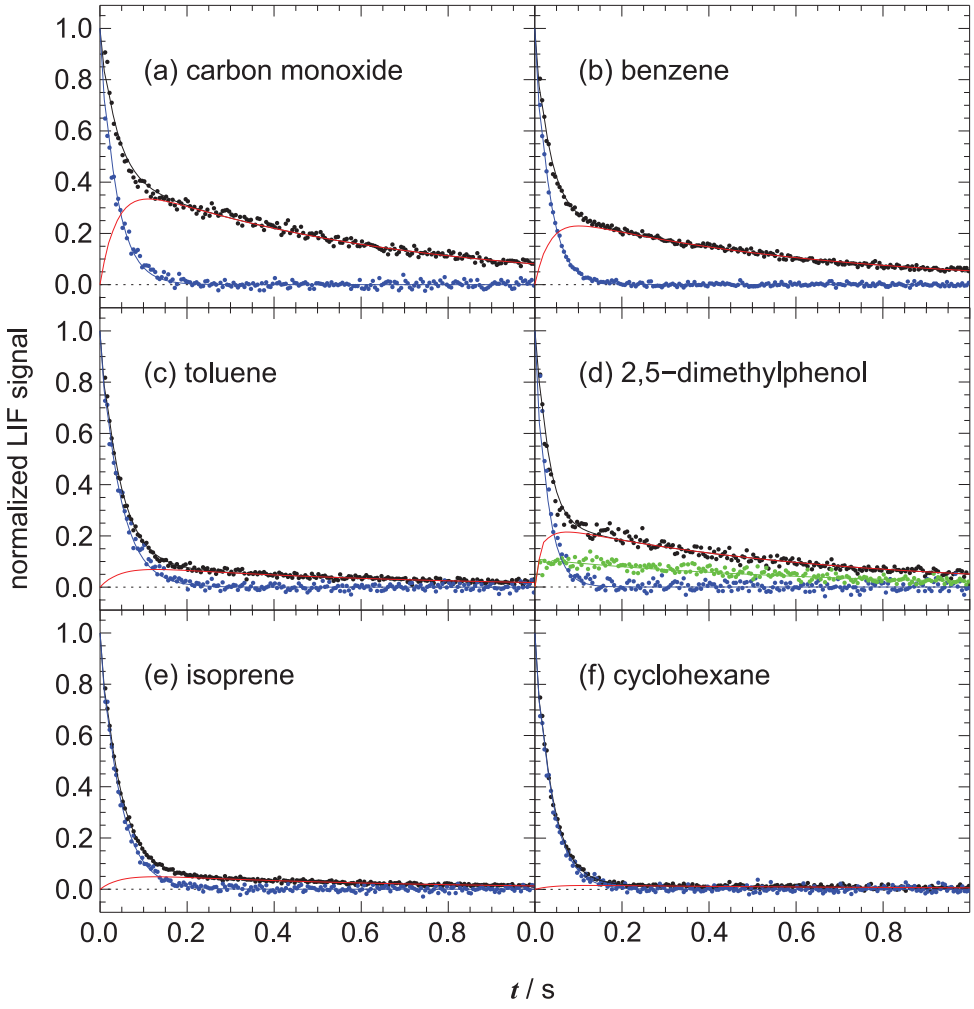

Figure 4.1: Normalized S_{OH} (blue points) and S_{HO_x} (black points) obtained in the presence of CO, benzene, toluene, 2,5 - dimethylphenol, isoprene, and cyclohexane in synthetic air in the absence of NO in the reaction volume. The NO concentration in the LIF detection cell is $\leq 1.2\times10^{14}$cm^{-3} in each experiment. The green points in (d) represent S_{HO_x} obtained in the absence of the OH precursor O_3, i.e. from photolytical HO_2 formation observed for this phenol compound. Full lines show fits to the data points according to eqs. 4.1, 4.2, 4.4, and 4.5 (see text). The red lines show the fitted contributions of HO_2 to S_{HO_x}. (a) is the corresponding reference experiment for (b). For (c)-(f) these experiments are not shown.

4.2.1 HO_2 formation from OH + benzene and alkylbenzenes

Tables 4.1 and 4.2 show the fit results of combined CO/VOC experiments performed in synthetic air at different NO concentrations in the LIF detection cell ($[NO]_D$). A typical value of $f_{OH} = 0.8 \pm 0.1$ is found and no strong dependence on $[NO]_D$ is observed. This is expected because the OH radical losses due to HNO_2 formation (see reaction R16) are of minor importance in the detection cell. f_{HO_2} is found to increase with increasing $[NO]_D$ reaching maximum values of about 1.6. This observation can be rationalized by greater OH losses at the sampling nozzle compared to that for HO_2 and is consistent with previous studies.[81,88,89] To reproduce the increase of f_{HO_2} with $[NO]_D$, an analytical solution is derived for the HO_2 to OH conversion in the detection cell (reaction R7) that also considers an OH loss via reaction R16:

$$\frac{[OH](t_D)}{[HO_2](t_D = 0)} = f_{HO_2} = \gamma \frac{k_{HO_2+NO}}{k_{OH+NO} - k_{HO_2+NO}} \times \left\{\exp(-k_{HO_2+NO}[NO]t_D) - \exp(-k_{OH+NO}[NO]t_D)\right\} \quad (4.11)$$

The factor f_{HO_2} in eq. 4.11 is given by the ratio of [OH] to $[HO_2](t_D = 0)$, the HO_2 starting concentration entering the detection cell. For convenience it is assumed that only HO_2 is sampled ($[OH](t_D = 0)$ set to zero). An additional factor γ is introduced to allow for values of $f_{HO_2} > 1$. By fitting eq. 4.11 to all f_{HO_2} listed in tables 4.1 and 4.2, a reaction time in the detection cell of $t_D \approx 240$ μs and a factor of $\gamma \approx 1.5$ are obtained. The relevant rate constants (see table 4.3) and $[NO]_D$ are used as constraints. However, the reaction time in the detection cell should be considered effective because it is determined assuming ideal mixing of NO added to the supersonic gas expansion. The possible influence of inhomogeneities and turbulences is neglected. Ideal mixing cannot be verified because $[NO]_D$ is calculated and not measured directly. As shown in fig 4.2 the model (full line) is not able to reproduce the measured f_{HO_2} (symbols) perfectly but the general $[NO]_D$ dependence is described to a good approximation. The reaction time t_D for radical conversions in the detection cell and the factor γ determined here are similar to previous results obtained with a comparable setup.[81,90] t_D will be used for the numerical simulations of RO_2 interferences as outlined below.

Table 4.1: Fit results of f_{OH}, f_{HO_2}, k_{OH}^{VOC} and Φ^{VOC} from combined CO/ VOC experiments in synthetic air at different NO concentrations $[NO]_D$ in the LIF detection cell. Results are obtained by fitting eqs. 4.1, 4.2, 4.4, and 4.5 to the S_{OH} and S_{HO_x} decay curves. Numbers in bold face indicate the prompt HO_2 yields at $F_{RO_2} \approx 1$.

Reactant	$[NO]_D$ $/10^{14}$ cm^{-3}	f_{OH}	f_{HO_2}	k_{OH}^{VOC} / s^{-1}	$\Phi^{VOC} = \phi_{HO_2}^{VOC} F_{RO_2}$	χ^2/DOF
Cyclohexane	1.2	0.94	0.53	26.7	**0.04±0.02**	1.22
	30.3	0.86	1.50	29.5	0.11±0.02	1.74
Isoprene	0.4	0.86	0.23	27.5	0.11±0.04	1.15
	1.2	0.92	0.45	22.7	0.15±0.02	1.25
	–	–	–	–	**0.13±0.03***	–
	3.9	0.87	0.75	32.4	0.30±0.04	1.26
	6.6	0.77	0.98	32.0	0.44±0.06	1.33
	15.0	0.79	1.39	29.0	0.69±0.10	1.62
	23.7	0.73	1.63	26.7	0.93±0.15	1.86
	30.3	0.79	1.62	18.5	0.96±0.11	2.15
Benzene	0.4	0.85	0.23	20.9	0.69±0.10	1.09
	1.2	0.91	0.45	31.0	0.67±0.08	1.30
	–	–	–	–	**0.68±0.09***	–
	3.9	0.86	0.75	21.2	0.77±0.10	1.24
	6.6	0.81	0.96	21.1	0.84±0.09	1.19
	15.0	0.82	1.36	20.1	0.81±0.09	1.30
	23.7	0.73	1.63	20.0	0.81±0.08	1.21
	30.3	0.80	1.61	28.6	0.87±0.08	1.57
Toluene	0.12	0.84	0.22	22.3	0.42±0.07	1.20
	0.12	0.89	0.20	72.2	0.40±0.13	1.23
	1.2	0.85	0.63	43.8	0.45±0.14	1.16
	–	–	–	–	**0.42±0.11***	–
	3.9	0.87	0.94	20.1	0.56±0.11	1.17
	9.7	0.89	1.30	17.0	0.62±0.10	1.21
	15.0	0.81	1.46	17.9	0.77±0.13	1.27

* Mean values and mean errors of measurements at $[NO]_D \leq 1.2 \times 10^{14}$cm^{-3}.

Table 4.2: Table 4.1 continued.

Reactant	$[NO]_D$ $/10^{14}$ cm^{-3}	f_{OH}	f_{HO_2}	k_{OH}^{VOC} / s^{-1}	$\Phi^{VOC} = \phi_{HO_2}^{VOC} F_{RO_2}$	χ^2/DOF
Ethylbenzene	0.12	0.86	0.14	17.9	**0.53±0.10**	1.17
o-Xylene	0.12	0.97	0.15	56.4	**0.41±0.08**	1.28
m-Xylene	0.12	0.95	0.18	74.5	**0.27±0.06**	1.23
p-Xylene	0.12	0.87	0.22	25.9	0.43±0.06	1.20
	0.12	0.85	0.19	74.1	0.42±0.15	1.28
	1.2	1.00	0.67	25.8	0.36±0.06	1.18
	–	–	–	–	**0.40±0.09***	–
	3.9	0.94	1.01	25.9	0.44±0.09	1.15
	9.7	0.91	1.34	25.0	0.58±0.11	1.28
	15.	0.83	1.43	25.7	0.67±0.16	1.31
1,2,3-TMB	0.12	0.97	0.18	38.7	**0.31±0.06**	1.28
1,2,4-TMB	0.12	0.95	0.17	53.3	**0.37±0.09**	1.33
1,3,5-TMB	0.12	0.83	0.19	64.3	0.34±0.10	1.17
	0.12	0.93	0.21	18.2	0.37±0.06	1.14
	0.24	0.89	0.27	50.4	0.25±0.06	1.31
	1.2	0.82	0.69	65.2	0.21±0.08	1.19
	–	–	–	–	**0.29±0.08***	–
	2.7	0.85	1.19	42.7	0.31±0.07	2.07
	3.9	0.81	1.06	50.8	0.34±0.12	1.19
	9.7	0.90	1.31	48.4	0.52±0.19	1.38
	15.0	0.85	1.46	28.5	0.67±0.15	1.28
HMB	0.12	0.88	0.14	30.0	0.32±0.08	1.35
	0.12	0.94	0.15	17.2	0.32±0.09	1.24
	0.39	0.99	0.21	18.7	0.33±0.06	1.25
	–	–	–	–	**0.32±0.08***	–

* Mean values and mean errors of measurements at $[NO]_D \leq 1.2 \times 10^{14}$cm^{-3}.

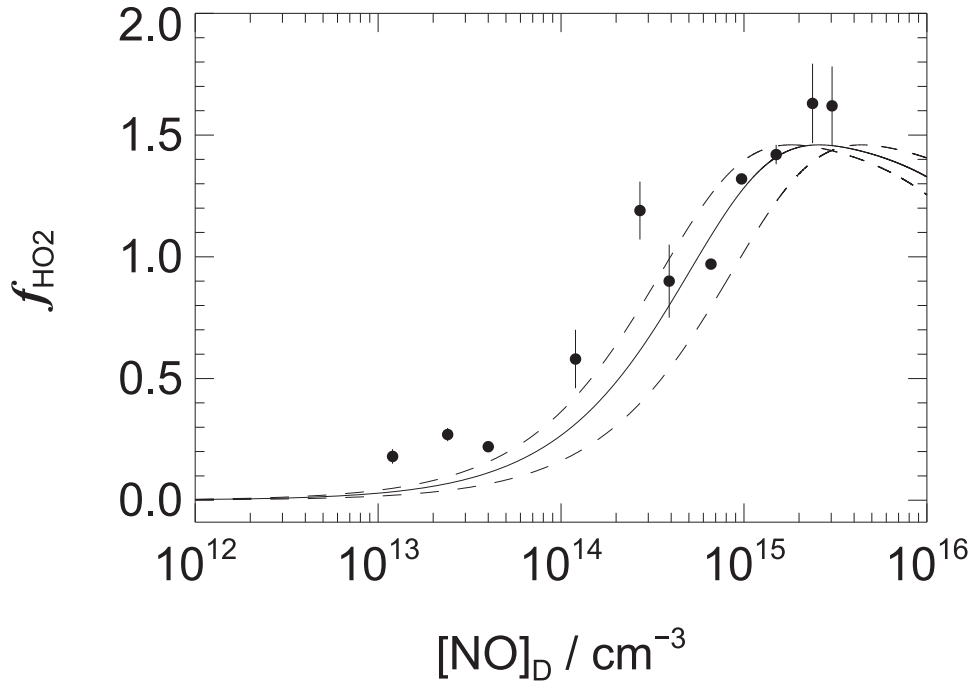

Figure 4.2: Dependence of f_{HO_2} determined in combined CO/VOC experiments on $[NO]_D$, the NO concentration in the LIF detection cell. Symbols show mean values and corresponding standard deviations of f_{HO_2} as listed in tables 4.1 and 4.2. The solid line shows a fit of eq. 4.11 to f_{HO_2} using k_{HO_2+NO}, k_{OH+NO}, and $[NO]_D$ as constraints. The fit is weighted by the experimental errors and a reaction time of $t_D = 240$ μs is obtained. Dashed lines represent results of sensitivity runs where the reaction time t_D is varied by ± 100 μs.

Φ^{VOC} obtained in experiments with isoprene, benzene, toluene, *p*-xylene, and 1,3,5-TMB exhibit a significant dependence on $[NO]_D$ indicating contributions of interferences caused by the presence of RO_2 radicals (see fig. 4.3). In combined CO/cyclohexane experiments, Φ^{VOC} is hardly increased at elevated $[NO]_D$. Numerical simulations taking into account the reactions in the LIF detection cell are performed to reproduce the NO dependence of the different Φ^{VOC}. Rate constants and experimental conditions used for the numerical simulations are listed in table 4.3. All model runs are performed on the basis of t_D, the estimated reaction time. The model is initialized with current recommendations from literature regarding the yields of prompt HO_2 and RO_2: $\phi^{VOC}_{RO_2}/\phi^{VOC}_{HO_2} = 0.35/0.65$ for benzene, $\phi^{VOC}_{RO_2}/\phi^{VOC}_{HO_2} = 0.72/0.28$ for toluene and *p*-xylene and $\phi^{VOC}_{RO_2}/\phi^{VOC}_{HO_2} = 0.82/0.18$ for 1,3,5-TMB.[27,28] For cyclohexane and isoprene the numerical simulations are initialized with $\phi^{VOC}_{RO_2} = 1$.[91]

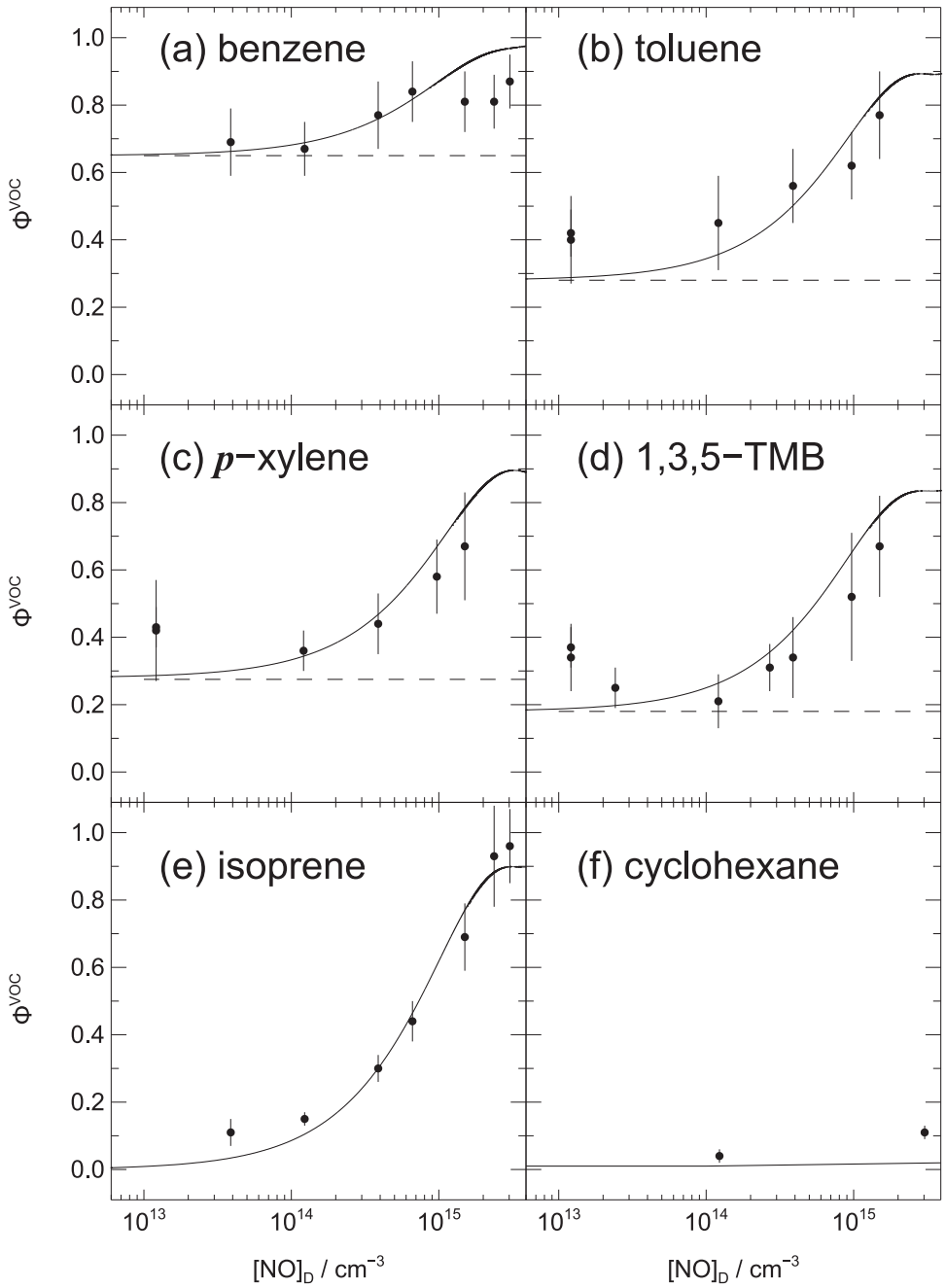

Figure 4.3: Dependence of fitted Φ^{VOC} on $[\mathrm{NO}]_{\mathrm{D}}$, the NO concentration in the LIF detection cell. Symbols show results of combined CO/VOC experiments. The solid lines show the simulated $[\mathrm{NO}]_{\mathrm{D}}$ dependence of Φ^{VOC} based on the reactions in table 4.3. The dashed lines indicate the presumed contribution of $\phi^{\mathrm{VOC}}_{\mathrm{HO_2}}$ to Φ^{VOC} following the OH + aromatic hydrocarbon reaction based on MCM[27,28] recommendations.

Table 4.3: Reactions and reaction rate constants for radical conversions in the LIF detection cell used for the simulation of interferences from organic peroxy radicals. Rate constants are calculated for a temperature of 298 K. Prompt HO_2 yields correspond to MCM recommendations.

Reaction	k		
$HO_2 + NO \longrightarrow OH + NO_2$	8.1×10^{-12} cm^3s^{-1} [a]		
$OH + NO \longrightarrow HONO$	5.7×10^{-14} cm^3s^{-1} [a,b]		
$OH + NO_2 \longrightarrow HNO_3$	1.4×10^{-13} cm^3s^{-1} [a,b]		
	Aromatics[c]	**Isoprene**	**Cyclohexane**
$RO_2 + NO \longrightarrow RO + NO_2$	7.7×10^{-12} cm^3s^{-1} [d]	7.7×10^{-12} cm^3s^{-1} [d]	7.8×10^{-12} cm^3s^{-1} [d]
$RO_2 + NO \longrightarrow RNO_3$	1.3×10^{-12} cm^3s^{-1} [d]	8.5×10^{-13} cm^3s^{-1} [d]	6.6×10^{-13} cm^3s^{-1} [d]
$RO \longrightarrow$ fragments	1×10^6 s^{-1} [d]	1×10^6 s^{-1} [e]	–
RO, fragments $+O_2 \longrightarrow HO_2$	9.1×10^{-12} cm^3s^{-1} [f]	9.1×10^{-12} cm^3s^{-1} [g]	7.7×10^{-15} cm^3s^{-1} [h]
ϕ_{HO_2}	0.65/0.28/0.18 [i]	0	0

[a] NASA recommendation.[77]
[b] Calculated for a total pressure of 3.5 mbar.
[c] Listed rate constants apply for toluene, *p*-xylene, and 1,3,5-TMB.
[d] MCM recommendation.[92]
[e] MCM recommendation[92] for RO $\longrightarrow$ fragment + CH_2OH (assumed main reaction).
[f] Rate constant assumed similar to that for $CH_2OH + O_2$.[g]
[g] NASA recommendation[77] for $CH_2OH + O_2 \longrightarrow HCHO + HO_2$.
[h] MCM recommendation[92] for $RO + O_2 \longrightarrow$ cyclohexanone + HO_2.
[i] Prompt HO_2 yield from OH + benzene/toluene and *p*-xylene/1,3,5-TMB.[92]

The full lines in fig. 4.3 show calculated OH concentrations normalized to a reference case where only HO_2 radicals are entering the LIF detection cell. The dashed lines indicate the recommended prompt HO_2 yields from aromatic hydrocarbons and the calculated Φ^{VOC} expectedly approach these limits at decreasing $[NO]_D$, confirming the vanishing influence from organic peroxy radicals, i.e. $\Phi^{VOC} \approx \phi^{VOC}_{HO_2}$ at low $[NO]_D$.

In the case of benzene, the Φ^{VOC} show a slight dependence on $[NO]_D$. The increase at elevated $[NO]_D$ is assigned to subsequent reactions of the bicyclic peroxy radicals (biRO$_2$). The calculations quantifying the RO_2 conversion efficiency are in good agreement with the experimental results. The behaviour of Φ^{VOC} towards low $[NO]_D$ is in excellent agreement with the measurements whereas at $[NO]_D$ exceeding 10^{15}cm^{-3} the model slightly overpredicts Φ^{VOC}. The model calculations indicate that the limiting value is already reached in good approximation at $[NO]_D \leq 1.2\times10^{14}$cm^{-3}, i.e. $\Phi^{benzene} = \phi^{benzene}_{HO_2}$. A further reduction of $[NO]_D$ is not useful since it results in HO_2 sensitivity factors of $f_{HO_2} \leq 0.24$, so that S_{OH} and S_{HO_x} hardly differ. For toluene, *p*-xylene, and 1,3,5-TMB the model calculations are also in good agreement with the experimental Φ^{VOC} with a single exception of $\Phi^{1,3,5-TMB}$ obtained at the lowest $[NO]_D$ that is slightly greater than predicted by the numerical simulations. The reason for this behaviour is not clear. However, considering all data obtained in combined CO/alkylbenzene experiments it becomes obvious that Φ^{VOC} within experimental uncertainties already level out at $[NO]_D \approx 1 - 2 \times 10^{14}$cm^{-3}. For benzene, toluene, *p*-xylene, and 1,3,5-TMB, the final prompt HO_2 yields are therefore determined by averaging the results obtained at $[NO]_D \leq 1.2 \times 10^{14}$cm^{-3} (bold face in tables 4.1 and 4.2). For the other alkylbenzenes listed in table 4.2, the full dependence of Φ^{VOC} on $[NO]_D$ is not investigated and most experiments are performed at $[NO]_D = 0.12 \times 10^{14}$cm^{-3}.

In addition to experiments with aromatic hydrocarbons, isoprene is used as a reference compound. OH + isoprene gives isoprene peroxy radicals with about unity yield. In the presence of NO, these radicals are converted to isoprene-derived alkoxy radicals that undergo rapid decomposition to fragments. One of these fragments, CH_2OH, again reacts rapidly with O_2 to form HO_2 + HCHO. This reaction sequence is very similar for peroxy radicals from OH + aromatics where HO_2 formation also proceeds via fragmentation of intermediately formed bicyclic alkoxy radicals (biRO) and a fast subsequent O_2 reaction step. Therefore, isoprene experiments are consulted to check whether the limiting behaviour of Φ^{VOC} towards low $[NO]_D$ can be reproduced correctly by the numerical model. As shown in fig. 4.3, the experimentally obtained Φ^{VOC} in the case of isoprene are consistent with the model simula-

tions and approach zero in good approximation at low $[NO]_D$. The minimum value of 0.11±0.04 obtained at the lowest $[NO]_D$ could hint towards a minor, direct HO_2 formation with an upper limit $\phi_{HO_2}^{isoprene} \leq 0.10$. Nevertheless, a residual interference from peroxy radicals that is not accounted for in the numerical model can also not be excluded.

In contrast to isoprene, the further test reactant cyclohexane is expected to form HO_2 significantly slower in secondary reactions of peroxy radicals in the presence of NO because of a much slower RO + O_2 reaction with no preceding RO decomposition (see table 4.3). In agreement with that, the observed Φ^{VOC} are very small with hardly any increase at elevated $[NO]_D$, although calculations slightly underpredict the observed values. Again, this can be explained by an upper limit $\phi_{HO_2}^{cyclohexane} \leq 0.05$ or model deficiencies underestimating RO_2 interferences.

In summary, small residual RO_2 interferences ($\alpha_{RO_2} \leq 0.1$) cannot be excluded even at the lowest possible $[NO]_D$ concentrations because of an incomplete understanding of transport processes within the LIF detection cell (e.g. turbulence induced by the gas-expansion and NO mixing effects).[81] The prompt HO_2 yields determined in this work should therefore be considered upper rather than lower limits.

Table 4.4: Fit results of f_{OH}, f_{HO_2}, k_{OH}^{VOC} and Φ^{VOC} from combined CO/ hydroxybenzene experiments in synthetic air at $[NO]_D = 0.12 \times 10^{14} cm^{-3}$ in the LIF detection cell. Results are obtained by fitting eqs. 4.1, 4.2, 4.4, and 4.5 to the S_{OH} and S_{HO_x} decay curves.

Reactant	$[HO_2]_0/[OH]_0$	f_{OH}	f_{HO_2}	k_{OH}^{VOC} / s^{-1}	$\Phi^{VOC} \approx \phi_{HO_2}^{VOC}$	χ^2/DOF
Phenol	0.33	0.88	0.33	7.9	0.89±0.29	1.36
	0.83	0.81	0.32	18.4		
o-Cresol	0.37	0.80	0.20	9.2	0.87±0.29	1.48
	0.81	0.98	0.23	17.4		
2,5-Dimethyl-phenol	0.20	0.90	0.20	15.8	0.72±0.12	1.23
	0.55	1.02	0.20	38.6		
2,4,6-Trimethyl-phenol	0.01	0.93	0.19	15.8	0.45±0.13	1.28
	0.03	0.93	0.23	81.6		

4.2.2 HO_2 formation from OH + hydroxybenzenes

Table 4.4 shows fit results of combined CO/hydroxybenzene experiments revealing that the yields of promptly formed HO_2 are much greater than those for the alkylbenzenes with a single exception for 2,4,6-trimethylphenol. Moreover, an instantaneous photolytical HO_2 formation is observed in experiments without the OH precursor ozone (see fig. 4.1 (d) for the example 2,5-dimethylphenol). Consequently, S_{HOx} curves recorded in the presence of ozone are also expected to contain an underlying contribution from photolytically produced HO_2. This photolytical contribution is accounted for in the data analysis by $[HO_2]_0$ in eq. 4.5 that is assumed to depend linearly on the concentration of the aromatic hydrocarbon. In a first approach, measurements are therefore performed at two different aromatic hydrocarbon concentrations and two S_{OH} and S_{HOx} decay curves each are recorded. Two sets of eqs. 4.1, 4.2, 4.4, and 4.5 are obtained and fitted simultaneously by assuming $[HO_2]_0 \propto [VOC]$ and treating the proportionality factor as an additional fit parameter. However, the error limits obtained by this fitting strategy are significantly greater than in the case of the alkylbenzene experiments and approach 100%. Expectedly, it is difficult to distinguish between photolytically and secondarily formed HO_2 and the large mutual dependence of the respective contributions leads to increased error limits. An extended evaluation procedure is therefore adopted where also the decay curves S_{HOx} obtained in the absence of the OH precursor ozone are implemented in the fits by setting $[OH]_0$=0 in eq. 4.5. This leads to similar results with im-

proved error limits as listed in table 4.4. $[NO]_D$ are always kept low during the experiments with hydroxybenzenes and the extracted HO_2 yields can be considered prompt formation yields: $\Phi^{VOC} \approx \phi^{VOC}_{HO_2}$. Because prompt HO_2 yields are greater compared to the alkylbenzenes, any residual contribution of RO_2 interferences is expected to be even smaller and negligible.

4.3 Discussion

Measurements of HO_2 yields upon the OH + aromatic hydrocarbon reactions in synthetic air in the absence of NO are used to investigate the branching ratios of primary oxidation steps. The extracted ϕ_{HO_2} should match the combined yields of currently proposed HO_2 co-products. Fig. 4.4 schematically depicts the mechanism in terms of prompt HO_2 and its co-products as well as competing reaction channels.

From OH + benzene these co-products are phenol and epoxide compounds:

$$\phi^{benzene}_{HO_2} = \phi_{phenol} + \phi_{epoxide} \tag{4.12}$$

In the case of OH + alkylbenzenes, formation of oxepins is postulated as an additional pathway (see fig. 2.1):

$$\phi^{alkylbenzene}_{HO_2} = \phi_{phenol} + \phi_{epoxide} + \phi_{oxepin} \tag{4.13}$$

On the other hand, the remainder $(1 - \phi_{HO_2})$ should match the combined yields of reaction channels not associated with prompt HO_2 formation. From OH + benzene, formation of glyoxal via the bicyclic peroxy radical ($biRO_2$) channel is the only pathway that is not linked with prompt HO_2:

$$1 - \phi^{benzene}_{HO_2} = \phi_{glyoxal} \tag{4.14}$$

From OH + alkylbenzenes, the bicyclic peroxy radical channel leading to α-dicarbonyls (α-DCs, i.e. glyoxal, methylglyoxal, dimethylglyoxal), the H-atom abstraction finally forming benzaldehydes, and the dealkylation are not associated with prompt HO_2 (see fig. 2.1):

$$1 - \phi^{alkylbenzene}_{HO_2} = \phi_{\alpha-DC} + \phi_{benzaldehyde} + \phi_{dealkylation} \tag{4.15}$$

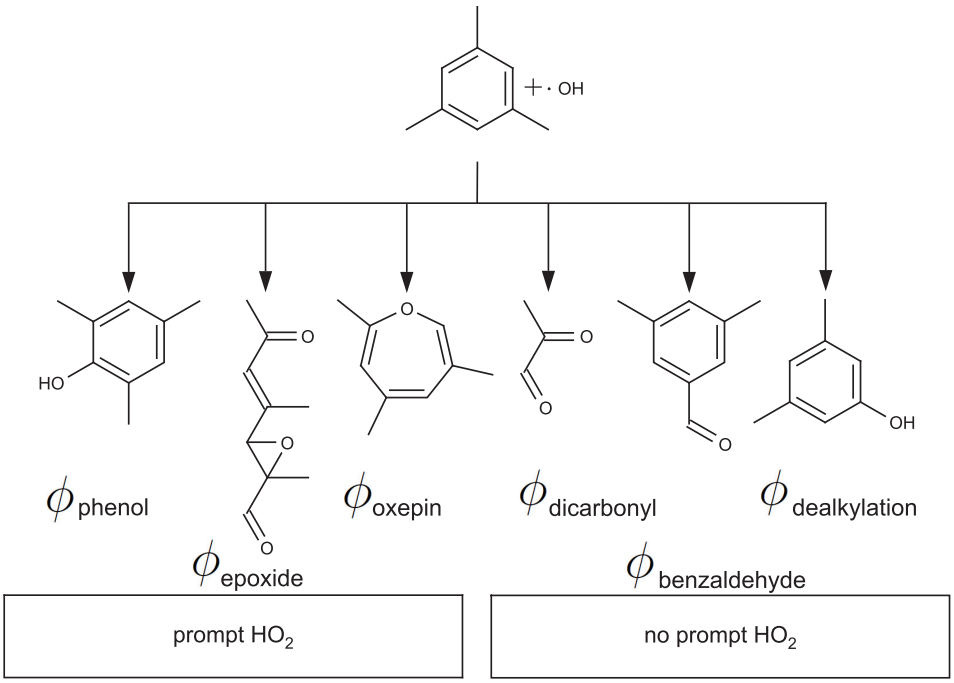

Figure 4.4: Schematic representation of the atmospheric oxidation mechanism of aromatic hydrocarbons using the example of 1,3,5-TMB. Major reaction pathways are grouped into prompt HO_2 channels and reaction channels not associated with prompt HO_2.

4.3.1 OH + benzene

The HO_2 yield of $\phi_{HO_2}^{benzene}$= 0.68±0.09 obtained following the OH + benzene reaction is similar to a phenol yield of 0.53±0.07 determined in chamber experiments (Volkamer et al.[25]) and to phenol yields determined in flow-tube experiments of 0.61±0.07 (Berndt and Böge[46]) and 0.51±0.04 (Noda et al.[32]). Because HO_2 is the expected co-product of phenol formation, this result is consistent with the currently proposed mechanism. Considerably lower phenol yields of about 0.2−0.3 were reported in former studies by Atkinson et al.[93], Bjergbakke et al.[94], and Berndt and Böge[95](see table 4.5). Most likely, these deviating values result from the different experimental conditions in the respective studies leading to different chemical mechanisms that were not considered in the data evaluation. For example, Bjergbakke et al.[94] and Berndt and Böge[95] used high initial radical concentrations and an influence of radical-radical reactions on the phenol yield cannot be ruled out. In the study by Atkinson et al.[93] high initial NO_2 concentrations were deployed and the AOH + NO_2 reaction was not accounted for in the data analysis. The data reported by Volkamer et al.[24,25] are implemented in the

Table 4.5: Product yields of the OH-initiated oxidation of benzene in the presence of O_2 from literature.

Reference	**Prompt HO_2**		**No prompt HO_2**
	ϕ_{phenol}	ϕ_{epoxide}	ϕ_{glyoxal}
OH + benzene			
Atkinson et al.[93]	0.24±0.04	–	–
Bjergbakke et al.[94]	0.25±0.05	–	–
Berndt and Böge[95]	0.30±0.02	–	0.22±0.02
Volkamer et al.[24]	–	–	0.35±0.10
Volkamer et al.[25]	0.53±0.07	–	–
Berndt and Böge[46]	0.61±0.07	–	0.29±0.10
Noda et al.[32]	0.51±0.04	–	–
Birdsall et al.[49]	$\approx 0.50^a$	$\approx 0.07^a$	–
This study	$\phi_{HO_2} = 0.68 \pm 0.09$		$(1 - \phi_{HO_2}) = 0.32 \pm 0.09$

[a] Relative product yield.

current MCM. On the basis of these values, Bloss et al.[28] further assigned a yield of epoxides of 0.12 to close the budget for the OH-initiated degradation of benzene. Taking the data by Berndt and Böge,[46] a similar epoxide yield of about 0.10 is obtained. Because formation of epoxides is also associated with HO_2 formation with no preceding NO reaction, the approach by Bloss et al.[28] is in accordance with the results of this work. Regarding the error of $\phi_{HO_2}^{\text{benzene}}$, the result can only give a hint towards a minor, but potentially significant (>10%) epoxide formation. Recently, Birdsall and Elrod[49] observed epoxide formation as a minor reaction channel of the OH + benzene reaction in a flow-tube study. This further confirms the result of this work.

The remainder $1-\phi_{HO_2}^{\text{benzene}}$= 0.32±0.09 corresponds very well to an observed yield of glyoxal of 0.35±0.10 from chamber experiments by Volkamer et al.[24] under low NO_x conditions and a glyoxal yield of 0.22±0.02[95] and 0.29±0.10[46] by Berndt and Böge from flow-tube experiments in the presence of NO. Glyoxal is formed from the $biRO_2$ + NO reaction and is therefore not associated with prompt HO_2.

4.3.2 OH + toluene and ethylbenzene

For the OH + toluene reaction $\phi_{HO_2}^{\text{toluene}}$= 0.42±0.11 is obtained. This yield is significantly greater than ϕ_{phenol} (i.e. cresol) of 0.18−0.28 reported in most product studies[32,33,44,47,93,97] (see table 4.6) except for two studies[96,98] re-

Table 4.6: Product yields of the OH-initiated oxidation of toluene in the presence of O_2 from literature.

Reference	Prompt HO_2		No prompt HO_2		
	ϕ_{phenol} (*a*)	ϕ_{epoxide} (*b*)	$\phi_{\alpha-\text{DC}}$ (*c*)	$\phi_{\text{benzaldehyde}}$	$\phi_{\text{dealkylation}}$ (*d*)
OH + toluene					
Atkinson et al.[93]	0.25±0.03	–	–	0.07±0.01	–
Seuwen et al.[96]	0.53±0.08[e]	–	0.10±0.02	0.05±0.01	–
Smith et al.[44]	0.18±0.01	–	0.41±0.03	0.06±0.01	–
Klotz et al.[97]	0.18±0.03	–	–	0.06±0.01	–
Moschonas et al.[98]	0.09±0.03	–	–	0.08±0.01	–
Volkamer et al.[24]	–	–	0.39±0.10[g]	–	–
Noda et al.[32]	0.18±0.02	–	–	–	0.05±0.01
Baltaretu et al.[47]	0.28±0.06	0.07±0.03	0.30±0.10[h]	0.05±0.02	–
Birdsall et al.[33]	≈ 0.27[f]	≈ 0.05[f]	–	≈ 0.04[f]	≈ 0.09[f]
Nishino et al.[99]	–	–	0.48±0.03	–	–
This study	$\phi_{HO_2} = 0.42 \pm 0.11$		$(1 - \phi_{HO_2}) = 0.58 \pm 0.11$		

[a] Sum of *o*-, *m*- and *p*-cresol (unless otherwise stated).
[b] 2-methyl-2,3-epoxy-6-oxo-4-hexenal.
[c] Sum of glyoxal and methylglyoxal (unless otherwise stated). [d] Phenol.
[e] Sum of *o*- and *p*-cresol. [f] Relative product yield. [g] Glyoxal.
[h] Prediction for α-dicarbonyl formation upon a second OH attack.

porting considerably greater and smaller values. However, these two studies are supposed not to be representative for atmospheric conditions because of a potential influence of heterogeneous reactions[96] and losses of primary oxidation products by reaction with OH.[98] The result of this study is consistent with the currently proposed toluene degradation mechanism where the co-products of prompt HO_2 are cresols and an epoxide. By comparison of $\phi_{HO_2}^{\text{toluene}}$ to the reported cresol yields, formation of 0.14−0.24 of other HO_2 co-products is possible. Flow-tube studies by Baltaretu et al.[47] and Birdsall et al.[33] indeed reported experimental evidence for the epoxide pathway. The combined yield of cresol and epoxide of 0.35±0.07[47] is similar to $\phi_{HO_2}^{\text{toluene}}$ determined in this work. Bloss et al.[28] estimated a combined yield of 0.28 for cresol and epoxide based on the data by Volkamer et al.[24] to close the budget for the OH-initiated degradation of toluene. This value is slightly lower than the result of this study. Owing to the uncertainties of the primary product yields, it cannot be ruled out that there are further reaction channels yielding prompt HO_2 like the oxepin pathway proposed by Klotz et al.[51,54,100]. This reaction channel has so far only been excluded for OH + benzene[52] but is

theoretically supported for toluene by quantum chemical computations.[101]

The remainder $1 - \phi_{HO_2}^{toluene} = 0.58 \pm 0.11$ is also somewhat greater than the combined yields of $\phi_{\alpha-DC} + \phi_{benzaldehyde}$ determined in product studies: 0.47 ± 0.03[44], 0.39 ± 0.10[24], and 0.35 ± 0.10[47]. This discrepancy can be attributed to the great uncertainty of $\phi_{\alpha-DC}$ and to missing minor (< 0.10)[32,33] reaction channels like the dealkylation pathway that was experimentally confirmed in flow-tube studies by Noda et al.[32] and Birdsall et al.[33].

For the OH + ethylbenzene reaction $\phi_{HO_2}^{ethylbenzene} = 0.53 \pm 0.10$ is determined. Only few experimental studies on the photo-oxidation of ethylbenzene are available in literature.[102–105] These studies focused on the formation of secondary organic aerosol and no quantitative information about gaseous oxidation products was reported. However, in previous studies the HO_2 co-products ethylphenol[49,102,105] and an epoxide species[49] were found to be oxidation products. Owing to the lack of absolute product yields, it is not possible to draw further conclusions concerning other reaction channels yielding prompt HO_2.

4.3.3 OH + xylene isomers

In the case of *o*-xylene and *p*-xylene prompt HO_2 yields of 0.41 ± 0.08 and 0.40 ± 0.09 are obtained, respectively. The yields of dimethylphenols were reported to be $0.10-0.16$[32,53,107] and $0.12-0.19$[32,45,53,59,108], respectively (see table 4.7). Again, the results suggest that non-phenol reaction pathways, e.g. epoxide formation, contribute significantly (up to 0.30) to the prompt HO_2 formation which is consistent with the current understanding of the xylene degradation mechanism. For OH + *o*-xylene the result of this study is in line with the estimation by Bloss et al.[28]: $\phi_{phenol} + \phi_{epoxide} = 0.40$. For OH + *p*-xylene the estimation is somewhat lower, i.e. 0.28.[28] To date, no absolute formation yields of epoxides from *o*- and *p*-xylene have been reported but species with corresponding molecular weights have been observed.[49,109–111]

The remainders of $1 - \phi_{HO_2}^{o-xylene} = 0.59 \pm 0.08$ and $1 - \phi_{HO_2}^{p-xylene} = 0.60 \pm 0.09$ determined here are in agreement with $\phi_{\alpha-DC} + \phi_{benzaldehyde}$ reported in several studies: $0.40-0.60$[61,99,106] for *o*-xylene and $0.40-0.70$[45,59,61,99,106,108] for *p*-xylene (see table 4.7). The uncertainties of the reported product yields leave some scope for additional minor reaction pathways like the dealkylation postulated by Noda et al.: $\phi_{dealkylation} = 0.04 - 0.05$.[32]

For *m*-xylene the situation is different because the gap between $\phi_{HO_2}^{m-xylene} = 0.27 \pm 0.06$ and ϕ_{phenol} (i.e. dimethylphenol) from previous product studies of $0.11-0.21$[32,45,48,53,107] is smaller than for *o*- and *p*-xylene (see table 4.8). Moreover, in recent studies by Zhao et al.[48] and Birdsall and Elrod[49] the

Table 4.7: Product yields of the OH-initiated oxidation of *o*- and *p*-xylene in the presence of O_2 from literature.

Reference	**Prompt HO_2**		**No prompt HO_2**		
	ϕ_{phenol} (*a*)	ϕ_{epoxide} (*b*)	$\phi_{\alpha-\text{DC}}$ (*c*)	$\phi_{\text{benzaldehyde}}$ (*d*)	$\phi_{\text{dealkylation}}$ (*e*)
OH + *o*-xylene					
Bandow et al.[106]	–	–	0.41±0.04[g]	0.05±0.01	–
Gery et al.[107]	0.10±0.04	–	–	0.17±0.07	–
Atkinson et al.[53]	0.16±0.02	–	–	0.05±0.01	–
Arey et al.[61]	–	–	0.61[g]	–	–
Noda et al.[32]	0.11±0.05	–	–	–	0.05±0.03
Nishino et al.[99]	–	–	0.46±0.06	–	–
Birdsall et al.[49]	≈ 0.08[f]	≈ 0.07[f]	–	≈ 0.09[f]	–
This study	$\phi_{HO_2} = 0.41 \pm 0.08$		$(1 - \phi_{HO_2}) = 0.59 \pm 0.08$		
OH + *p*-xylene					
Bandow et al.[106]	–	–	0.36±0.03	0.08±0.01	–
Atkinson et al.[53]	0.19±0.04	–	–	0.07±0.01	–
Smith et al.[45]	0.13±0.02	–	0.61±0.11	0.10±0.02	–
Bethel et al.[59]	0.14±0.02	–	(0.32[h])	0.07±0.01	–
Volkamer et al.[24]	–	–	0.40±0.11[i]	–	–
Volkamer et al.[108]	0.12±0.03	–	–	0.08±0.02	–
Arey et al.[61]	–	–	0.49	–	–
Noda et al.[32]	0.13±0.03	–	–	–	0.04±0.03
Nishino et al.[99]	–	–	0.58±0.05	–	–
Birdsall et al.[49]	≈ 0.12[f]	≈ 0.07[f]	–	≈ 0.09[f]	–
This study	$\phi_{HO_2} = 0.40 \pm 0.09$		$(1 - \phi_{HO_2}) = 0.60 \pm 0.09$		

[a] From *o*-xylene: (2,3+3,4)-dimethylphenol; from *p*-xylene: 2,5-dimethylphenol. [b] Sum of 2,4-dimethyl-2,3-epoxy-6-oxo-4-hexenal, 2,6-dimethyl-2,3-epoxy-6-oxo-4-hexenal, and 3,5-dimethyl-2-hydroxyl-3,4-epoxy-5-hexenal. [c] Sum of glyoxal and methylglyoxal (unless otherwise stated). [d] From *o*-xylene: 2-methylbenzaldehyde; from *p*-xylene: 4-methylbenzaldehyde. [e] Cresol. [f] Relative product yield. [g] Sum of glyoxal, methylglyoxal and dimethylglyoxal. [h] 3-hexene-2,5-dione; extrapolated to NO_x-free conditions. [i] Glyoxal.

Table 4.8: Product yields of the OH-initiated oxidation of *m*-xylene in the presence of O_2 from literature.

Reference	**Prompt HO_2**		**No prompt HO_2**		
	ϕ_{phenol} (*a*)	ϕ_{epoxide} (*b*)	$\phi_{\alpha-\text{DC}}$ (*c*)	$\phi_{\text{benzaldehyde}}$ (*d*)	$\phi_{\text{dealkylation}}$ (*e*)
OH + *m*-xylene					
Bandow et al.[106]	–	–	0.55±0.07	0.04±0.01	–
Gery et al.[107]	0.18±0.07	–	–	0.13±0.06	–
Atkinson et al.[53]	0.21±0.03[f]	–	–	0.03±0.01	–
Smith et al.[45]	0.11±0.01	–	0.48±0.02	0.05±0.01	–
Zhao et al.[48]	0.17±0.03[f]	0.02±0.01	0.15±0.04[h]	0.06±0.01	–
Arey et al.[61]	–	–	0.46	–	–
Noda et al.[32]	0.14±0.03	–	–	–	0.11±0.04
Aschmann et al.[34]	–	–	–	–	< 0.02
Nishino et al.[99]	–	–	0.63±0.09	–	–
Birdsall et al.[49]	≈ 0.05[g]	≈ 0.10[g]	–	–	–
This study	$\phi_{HO_2} = 0.27 \pm 0.06$		$(1 - \phi_{HO_2}) = 0.73 \pm 0.06$		

[a] (2,4+2,6+3,5)-dimethylphenol (unless otherwise stated).
[b] Sum of 2,4-dimethyl-2,3-epoxy-6-oxo-4-hexenal, 2,6-dimethyl-2,3-epoxy-6-oxo-4-hexenal, and 3,5-dimethyl-2-hydroxyl-3,4-epoxy-5-hexenal. [c] Sum of glyoxal and methylglyoxal (unless otherwise stated). [d] 3-methylbenzaldehyde. [e] Cresol.
[f] (2,4+2,6)-dimethylphenol. [g] Relative product yield. [h] Methylglyoxal.

formation of epoxides from *m*-xylene was reported. The combined yield of $\phi_{\text{phenol}} + \phi_{\text{epoxide}} = 0.19 \pm 0.03$[48] corresponds quite well to the prompt HO_2 yield determined in this work. Accordingly, HO_2 formation via the epoxide reaction channel is considered to be of minor importance for *m*-xylene. Most of the previous product studies on *m*-xylene reported combined formation yields of $\phi_{\alpha-\text{DC}} + \phi_{\text{benzaldehyde}}$ ranging between 0.40−0.60.[45,61,99,106] Zhao et al.[48] reported a considerably lower value of 0.21. The authors attributed this discrepancy mainly to their very low yield of methylglyoxal (0.15) obtained in a fast turbulent flow reactor. By comparing the remainder of $1 - \phi_{HO_2}^{m-\text{xylene}} =$ 0.73±0.06 to these literature values of $\phi_{\alpha-\text{DC}}+\phi_{\text{benzaldehyde}}$ it becomes obvious that the carbon balance is not closed. Taking into account the data by Bandow et al.[106], Smith et al.[45], Arey et al.[61], and Nishino et al.[99], 0.10−0.30 of the primary oxidation products not associated with prompt HO_2 are not identified so far. This gap can at least partly be closed by the dealkylation pathway yielding cresol reported by Noda et al.[32]: $\phi_{\text{dealkylation}} = 0.11 \pm 0.04$. Contradictory results were reported by Aschmann et al.[34] who determined a cresol yield of < 0.02 for *m*-xylene and suggested that the ion peaks observed

by Noda et al.[32] could correspond to the sum of cresol and methyloxepin (both resulting from dealkylation and having the same mass-to-charge-ratio). A corresponding dealkylation mechanism yielding methyloxepin following the OH + *m*-xylene reaction was postulated by Aschmann et al.[34].

4.3.4 OH + trimethylbenzene isomers

The HO_2 yields of the OH + TMB reactions are determined to be 0.31±0.06 (1,2,3-TMB), 0.37±0.09 (1,2,4-TMB), and 0.29±0.08 (1,3,5-TMB). Only a few product studies[45,49,55,56,108] have reported the formation of phenols from TMB photo-oxidation while absolute quantitative information was only given by Smith et al.[45] and Volkamer[108] with yields of $\leq$ 0.07 (see table 4.9). Formation of epoxide compounds has been observed in a flow-tube study by Birdsall and Elrod but no absolute formation yields are available.[49] Bloss et al.[28] assigned epoxide yields of 0.21 (1,2,3-TMB), 0.30 (1,2,4-TMB), and 0.14 (1,3,5-TMB) to close the carbon balance. The results of this work support the recommendations given by Bloss et al.[28] However, it can merely be concluded that non-phenol reaction channels contribute significantly to prompt HO_2 formation (< 0.30).

For the reaction channels not associated with prompt HO_2, $1 - \phi_{HO_2} =$ 0.69±0.06 (1,2,3-TMB), 0.63±0.09 (1,2,4-TMB), and 0.71±0.08 (1,3,5-TMB) are derived. These results are similar to $\phi_{\alpha-\mathrm{DC}} + \phi_{\mathrm{benzaldehyde}} = 0.40 - 0.70$ determined in previous studies[45,59,61,99,112] (lower values for $\phi_{\alpha-\mathrm{DC}}$ of 0.20 ± 0.03 (1,2,3-TMB) and 0.36 ± 0.08 (1,2,4-TMB) were determined by Nishino et al.[99] since dimethylglyoxal was not measured). A single exception is the work by Smith et al.[45] who obtained $\phi_{\alpha-\mathrm{DC}} + \phi_{\mathrm{benzaldehyde}} = 0.93 \pm 0.25$ for the OH + 1,3,5-TMB reaction. This is somewhat greater than $1 - \phi_{HO_2}^{1,3,5-\mathrm{TMB}}$ determined in this study but still in agreement within the combined errors. The dealkylation pathway may be operative for the OH + TMB reaction but is probably of minor importance (< 0.10).

4.3.5 OH + hexamethylbenzene

The OH + HMB reaction gives $\phi_{HO_2}^{HMB}$=0.32±0.08. Unfortunately, no complementary product studies on the photo-oxidation of HMB are available. Only a single flow-tube study by Berndt and Böge[113] performed at 295 K and 25 mbar in He reported the formation of hexamethyl-2,4-cyclohexadienone following the OH + HMB reaction in the presence of NO_2. Assuming a similar HMB oxidation mechanism in the presence of O_2, hexamethyl-2,4-cyclohexadienone could be the co-product of prompt HO_2, but no experimental evidence for this reaction is available so far.

Table 4.9: Product yields of the OH-initiated oxidation of the trimethylbenzene isomers in the presence of O_2 from literature.

Reference	**Prompt HO_2**		**No prompt HO_2**	
	ϕ_{phenol} (a)	ϕ_{epoxide}	$\phi_{\alpha-\text{DC}}$ (b)	$\phi_{\text{benzaldehyde}}$ (c)
OH + 1,2,3-TMB				
Bandow et al.[112]	–	–	0.70±0.02	–
Bethel et al.[59]	–	–	0.52[e]	–
Arey et al.[61]	–	–	0.59	–
Nishino et al.[99]	–	–	0.20±0.03[f]	–
Birdsall et al.[49]	≈ 0.04[d]	≈ 0.05[d]	–	–
This study	$\phi_{HO_2} = 0.31 \pm 0.06$		$(1 - \phi_{HO_2}) = 0.69 \pm 0.06$	
OH + 1,2,4-TMB				
Bandow et al.[112]	–	–	0.56±0.02	–
Smith et al.[45]	0.02±0.01	–	0.62±0.07	0.04±0.01
Bethel et al.[59]	–	–	0.41[g]	–
Arey et al.[61]	–	–	0.50	–
Nishino et al.[99]	–	–	0.36±0.08[f]	–
Birdsall et al.[49]	≈ 0.08[d]	≈ 0.06[d]	–	–
This study	$\phi_{HO_2} = 0.37 \pm 0.09$		$(1 - \phi_{HO_2}) = 0.63 \pm 0.09$	
OH + 1,3,5-TMB				
Bandow et al.[112]	–	–	0.64±0.03[h]	–
Smith et al.[45]	0.04±0.01	–	0.90±0.25[h]	0.03±0.01
Volkamer et al.[108]	0.07±0.01	–	–	0.03±0.01
Arey et al.[61]	–	–	0.60[h]	–
Nishino et al.[99]	–	–	0.58±0.05[h]	–
Birdsall et al.[49]	≈ 0.03[d]	≈ 0.04[d]	–	–
This study	$\phi_{HO_2} = 0.29 \pm 0.08$		$(1 - \phi_{HO_2}) = 0.71 \pm 0.08$	

[a] From 1,2,3-TMB: 2,3,4-trimethylphenol; from 1,2,4-TMB: (2,3,5+2,3,6+2,4,5)-trimethylphenol; from 1,3,5-TMB: 2,4,6-trimethylphenol. [b] Sum of glyoxal, methylglyoxal, and dimethylglyoxal (unless otherwise stated). [c] From 1,2,4-TMB: (2,4+3,4+2,5)-dimethylbenzaldehyde; from 1,3,5-TMB: 3,5-dimethylbenzaldehyd. [d] Relative product yield. [e] Dimethylglyoxal; extrapolated to NO_x-free conditions. [f] Sum of glyoxal and methylglyoxal. [g] Sum of dimethylglyoxal and 3-hexene-2,5-dione; extrapolated to NO_x-free conditions. [h] Methylglyoxal.

4.3.6 OH + hydroxybenzenes

The current understanding of the OH-initiated atmospheric oxidation of hydroxybenzenes is somewhat different from that of alkylbenzenes and a short overview is presented in fig. 4.5. The degradation also proceeds preferably ($\geq 90\%$) via reversible OH-addition to the aromatic ring. H-atom abstraction from substituent hydroxyl groups finally yielding nitrophenols (fig. 4.5, IX, after NO reaction) is of minor importance and H-atom abstraction from alkyl substituents is almost negligible under atmospheric conditions.[114,115] The atmospheric fate of the aromatic-OH-adduct is also governed by reactions with O_2 but to date no experimental evidence is available for the intermediate formation of organic peroxy radicals. Depending on the OH-addition site with respect to the existing hydroxyl group several pathways were proposed.[115] Dihydroxybenzenes (II) are major confirmed products most likely stemming from *ortho*-OH-addition and subsequent direct H-displacement. Other confirmed products are 1,4-benzoquinones (VI) possibly formed after *ipso*-OH-addition yielding a monocyclic peroxy radical (IV) upon reaction with O_2. After further successive reactions with NO and O_2, 1,4-benzoquinones are formed. Olariu et al.[115] found that reactions proceed preferably via *ortho*-OH-addition ($> 60\%$) whereas *ipso*-OH-addition is considered to be of minor importance ($< 10\%$). Experimental evidence for *meta*- and/or *para*-OH-addition was not reported. Accordingly, formation of prompt HO_2 is expected to be exclusively associated with *ortho*-OH-addition and formation of dihydroxybenzenes:

$$\phi_{HO_2}^{\text{hydroxybenzene}} = \phi_{\text{dihydoxybenzene}} \tag{4.16}$$

On the other hand, $1 - \phi_{HO_2}$ should match the yield of nitrophenols from the H-atom abstraction channel plus the yield of 1,4-benzoquinones formed following the proposed *ipso*-OH-addition:

$$1 - \phi_{HO_2}^{\text{hydroxybenzene}} = \phi_{\text{nitrophenol}} + \phi_{\text{quinone}} \tag{4.17}$$

The prompt HO_2 yields extracted from the OH + hydroxybenzene experiments, $\phi_{HO_2}^{\text{phenol}} = 0.89 \pm 0.29$, $\phi_{HO_2}^{o-\text{cresol}} = 0.87 \pm 0.29$ and $\phi_{HO_2}^{2,5-\text{dimethylphenol}} = 0.72 \pm 0.12$, are considerably greater compared to those from alkylbenzenes with the exception of $\phi_{HO_2}^{2,4,6-\text{trimethylphenol}} = 0.45 \pm 0.13$. The results are consistent with previous product studies reporting high dihydroxybenzene yields of 0.7-0.8[115–117] from OH + phenol and OH + *o*-cresol (see table 4.10). This confirms that HO_2 is formed as co-product of dihydoxybenzenes.

Table 4.10: Product yields of the OH-initiated oxidation of phenol and *o*-cresol in the presence of O_2 from literature.

Reference	**Prompt HO_2**	**No prompt HO_2**	
	$\phi_{\text{dihydroxybenzene}}$ (*a*)	$\phi_{\text{nitrophenol}}$ (*b*)	ϕ_{quinone} (*c*)
OH + phenol			
Olariu et al.[115]	0.80±0.12	0.06±0.01	0.04±0.01
Berndt et al.[116]	0.73±0.04	0.04±0.02	0.01±0.01
This study	$\phi_{HO_2} = 0.89 \pm 0.29$	$(1 - \phi_{HO_2}) = 0.11 \pm 0.29$	
OH + *o*-cresol			
Olariu et al.[115]	0.73±0.15	0.07±0.02	0.07±0.02
Coeur-Tourneur et al.[117]	–	0.05±0.01	0.06±0.01
This study	$\phi_{HO_2} = 0.87 \pm 0.29$	$(1 - \phi_{HO_2}) = 0.13 \pm 0.29$	

[a] From phenol: 1,2-dihydroxybenzene; from *o*-cresol: 3-methyl-1,2-dihydoxybenzene.
[b] From phenol: 2-nitrophenol; from *o*-cresol: 6-methyl-2-nitrophenol.
[c] From phenol: 1,4-benzoquinone; from *o*-cresol: methyl-1,4-benzoquinone.

The contributions of reaction channels not associated with prompt HO_2 were determined to be $1 - \phi_{HO_2}^{\text{phenol}} = 0.11 \pm 0.29$ and $1 - \phi_{HO_2}^{o-\text{cresol}} = 0.13 \pm 0.29$. Although the errors are considerable, these yields correspond well to reported values of $\phi_{\text{nitrophenol}} + \phi_{\text{quinone}}$ from phenol (0.10±0.02)[115] and *o*-cresol (0.14±0.04)[115], respectively. No product studies are available in the literature for 2,5-dimethylphenol and 2,4,6-trimethylphenol.

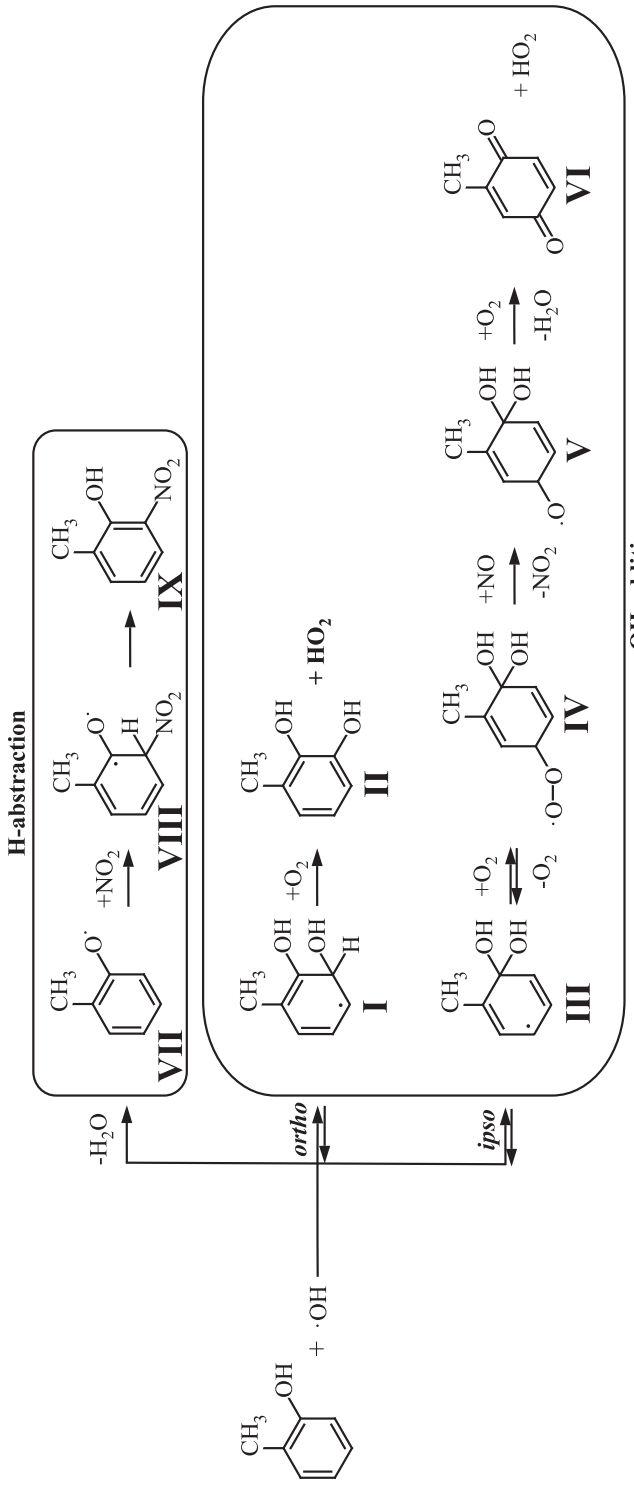

Figure 4.5: Postulated reaction pathways of the OH-initiated oxidation of *o*-cresol.[115,118–120] For convenience, different resonance structures and possible isomers are not shown. HO_2 formed without preceding NO reaction steps is indicated in bold face.

5

Outdoor atmosphere simulation chamber studies

The outdoor atmosphere simulation chamber SAPHIR (Simulation of Atmospheric PHotochemistry In a large Reaction chamber) as shown in fig. 5.1 is located on the FZJ campus (50.91 °N, 6.41 °E) and facilitates the investigation of photochemical processes under preassigned and controlled conditions without the influence of meteorological effects (cf. Karl et al.[121], Poppe et al.[122], Wegener et al.[123]). SAPHIR consists of a 270 m^3 doubled-walled cylindrical teflon foil of 18 m in length and 5 m in diameter held by a steel frame. The teflon foil (DuPont, 125−250 μm thickness) is chemically inert and transmits radiation over the whole solar spectral range reaching the earth's surface.[124,125] A shutter system allows for a rapid closure of the chamber (≈60 s). Continuous flushing of the chamber and the space between the two layers of teflon foil with highly purified synthetic air is performed at slightly elevated pressures (0.5 mbar for the inner volume, 0.3 mbar for the outer volume) to prevent contaminations by small leakages in the foil. SAPHIR is equipped with a comprehensive set of analytical instruments that are either sampling air from the chamber through teflon tubings or are measuring in situ. The instruments are installed in air-conditioned containers below the chamber. Table 5.1 gives an overview of the typical instrumentation during the campaigns dedicated to the investigation of aromatic hydrocarbon photo-oxidation.

An enormous number of intermediates is involved in the oxidation of aromatics. However, only a selection of key species can be quantified. The focus of this study is therefore the investigation of radical budgets and the formation of some primary oxidation products. Further, an evaluation of the aromatic hydrocarbon chemistry in the MCMv3.2 is attempted. Because of their atmospheric abundance in urban environments, benzene, toluene,

Figure 5.1: The outdoor atmosphere simulation chamber SAPHIR with opened shutter system.

p-xylene, and 1,3,5-TMB are chosen for the investigations. Within this homologous series trends can be studied, e.g. the increasing importance of ring fragmentation with the number of alkyl substituents.[44,45] For the xylenes and trimethylbenzenes, isomers with the highest structural symmetry are selected to reduce the number of possible degradation products. Again CO is chosen as a chemical reference system because the rate constant of the OH + CO reaction is well-known and the OH radical recycling in the presence of NO only proceeds via reaction R7 and does not involve organic peroxy radicals. Thus, the photo-oxidation of CO offers the possibility to investigate chamber-related effects and their impact on the HO_x and NO_x budgets. Table 5.2 provides an overview of SAPHIR experiments with CO and aromatics performed in 2010 and 2011.

Table 5.1: Typical equipment of SAPHIR with analytical instruments during campaigns in 2010 and 2011. The reader is referred to literature for detailed information on the individual measurement techniques.

Experimental observable	Measurement method	Instrument	Time resolution / s
VOCs	Proton transfer reaction mass spectrometry (PTR-MS)[126]	Ionicon Analytik	30
VOCs	Gas chromatography (GC)[123]	Chrompack VOC Air	1500
HCHO	Hantzsch reaction[127]	AERO Laser AL4001	150
HNO_2	Long path absorption photometry (LOPAP)[128]	QUMA Elektronik & Analytik	300
CO	Reduction gas analysis (RGA)[123]	Trace Analytical RGA-3	180
CO_2, CH_4, H_2O	Cavity ring-down spectroscopy (CRDS)[129]	Picarro G2301	60
NO_x, O_3	Chemiluminescence (CL)[130]	Eco Physics TR 780	90
PAN	Gas chromatography (GC)[131]	Jülich PAN-GC	600
Glyoxal, HNO_2, NO_2	Incoherent broadband cavity-enhanced absorption spectroscopy (IBBCEAS)[132]	Jülich IBBCEAS instrument	60
OH, HCHO	Differential optical absorption spectroscopy (DOAS)[133]	Jülich DOAS instrument	200
OH, HO_2, RO_2	Laser-induced fluorescence (LIF)[89,134]	Jülich RO_x-LIF system	50
k_{OH}	Flash photolysis/laser-induced fluorescence (FP/LIF)[73]	Jülich RO_x-LIF system	180
Aerosol size distribution	Scanning mobility particle sizer (SMPS)[135]	TSI 3080	400
Aerosol number concentration	Condensed particle counter (CPC)	TSI UWCPC3786	20
Aerosol composition	Aerosol mass spectrometer (AMS)[136]	Aerodyne Research	300
Photolysis frequencies*	Spectroradiometry (SR)[124]	Bentham 300	120
Temperature	Ultrasonic anemometer (USA)	Metek USA-1	60
Pressure	Pressure gauge	Setra Systems 270	60
Flow rate	Mass flow controller	Brooks	60

* J_{NO_2}, J_{HNO_2}, J_{HCHO}, $J_{O(^1D)}$, $J_{H_2O_2}$; see section 5.2 for details.

Table 5.2: Compilation of SAPHIR experiments. Listed concentrations are measured immediately after injection of trace gases and used as initial conditions in MCMv3.2 model simulations. a_{HNO_2} and a_{HCHO} are determined by matching the initial increase of HNO_2 and HCHO measured by LOPAP and Hantzsch, respectively, during zero air periods. k_{OH}^{BG} is observed by the OH reactivity instrument in the dark, humidified chamber prior to addition of reactive trace gases (refer to section 5.3.1 for more detailed information).

Exp.	Date	Note	Reactant	[Reactant][a] / ppb	[Reactant][b] / ppb	[Reactant][c] / ppb	[NO][b] / ppb	a_{HNO_2} / 10^{13}cm^{-3}	a_{HCHO} / 10^{13}cm^{-3}	k_{OH}^{BG} / s^{-1}
1	17.06.2011	*d, e*	CO	–	1550	1550	–	3.8	0.8	1.2
2	09.08.2011	*e*	CO	–	860	860	–	2.9	0.4	1.2
3	07.06.2010	*f*	Benzene	280	230	230	–	7.1	0.3	1.5
4	23.06.2010	*d*	Benzene	280	–	235	–	4.2	0.3	1.0
5	01.08.2011		Benzene	235	226	250	–	2.8	0.6	0.9
6	08.06.2010	*f*	Benzene	290	235	235	8	7.1	0.3	1.0
7	25.06.2010	*d*	Benzene	280	–	215	8	4.2	0.3	1.0
8	05.07.2010	*d, f*	Toluene	85	–	65	–	3.5	0.3	1.0
9	04.08.2011		Toluene	85	73	107	–	2.8	0.2	0.9
10	13.06.2010		Toluene	85	54	60	7.5	4.0	0.3	2.0
11	14.06.2010		*p*-Xylene	30	17	26	–	4.7	0.3	1.5
12	02.07.2010	*d*	*p*-Xylene	30	–	26	–	3.3	0.3	1.5
13	07.08.2011		*p*-Xylene	30	22	29	–	2.8	0.5	1.5
14	16.06.2010		*p*-Xylene	30	17	24	7.5	5.2	0.3	2.5
15	30.06.2010	*d, f*	*p*-Xylene	30	–	24	8	4.7	0.3	1.5
16	17.06.2010		1,3,5-TMB	6.5	3.4	6.0	–	5.2	0.3	2.0
17	01.07.2010	*d, f*	1,3,5-TMB	6.5	–	6.5	–	3.5	0.3	1.0
18	10.08.2011		1,3,5-TMB	6.5	4.6	7.2	–	2.8	0.5	0.5
19	21.06.2010		1,3,5-TMB	6.5	3.0	6.0	7.5	4.2	0.3	1.3
20	28.06.2010	*d, g*	1,3,5-TMB	6.5	–	6.5	8	4.2	0.3	1.0

[a] Amount injected after zero air period using a microliter syringe; concentration calculated from the injected liquid volume.
[b] CO measured by RGA, aromatics by PTR-MS, and NO by CL. [c] Concentration calculated from the initial increase of k_{OH} upon addition of reactive trace gases (using OH rate constants from MCMv3.2).
[d] No PTR-MS measurements available. [e] No zero air period. O_3 and/or CO injected into the dark chamber.
[f] No LOPAP measurements available. a_{HNO_2} determined by matching the increase of [NO] and [OH] during zero air period.
[g] No Hantzsch measurements available. a_{HCHO} estimated.

5.1 Experimental procedure

The sequence of a typical SAPHIR experiment is shown in fig. 5.2 for the photo-oxidation of CO performed on 09.08.2011. Experiments start after the chamber is flushed overnight with high purity dry synthetic air provided by a gas mixing system at large flow rates of up to 300 m^3h^{-1} to purge all contaminations below the detection limits of the instruments. A fan driven by a pneumatic motor is used to assure homogeneous mixing under all conditions resulting in a mixing time of about 120 s.[125] In the morning, the flushed chamber is humidified by premixing ultrapure water vapour (Milli-Q) from a vaporizer to the main gas flow. Typical relative humidities of 40% are achieved. After humidification, the chamber is operated at a flow rate of about 5−10 m^3h^{-1} that is needed to replenish the losses caused by air sampling of instruments and leakages. This replenishment flow results in a dilution of all trace gases in the chamber. Prior to the photo-oxidation experiments, CO_2 is added as chemically inert tracer for the dilution rate. Afterwards, the shutter system is opened and the chamber is exposed to sunlight. Typically, no other trace gases are added for a period of about two hours. During this zero air period, HNO_2 is formed photolytically at the chamber walls dependent on the presence of water and UV radiation[137] (see section 5.2 for details). Photolysis of HNO_2 is the major primary source of OH radicals in SAPHIR and therefore the OH concentration measured by LIF and/or differential optical absorption spectroscopy (DOAS) is found to increase after the shutter system of the chamber is opened. Subsequently, the compound of interest (CO or aromatic hydrocarbon) is injected into the chamber (photo-oxidation period). Gases are introduced into the chamber using calibrated mass flow controllers. Liquids are injected by microliter syringes via a heated injection port which is continuously flushed with dry N_2. The N_2 flow from the injection port is added to the main replenishment flow of the chamber.

The example in fig. 5.2 shows three additions of CO that are observed by reduction gas analysis (RGA) and by the OH reactivity instrument. The resulting concentration of OH radicals in SAPHIR depends on the concentrations of OH reactants and is further modulated by solar radiation. A sharp decrease of the OH concentration upon the first addition of CO and a diurnal variation due to intermittent shading of SAPHIR by clouds can be seen in fig. 5.2. After several hours of illumination (depending on the respective compound injected) the shutter system is closed and the chamber is prepared for the next experiment.

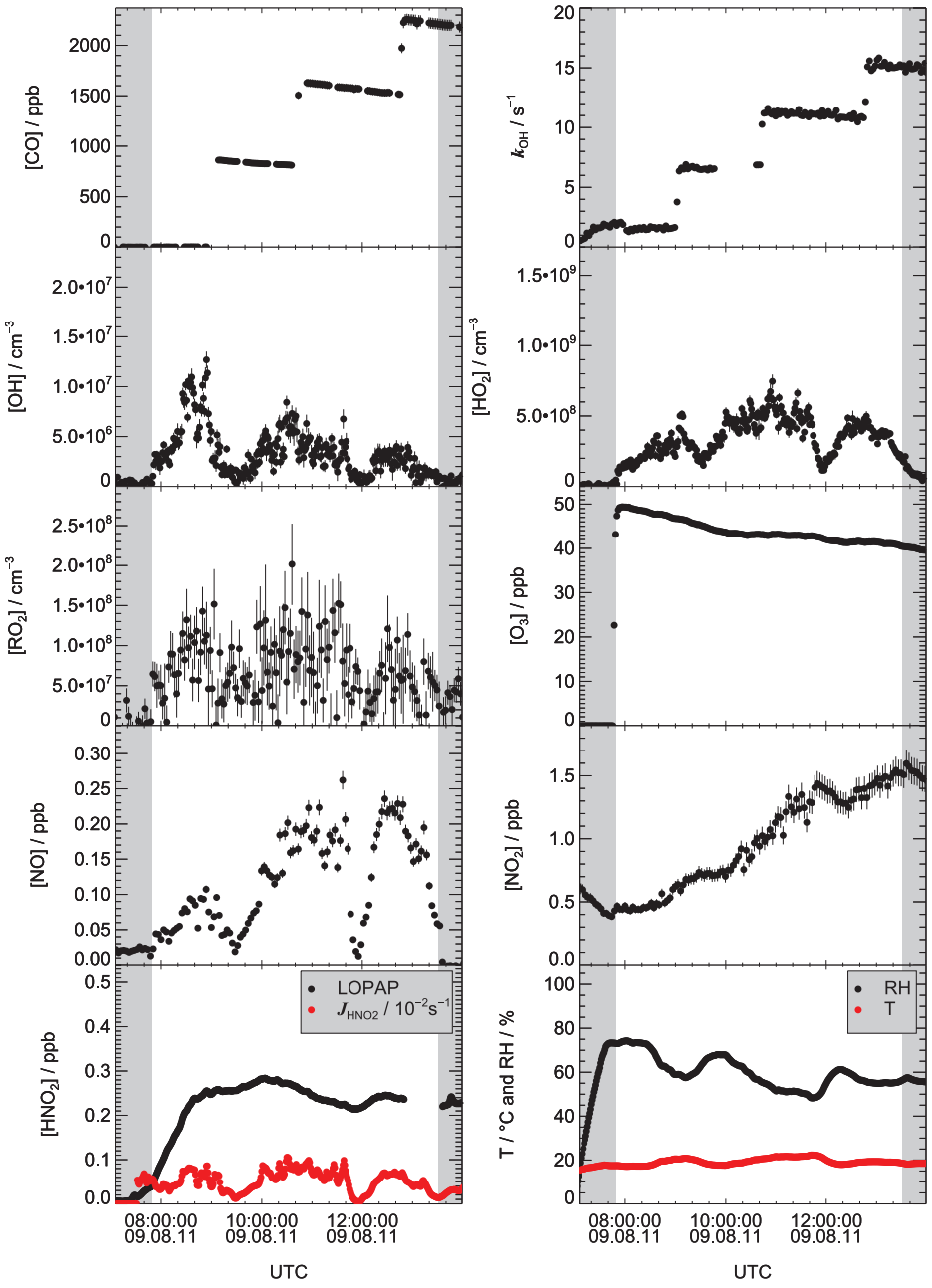

Figure 5.2: Measurements of selected quantities performed during an experiment with CO on 09.08.2011. Three injections of CO are observed by RGA and the OH reactivity instrument. OH rapidly decreases after the first CO injection. Further, the diurnal profiles of OH, HO_2, RO_2, and NO are modulated by solar radiation and correlate with J_{HNO_2} (red symbols in lower left panel). Grey shaded areas indicate periods when the chamber shutter system is closed. The time axis is given in Universal Time Coordinated (UTC).

Photo-oxidation experiments with aromatics are performed under low NO_x (<2 ppb) and high NO_x (up to 10 ppb) conditions. In the case of high NO_x experiments, NO is injected 30 minutes prior to the addition of the aromatic. For low NO_x experiments no injections were made and the main source of NO_x was photolysis of HNO_2.

5.2 Numerical model simulations

A photochemical zero-dimensional box model is used for the interpretation of SAPHIR experiments. The model incorporates explicit photo-oxidation schemes of aromatic hydrocarbons and an inorganic reaction scheme taken from the MCMv3.2[23,28] (via website: http://mcm.leeds.ac.uk/MCM). The set of differential equations is solved numerically using the FACSIMILE solver (AEA Technologies) in combination with the EASY interface (Brauers and Rohrer[138]). All experimental time-dependent boundary conditions (temperature, pressure, replenishment flow rate, relative humidity, photolysis frequencies) are considered in the model. Photolysis processes (e.g. R1 and R18) are quantified by first-order rate constants termed as photolysis frequencies J. MCMv3.2 provides parameterizations of photolysis frequencies[22] valid for clear sky conditions (J^{CS}) that need to be adjusted to represent the photolytic conditions within SAPHIR (shading by construction elements, light attenuation by the teflon foil, backscattering from the chamber floor, and external effects caused by clouds and aerosols). A model was developed by Bohn and Zilken[124] to calculate photolysis frequencies J in the chamber based on external measurements[125] of solar spectral actinic flux. Photolysis frequencies of NO_2, HNO_2, HCHO, $O(^1D)$, and H_2O_2 are provided routinely. If no measurements are available (e.g. photolysis frequencies of unsaturated γ-dicarbonyls, ketones, organic hydroperoxides, etc.) the ratio of measured J_{NO_2} to parameterized $J^{CS}_{NO_2}$ is applied as scaling factor for the photolysis frequencies taken from MCMv3.2.

Correction of HO_2 measurement interferences by RO_2

The cycles of HO_x and NO_x in photo-oxidation systems are coupled via reactions R7, R8, R15, R16, and R17. This shows that accurate measurements of all involved species are essential if model-measurement comparisons are consulted for analysis. The Jülich RO_x-LIF instrument facilitates measurements of OH, HO_x, and RO_x (sum of OH, HO_2, and RO_2). From these measurements, concentrations of HO_2 and RO_2 can be determined (see Fuchs et al.[89] for details). As outlined in sections 4.1 and 4.2, the LIF HO_2 detection

technique is subject to interferences caused by specific organic peroxy radicals[79,81] and a significant amount of RO_2 is unintentionally converted to HO_2 in the LIF detection cell. In the case of RO_2 stemming from benzene, relative detection sensitivities for RO_2 compared to that for HO_2 of $\alpha_{RO_2}^{benzene} = 0.86$ were determined experimentally in 2010.[81] In 2011, $\alpha_{RO_2}^{benzene}$ was then reduced to 0.17 by means of technical changes of the experimental setup.[81]

Generally, the HO_2 concentration measured by LIF during SAPHIR experiments, $[HO_2^*]$, has to be corrected for the concentration of a number of interfering RO_2 radicals, $[RO_2]_i$, detected with the corresponding relative sensitivities $\alpha_{RO_2}^i$ to obtain the true HO_2 concentration, $[HO_2]$.[82]

$$[HO_2] = [HO_2^*] - \sum \left(\alpha_{RO_2}^i \times [RO_2]_i \right) \tag{5.1}$$

Accordingly, the true RO_2 concentration, $[RO_2]$, is given by the sum of the RO_2 concentration measured by LIF, $[RO_2^*]$, plus the contribution of a number of RO_2 radicals, $\alpha_{RO_2}^i \times [RO_2]_i$, that was spuriously detected as HO_2.

$$[RO_2] = [RO_2^*] + \sum \left(\alpha_{RO_2}^i \times [RO_2]_i \right) \tag{5.2}$$

For the correction of the LIF data and for model-measurement comparisons, it is assumed that only RO_2 are detectable by LIF that are converted within one NO reaction step forming RO (R8) and one subsequent O_2 reaction step forming HO_2 (R10). Speciated RO_2 measurements are not available and consequently, the correction of the LIF data is necessarily done on the basis of numerical model simulations incorporating MCMv3.2. Individual organic peroxy radical concentrations, $[RO_2]_i$, are simulated for each SAPHIR experiment. Organic peroxy radicals involved in the photo-oxidation of aromatics that are detectable by LIF are listed in the appendix A. Speciated values of $\alpha_{RO_2}^i$ are not available and $\alpha_{RO_2}^{benzene}$ is therefore used for corrections according to eqs. 5.1 and 5.2 for all $[RO_2]_i$ stemming from benzene, toluene, *p*-xylene, and 1,3,5-TMB. Additional MCMv3.2 based factors c_{RO}^i and $c_{HO_2}^i$ account for the yield of RO in reaction R8 and the yield of HO_2 in reaction R10, respectively, and are applied to $\alpha_{RO_2}^i$ (see appendix A for details). All HO_2 and RO_2 measurements presented in the following sections are corrected for interferences. At least for the experiments in 2011, the uncertainties of these corrections are small.

5.3 Results

Up-to-date explicit photo-oxidation mechanisms of MCMv3.2 are evaluated against the experimental data. Model-measurement comparisons are used

to study SAPHIR specific processes (section 5.3.1) and further to investigate aromatic degradation mechanisms (section 5.3.2). For the evaluation of MCMv3.2 against SAPHIR experiments with aromatics, the model runs are exclusively constrained to experimental boundary conditions and all concentrations of reactive trace gases involved in aromatic photo-oxidation systems are treated as free parameters rather than prescribing any measured data. For example, constraining the model to measured trace gas concentrations with small experimental errors might be related to substantial uncertainties of chemical turnover rates simulated by the model if implemented rate constants are subject to large errors. To identify key parameters influencing the photo-oxidation systems, sensitivity studies are performed by individually varying selected model parameters. These sensitivity studies give insight into HO_x and NO_x budgets and their dependence on the specific key parameters. In addition, primary phenolic oxidation product yields are determined in section 5.3.3. These product yields contain information on the branching ratios of major oxidation pathways. Moreover, the unique combination of instruments operated during SAPHIR experiments with aromatics allows for a detailed analysis of the OH budget that is performed on the basis of measurements alone, as described in section 5.3.4.

5.3.1 Chamber auxiliary mechanism

An important issue of simulation chamber experiments is the influence of wall effects that has to be considered in the data analysis.[137,139–141] Numerical simulations presented here include an auxiliary model accounting for chamber-related effects that can be subdivided into chamber sources and chamber sinks. The dominant radical source in SAPHIR is the photolysis of HNO_2 yielding OH and NO. HNO_2 is formed photolytically in the presence of water vapour probably at the inner wall of the chamber. The photolytic HNO_2 source strongly depends on relative humidity RH, light intensity (using the NO_2 photolysis frequency J_{NO_2} as proxy) and temperature T. An empirical parameterization for the HNO_2 production rate (in units of $cm^{-3}s^{-1}$) is given by Rohrer et al.[137]:

$$\begin{aligned} S_{HNO_2} &= a_{HNO_2} \times J_{NO_2} \\ &\times \left(1 + \left(\frac{RH}{11.6\%}\right)^2\right) \times \exp\left(-\frac{3950\ \mathrm{K}}{T}\right) \end{aligned} \tag{5.3}$$

A typical scaling factor of $a_{HNO_2} = (4.1 \pm 1.2) \times 10^{13} cm^{-3}$ (mean value and standard deviation of results listed in table 5.2) is found for the experiments performed in 2010 and 2011. This factor is adjusted for each experiment

by matching the initial increase of HNO_2 measured by long path absorption photometry (LOPAP) after the clean, humidified chamber is exposed to sunlight. In addition, Karl[139] and Richter[140] reported a chamber source of HCHO that was also found to depend on RH, J_{NO_2}, and T.

$$\begin{aligned} S_{HCHO} &= a_{HCHO} \times J_{NO_2} \\ &\times \left(0.21 + 2.6 \times 10^{-2} \times \frac{RH}{\%}\right) \times \exp\left(-\frac{2880\ \mathrm{K}}{T}\right) \end{aligned} \tag{5.4}$$

For the evaluation of experiments presented here, a typical scaling factor of $a_{HCHO} = (0.4 \pm 0.3) \times 10^{13} \mathrm{cm}^{-3}$ (mean value and standard deviation of results listed in table 5.2) is applied to reproduce the HCHO concentrations measured by the Hantzsch and/or the DOAS instrument during zero air periods. Recently, other minor chamber sources of organic substances were reported.[141] Among them, formation of acetaldehyde and acetone are the most prominent sources. However, no systematic investigation was done to derive similar empirical expressions like those for HNO_2 and HCHO. If available, acetaldehyde and acetone concentrations measured by PTR-MS are used as constraints in the model simulations to account for these chamber sources. This approach is justified because these substances are present in low concentrations and are not formed as photo-oxidation products of the aromatics investigated in this work.

A careful characterization of SAPHIR specific processes is the precondition for the analysis of photo-oxidation experiments with aromatics by means of model-measurement comparisons. CO, which represents one of the most simple substances regarding its photochemical degradation, is therefore used for characterization experiments. The impact of chamber specific effects is assessed on the basis of the inorganic MCMv3.2 reaction scheme with reference to the CO photo-oxidation experiment performed on 09.08.2011. As shown in fig. 5.3, traces of NO_2 (about 0.7 ppb; for characterization of the IBBCEAS instrument) were added into the dark chamber. Upon humidification, the NO_2 concentration dropped again to 0.4 ppb. Afterwards, approximately 50 ppb of O_3 were added and the chamber volume was exposed to sunlight followed by the typical formation of HNO_2. Photolysis of HNO_2 led to formation of OH and NO. After the zero air period, three injections of CO were done. The increase of k_{OH} after each injection corresponds well to the measured CO concentration (using the MCMv3.2 recommendation for the OH + CO rate constant[92]). However, the measurements of k_{OH} prior to the first CO addition exceed the expected values (see red line in the upper right panel of fig. 5.3). Apparently, OH reactants were unintentionally injected into the dark chamber during the humidification. When water vapour

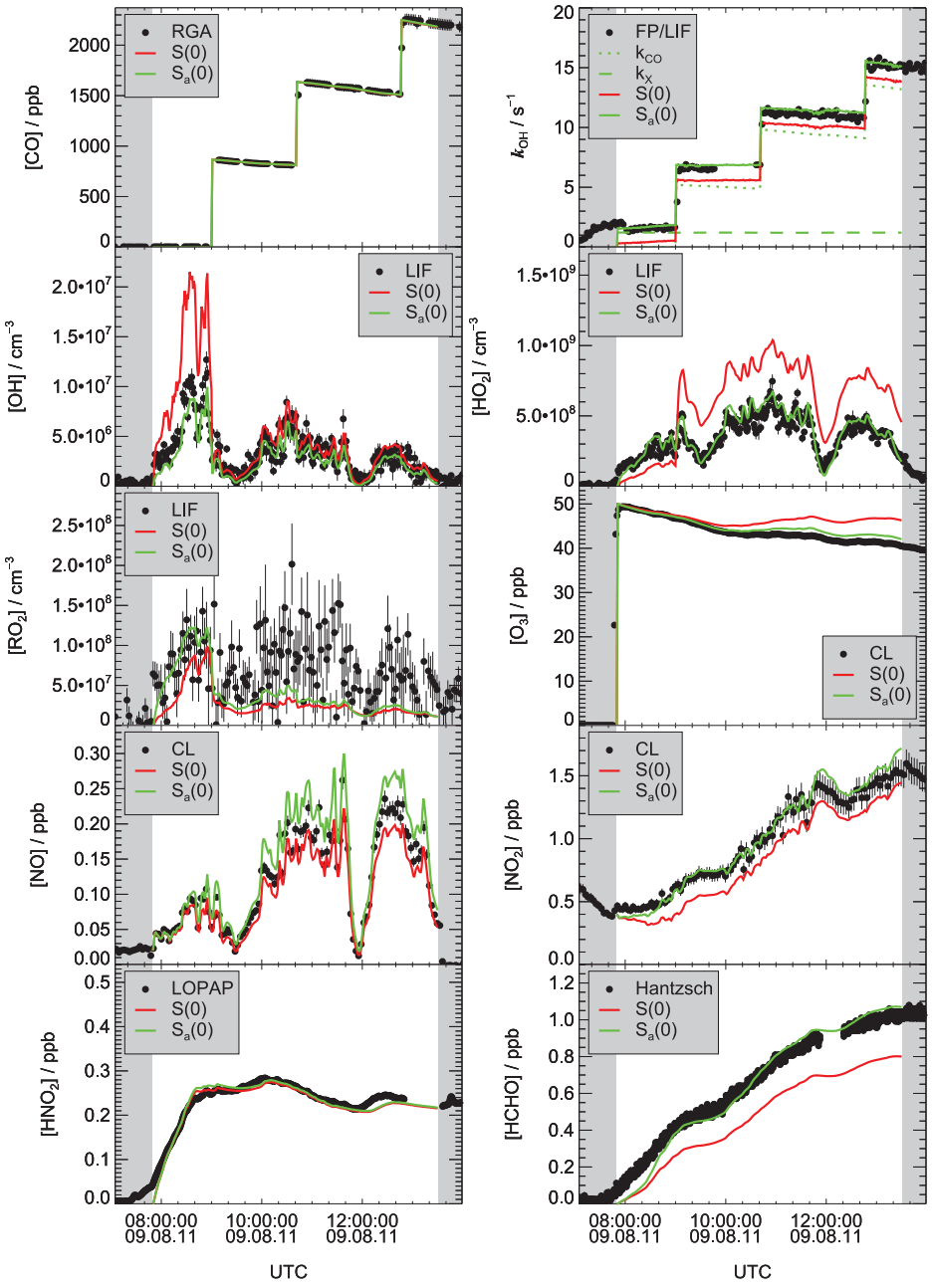

Figure 5.3: Model-measurement comparisons for a SAPHIR reference experiment with CO performed on 09.08.2011. Black symbols represent measurements. Solid lines show MCMv3.2 model simulations with ($S_a(0)$, green) and without (S(0), red) auxiliary chamber mechanism. The short dashed green line depicts the contribution of the OH + CO reaction to k_{OH} whereas the long dashed green line denotes the contribution of k_{OH}^{BG} to k_{OH}.

was injected, k_{OH} always exhibited a slight increase although no VOCs were detected. Consequently, the simulated profile of k_{OH} initially underpredicts the measurements by about 1.5 s^{-1}. However, the same difference is observed throughout the whole day. This hints at a constant background consumption of OH radicals in the chamber. Indeed, OH background loss rate constants of $k_{OH}^{BG} \approx 1.5\ s^{-1}$ are observed for all SAPHIR experiments in the clean, humidified, and dark chamber although measured VOCs are below their detection limits. Only part of this background reactivity ($\approx 30\%$) can be explained by reactions of OH with HNO_2, HCHO, acetaldehyde, acetone, and NO_x so that model simulations overpredict the measured OH concentration during zero air periods. In addition, typical concentrations of about $2 \times 10^8 cm^{-3}$ of HO_2 and unidentified RO_2 are observed in zero air. These peroxy radical concentrations are significantly greater than those predicted for the photo-oxidation of HNO_2, HCHO, acetaldehyde, and acetone. Consequently, part of k_{OH}^{BG}, HO_2, and RO_2 result from other unknown OH reactants in the chamber. In previous studies, this unknown background reactivity was assigned to a conversion of OH to HO_2 involving a hypothetical reactant Y (e.g. Rohrer et al.[137]). This approach was consistent with the formation of O_3 observed during zero air periods. In this work, simultaneous measurements of OH, HO_2, RO_2, and k_{OH} reveal that an auxiliary background reactivity of $OH + Y \longrightarrow HO_2$ results in an overestimation of HO_2 concentrations. Consequently, a new concept is introduced here. It involves an auxiliary reaction of OH plus an unknown compound X forming methylperoxy radicals (CH_3O_2) and HO_2 with yields of $\phi_{CH_3O_2}$ and $(1 - \phi_{CH_3O_2})$, respectively.

$$OH + X \longrightarrow \phi_{CH_3O_2}\ CH_3O_2 + (1 - \phi_{CH_3O_2})\ HO_2 \qquad \text{(R20)}$$

Reaction R20 is used to reproduce the initial formation of peroxy radicals during zero air periods. X is assumed to exhibit no diurnal variation. This is consistent with observations during zero air periods where no substantial increase of k_{OH} is measured. Accordingly, k_{OH}^{BG} caused by the unknown reactant X is treated as a constant contribution to the observed OH reactivity.

The model-measurement comparisons are evaluated quantitatively by calculating the summed squared residuals $\chi^2_{S(i)}$ for each individual model scenario S(i) (e.g. green lines in fig. 5.3) normalized to $\chi^2_{S(0)}$ for the MCMv3.2 base case scenario S(0) (red lines in fig. 5.3). By introducing reaction R20 to account for the observed OH background reactivity, the simulated peroxy radical concentrations expectedly increase compared to the scenario S(0). This effect is desired for RO_2 because S(0) underpredicts organic peroxy radicals. For HO_2 the approach deteriorates the agreement between model and measurement because HO_2 is already overestimated by scenario S(0) (see

fig. 5.3). A compromise for these compensating effects is attempted by optimising the simulation for RO_2 adapting $\phi_{CH_3O_2}$ and further introducing an effective HO_x loss (possibly wall loss) by means of a HO_2 background loss rate constant $k_L(HO_2)$.

$$HO_2 \xrightarrow{k_L(HO_2)} \text{products} \tag{R21}$$

In a first approach, reaction R20 is introduced and the summed squared residuals for model-measurement comparisons are minimized by varying $\phi_{CH_3O_2}$. Fig. 5.4 (panel a) shows results of sensitivity studies for the target species RO_2. R_{RO_2} denotes the ratio of $\chi^2_{S(i)}$ for different values of $\phi_{CH_3O_2}$ normalized to a reference case where $\phi_{CH_3O_2}$ is set to zero and only HO_2 is produced via reaction R20. A minimum for R_{RO_2} is found at around $\phi_{CH_3O_2} \approx 0.2$.

In a next step, the unimolecular HO_2 background loss reaction R21 is implemented as additional auxiliary process to improve the ability of the model in describing the formation of peroxy radicals. $k_L(HO_2)$ is varied and the improvement of model-measurement comparisons is evaluated by means of R_{HO_2}. Here the reference case assumes $k_L(HO_2) = 0$ and also considers reaction R20. As shown in fig. 5.4 (panel b), a minimum is found for values of $k_L(HO_2)$ in the range of $(5 - 10) \times 10^{-3} s^{-1}$.

By using the auxiliary reactions R20 and R21, the model simulations for k_{OH}, OH, HO_2, and NO_x are already in good agreement with the observations. The unidentified RO_2 measured by LIF is slightly underestimated by this auxiliary chamber model. Moreover, the formation of O_3 is overestimated by numerical model simulations. In addition to the effective HO_x loss that is introduced to describe the radical formation during zero air periods, an unimolecular background loss rate constant for O_3 ($k_L(O_3)$) is required to reproduce ozone formation during SAPHIR experiments with CO.

$$O_3 \xrightarrow{k_L(O_3)} \text{products} \tag{R22}$$

In a similar procedure as outlined above, reaction R22 is introduced as a further auxiliary reaction and the value for $k_L(O_3)$ is varied to optimize the simulation of the observed O_3 concentration using the normalized summed squared residuals R_{O_3} as criterion. Here the reference case considers both R20 and R21. For values of $k_L(O_3)$ at around $10 \times 10^{-6} s^{-1}$ model simulations show the best agreement with measurements (see fig. 5.4, panel c).

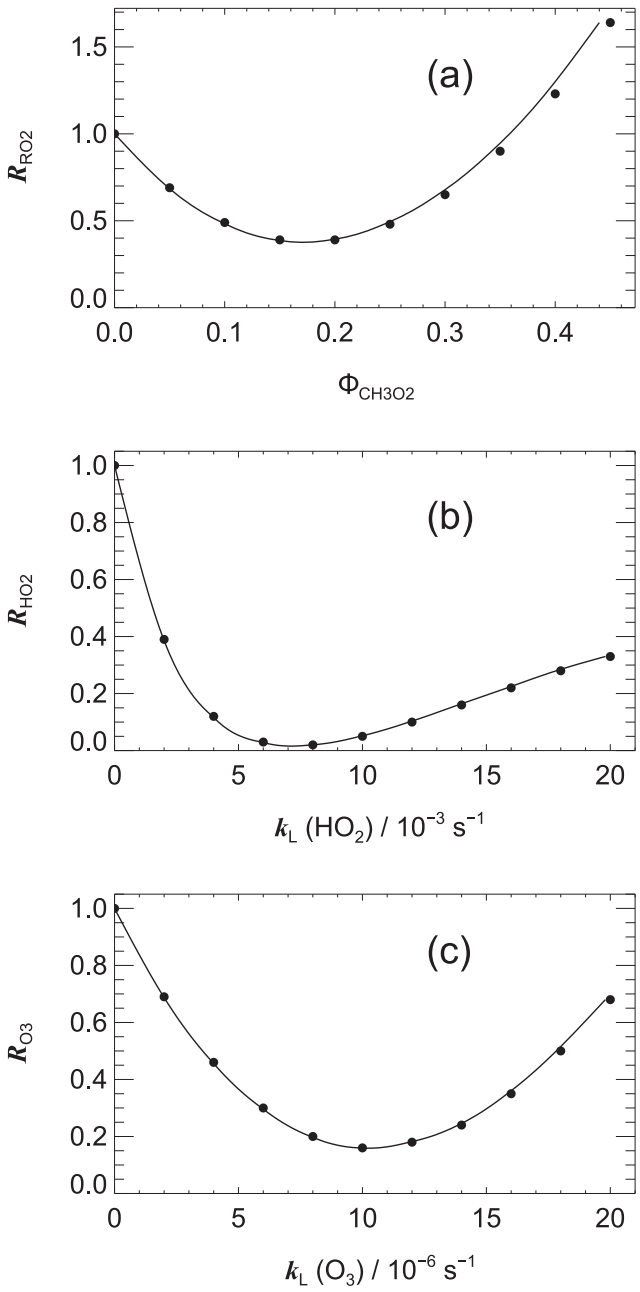

Figure 5.4: Results of model-measurement comparisons for the CO photo-oxidation experiment performed on 09.08.2011. The normalized summed squared residuals R_{RO_2}, R_{HO_2}, and R_{O_3} are consulted as measure for the performance of different model scenarios (see text). Model-measurement comparisons are restricted to the time period of illumination.

Green lines in fig. 5.3 represent the results of numerical simulations incorporating the auxiliary reactions R20, R21, and R22. It becomes obvious that the agreement for RO_2 is not perfect and other sources of organic peroxy radicals, possibly from photolytical processes, cannot be excluded. To clarify this point, more experiments dedicated to the investigation of chamber dependent effects are required. The SAPHIR auxiliary mechanism outlined in this section was tested for two CO photo-oxidation experiments (as listed in table 5.2) and for each zero air period performed prior to experiments with aromatic hydrocarbons. Typical values of $\phi_{CH_3O_2} = 0.2$, $k_L(HO_2) = 6 \times 10^{-3} s^{-1}$, and $k_L(O_3) = 8 \times 10^{-6} s^{-1}$ are used for the analysis of all SAPHIR experiments. The influence of the chamber auxiliary mechanism during photo-oxidation experiments with aromatics is limited and is discussed in section 5.4.2.

5.3.2 Evaluation of aromatic photo-oxidation mechanisms

Typical results of model-measurement comparisons are shown in fig. 5.5 for a photo-oxidation experiment with 1,3,5-TMB performed on 10.08.2011 under low NO_x conditions. Red lines represent MCMv3.2 base case simulations incorporating the chamber auxiliary mechanism (scenario $S_a(0)$), black and yellow symbols depict measurements. Again a zero air period is observed where the OH radical concentration increases strongly due to photolysis of HNO_2 that is formed photolytically at the chamber walls. OH rapidly decreases after injection of 1,3,5-TMB whereas HO_2 and RO_2 concentrations rise. SAPHIR experiments performed in 2010 and 2011 reveal that MCM tends to underestimate OH and peroxy radical concentrations in almost all experiments. The OH reactivity and the O_3 concentration are overpredicted by MCMv3.2. The SOA formation from aromatics was also investigated, but the analysis of these data is beyond the scope of this work and is presented elsewhere.[142,143] Briefly, SOA yields, given by the aerosol mass formed divided by the chemical turnover of the parent aromatic, were found to be less than 8%[142] for the experiments listed in table 5.2 which is in line with aromatic SOA yields reported in literature.[144–146] Therefore, the loss of gaseous compounds due to condensation onto particulate matter is of minor importance during SAPHIR experiments and is neglected in the evaluation of the gas phase chemistry.

Sensitivity studies are performed to identify the reasons for the MCMv3.2 deficiencies. These sensitivity studies focus on the fate of the bicyclic peroxy radical $biRO_2$ (e.g. see fig. 2.2) which is the major primary oxidation product

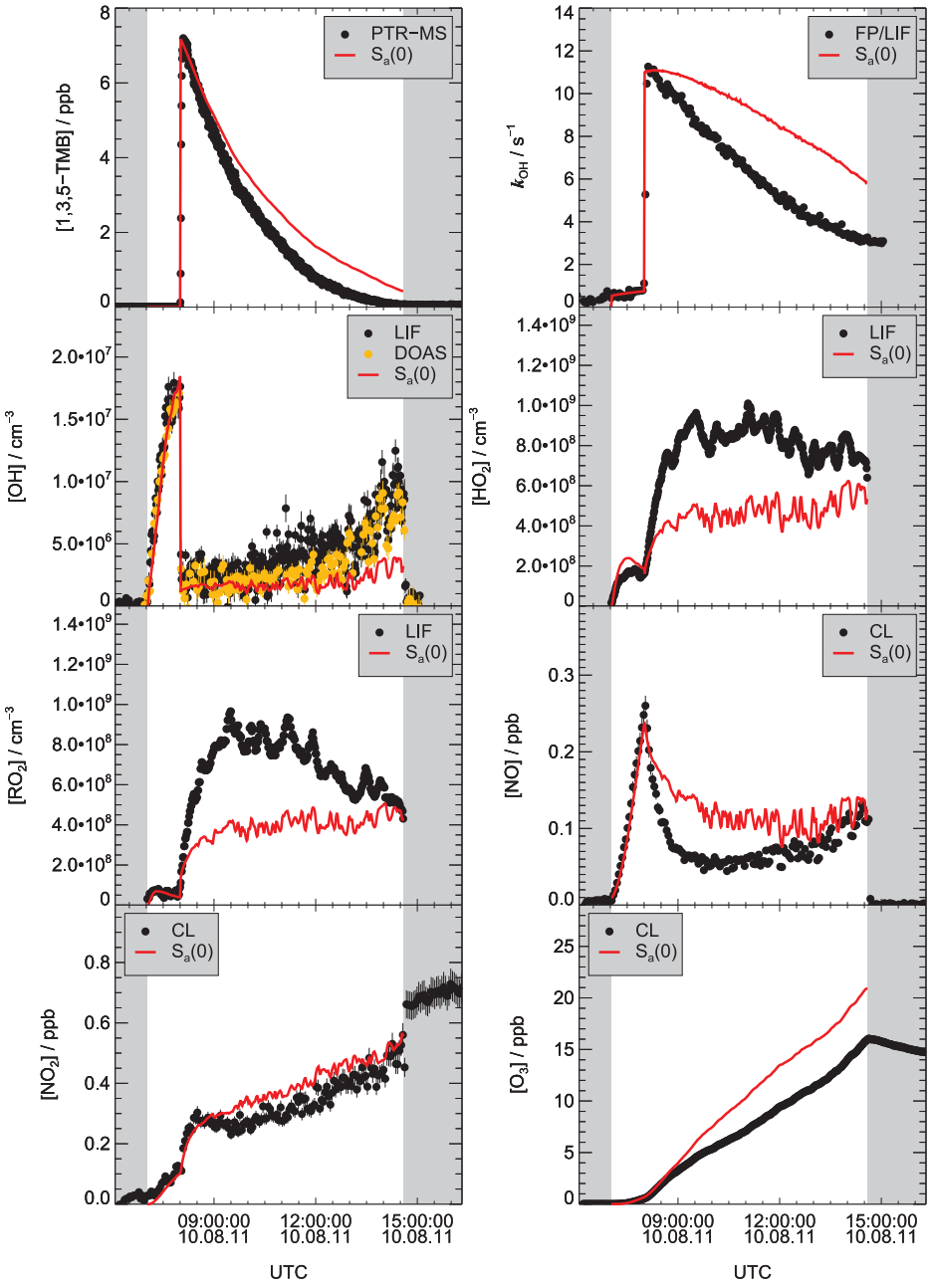

Figure 5.5: Model-measurement comparisons for a SAPHIR experiment with 1,3,5-TMB performed on 10.08.2011. Black and yellow symbols represent measurements. Red lines show MCMv3.2 model simulations for the base case scenario $S_a(0)$. The concentration of 1,3,5-TMB measured by PTR-MS is scaled to match the initial increase of k_{OH} (see section 5.3.3 for details).

from toluene, *p*-xylene, and 1,3,5-TMB with yields of about 65%, 63%, and 79%, respectively. For benzene this yield is somewhat lower ($\approx 35\%$) but still a significant fraction of the reaction proceeds via the $biRO_2$ pathway. Potential shortcomings in the MCMv3.2 representation of the subsequent chemistry of $biRO_2$ are therefore expected to affect model-measurement comparisons for all aromatics. As outlined in section 2.2, $biRO_2$ is predominantly consumed by reactions with NO either yielding a bicyclic nitrate ($biRNO_3$) or a bicyclic alkoxy radical (biRO). Bicyclic nitrate yields (ϕ_{biRNO_3}) implemented in MCMv3.2 were assigned on the basis of experimental data for alkane peroxy radicals and range around $8-16\%$.[147,148] However, it was recently found in a flow-tube study[57] that the bicyclic nitrate yields are generally lower than presumed ($2-8\%$). In contrast, the MCMv3.2 recommendations for the formation yields of α-DCs ($\phi_{\alpha-DC}$, i.e. glyoxal, methylglyoxal, and dimethylglyoxal) originating from biRO + O_2 reactions were experimentally confirmed in a large number of studies (see section 4.3). α-DCs are formed along with their assumed γ-DC co-products ($\phi_{\gamma-DC}$, e.g. butenedial, 4-oxo-2-pentenal, etc.). Another class of α-DC co-products, the furanones, was tentatively identified in chamber experiments[55,56,62,63] and MCMv3.2 presumes formation yields of $\phi_{\gamma-DC}$ that are not based on experimental data.

Further uncertainties in the MCMv3.2 relate to the $biRO_2$ + HO_2 reaction (fig. 2.2). Very recent research[33,49] showed that a recycling of biRO + OH via this pathway might be operative which is so far not considered in MCMv3.2. To date, only the formation of bicyclic hydroperoxides is implemented. Generally, such bicyclic species (hydroperoxides, ketones, diols, and nitrates) are supposed to exhibit considerable reactivity towards OH in MCMv3.2. However, neither measurements of corresponding rate constants ($k_{OH+bicyclics}$) nor reaction products are reported in literature. In summary, the following parameters are chosen for MCMv3.2 sensitivity studies:

- Yields of bicyclic nitrates (ϕ_{biRNO_3}) from the $biRO_2$ + NO reactions
- Yields of unsaturated γ-dicarbonyls ($\phi_{\gamma-DC}$) from the biRO + O_2 reactions
- Yields of OH (ϕ_{OH}) from the $biRO_2$ + HO_2 reactions
- OH rate constants ($k_{OH+bicyclics}$) of bicyclic compounds (hydroperoxides, ketones, diols, nitrates)

In a pre-screening of model parameters, MCMv3.2 was found to exhibit considerable sensitivity to these four quantities. The sensitivity to other investigated parameters is minor and not discussed in detail. In the following,

the selected parameters are varied independently and the performance of the different model runs is evaluated with reference to the four low NO_x SAPHIR experiments performed in 2011 with benzene, toluene, *p*-xylene, and 1,3,5-TMB. The 2011 experiments are selected because RO_2 interferences in the HO_2 measurement were suppressed and additional OH-DOAS measurements were available. Model-measurement comparisons are consulted for the following experimental observables: the parent aromatic, the OH reactivity, OH, HO_2, RO_2, NO, NO_2, and O_3. This set of key quantities contains information on the HO_x and NO_x budgets, and the O_3 production in the photo-oxidation systems. The model-measurement comparisons are analysed quantitatively by calculating the normalized summed squared residuals R as a function of the parameters listed above. The MCMv3.2 base case simulation $S_a(0)$ serves as reference. Values of R=1 therefore indicate the model performance of the current MCMv3.2 whereas values exceeding unity denote a deterioration of the model performance. Values of R below unity indicate improved agreement between model and measurement. For the sensitivity studies, the chamber auxiliary mechanism (see section 5.3.1), measured HNO_2 concentration (if available), relative humidity, temperature, pressure, photolysis frequencies, and the replenishment flow are the only constraints. The model runs are initialized with the starting concentration of the aromatic corresponding to the initial increase of the measured OH reactivity as listed in table 5.2 (see section 5.3.3 for details). The results of the sensitivity studies are plotted for the individual parameters in figs. 5.6 ($\phi_{\mathrm{biRNO_3}}$), 5.8 ($\phi_{\gamma-\mathrm{DC}}$), 5.9 ($\phi_{\mathrm{OH}}$), and 5.10 ($k_{\mathrm{OH+bicyclics}}$).

Model sensitivity to bicyclic nitrate yields from $biRO_2$ + NO

MCMv3.2 considers bicyclic nitrate yields of 0.08, 0.11, 0.14, and 0.16 for benzene, toluene, *p*-xylene, and 1,3,5-TMB, respectively. For the sensitivity studies shown in fig. 5.6, $\phi_{\mathrm{biRNO_3}}$ is varied from 0 to 0.4. The residuals of model-measurement comparisons for the parent aromatic (panel (a)) and the OH concentration (panel (c)) do not exhibit a distinct dependence on $\phi_{\mathrm{biRNO_3}}$. In contrast, the normalized residuals for k_{OH}, HO_2, RO_2, NO, NO_2, and O_3 (panels (b), (d)-(h)) strongly depend on $\phi_{\mathrm{biRNO_3}}$. For all aromatics, R is found to decrease with decreasing $\phi_{\mathrm{biRNO_3}}$ for HO_2, RO_2 (with a single exception of benzene), and NO whereas no such a consistent behaviour is observed for k_{OH}, NO_2, and O_3. In summary, the results suggest that a reduction of $\phi_{\mathrm{biRNO_3}}$ slightly improves the performance of MCMv3.2 in predicting peroxy radical and NO concentrations. This observation can be explained by the vanishing influence of reaction channels associated with radical termination and storage of nitrogen oxides at reduced $\phi_{\mathrm{biRNO_3}}$. However, the model performance for

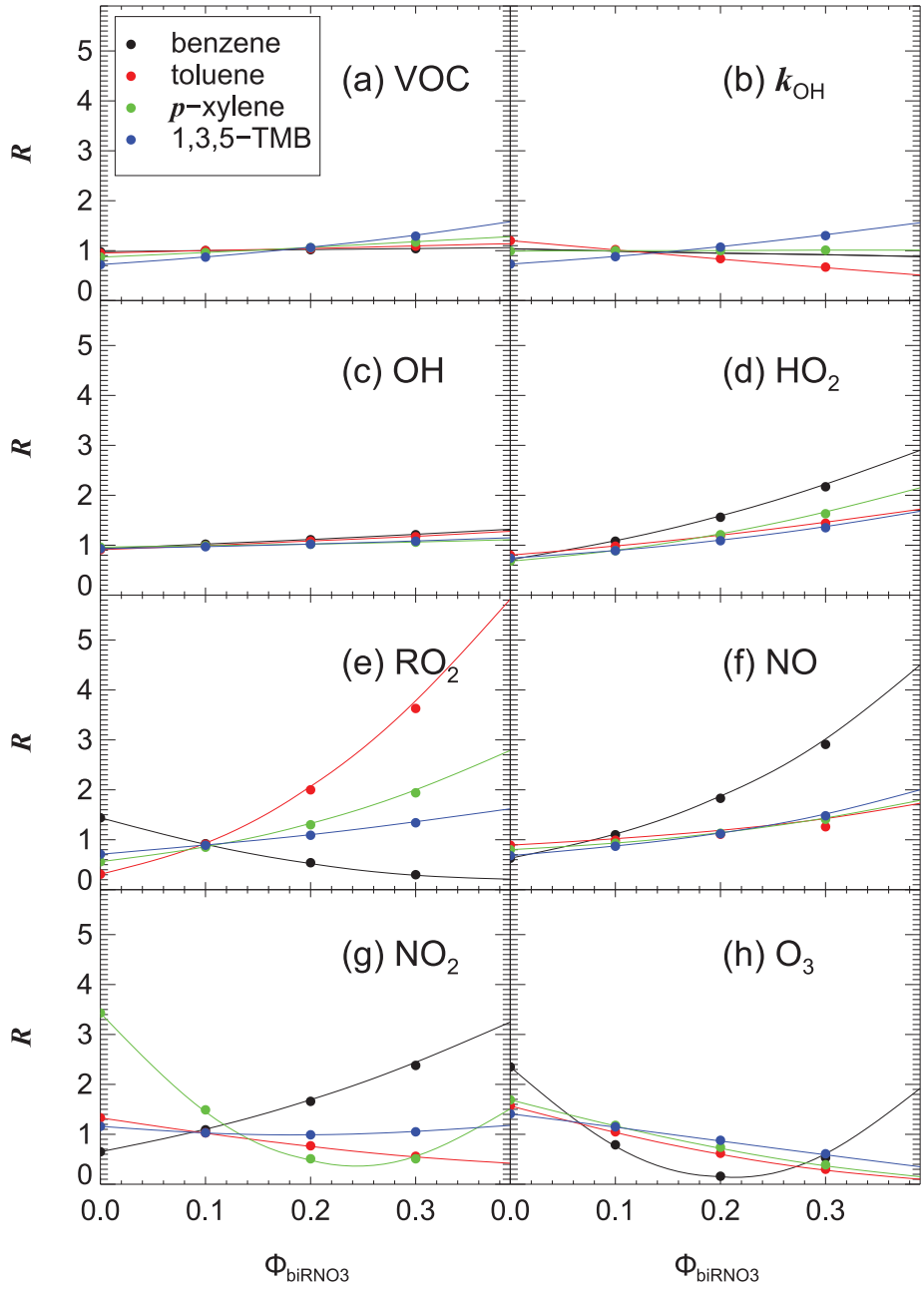

Figure 5.6: Analysis of MCMv3.2 performance as a function of bicyclic nitrate yields ($\phi_{\mathrm{biRNO_3}}$). Model-measurement comparisons are evaluated on the basis of the normalized summed squared residuals R for different target species using the MCMv3.2 base case scenario $S_a(0)$ as reference. The sensitivity studies shown here correspond to low NO_x SAPHIR experiments with benzene, toluene, *p*-xylene, and 1,3,5-TMB performed in 2011 (see table 5.2). The analysis is restricted to the time period of illumination.

the prediction of O_3 is even worse at reduced $\phi_{\mathrm{biRNO_3}}$ compared to the base case scenario (panel (h)). The origin of this effect might be related to the subsequent chemistry of biRO.

Model sensitivity to γ-DC yields from biRO + O_2

As outlined in section 2.2, the ring scission of aromatic compounds yields α-DCs that are either formed as co-products of unsaturated γ-DCs or furanones. For molecules with high structural symmetry like benzene and 1,3,5-TMB, the ring fragmentation results in the formation of glyoxal and methylglyoxal, respectively. The glyoxal co-products 4-oxo-2-butenal (MALDIAL) and 2(5H)-furanone (BZFUONE) from benzene degradation as well as the methylglyoxal co-products 4-oxo-2-methyl-2-pentenal (C5MDICARB) and 3,5-dimethyl-2(5H)-furanone (MXYFUONE) from 1,3,5-TMB degradation are assumed to be formed in equal amounts (see fig. 5.7). However, no measurements of absolute formation yields are reported in literature. For the investigation of model sensitivity to γ-DC yields, $\phi^{\mathrm{benzene}}_{\gamma-\mathrm{DC}} = \phi_{\mathrm{MALDIAL}}$ and $\phi^{1,3,5-\mathrm{TMB}}_{\gamma-\mathrm{DC}} = \phi_{\mathrm{C5MDICARB}}$ are varied from 0 to 1.

In contrast, the ring scission of toluene gives both glyoxal and methylglyoxal. MCMv3.2 considers several fragmentation patterns that are also displayed in fig. 5.7. Glyoxal is supposed to be formed as co-product of two different γ-DCs (4-oxo-2-methyl-2-butenal (C4MDIAL) and 4-oxo-2-pentenal (C5DICARB)) and as co-product of 5-methyl-2(5H)-furanone (TLFUONE) whereas methylglyoxal is formed along with MALDIAL and BZFUONE. If the formation of different γ-DCs is possible, their combined yield is treated as a single parameter for the sensitivity studies presented here and $\phi^{\mathrm{toluene}}_{\gamma-\mathrm{DC}}$ is given by the sum of ϕ_{C4MDIAL}, ϕ_{C5DICARB}, and ϕ_{MALDIAL}. This approach is justified since the subsequent chemistry of these lumped γ-DCs is assumed to be similar in MCMv3.2 and results in the formation of PAN-like derivatives after reactions with OH and NO_2. Such a storage of reactive nitrogen oxides is not considered for the subsequent chemistry of furanones. A general confinement for sensitivity studies is the ratio of $\phi_{\mathrm{glyoxal}} : \phi_{\mathrm{methylglyoxal}} = 60{:}40$ that is based on experimental data[44] and has to be maintained when $\phi^{\mathrm{toluene}}_{\gamma-\mathrm{DC}}$ is varied from 0 to 1.

The ring scission of *p*-xylene also yields both glyoxal and methylglyoxal ($\phi_{\mathrm{glyoxal}} : \phi_{\mathrm{methylglyoxal}} = 64{:}36$). However, for *p*-xylene the situation is somewhat different because the only assumed co-product of glyoxal is an unsaturated diketone (C4DBDIKET). C4MDIAL as well as 3-methyl-2(5H)-furanone (PXYFUONE) are formed as co-products of methylglyoxal (see fig. 5.7). The subsequent chemistry of C4DBDIKET is not associated with formation of PAN-derivatives. Therefore, the yields of C4DBDIKET and

C4MDIAL are not lumped for sensitivity studies and $\phi_{\mathrm{C4DBDIKET}}$=0.64 is necessarily treated as a constant contribution to $\phi_{\gamma-\mathrm{DC}}^{p-\mathrm{xylene}}$ that equals the formation yield of glyoxal. Accordingly, ϕ_{C4MDIAL} can only be varied from 0 to 0.36 resulting in $\phi_{\gamma-\mathrm{DC}}^{p-\mathrm{xylene}} = \phi_{\mathrm{C4MDIAL}} + \phi_{\mathrm{C4DBDIKET}}$ ranging from 0.64 to 1.

Fig. 5.8 displays the sensitivity of MCMv3.2 to $\phi_{\gamma-\mathrm{DC}}$ with reference to experimental data obtained for benzene, toluene, *p*-xylene, and 1,3,5-TMB. The normalized residuals R calculated for the parent aromatic (panel (a)) and the OH concentration (panel (c)) are not strongly affected by varying $\phi_{\gamma-\mathrm{DC}}$. Especially for toluene and 1,3,5-TMB, the residuals calculated for k_{OH} (panel (b)) are found to be dependent on $\phi_{\gamma-\mathrm{DC}}$ but no clear trend emerges. For all other target quantities, R is found to decrease with increasing $\phi_{\gamma-\mathrm{DC}}$ except for the residuals for RO_2 and NO_2 obtained for the benzene experiment that exhibit an opposite trend. However, the results suggest that an overall improvement of the model performance for all aromatics is achieved by setting $\phi_{\gamma-\mathrm{DC}}$ to its maximum value.

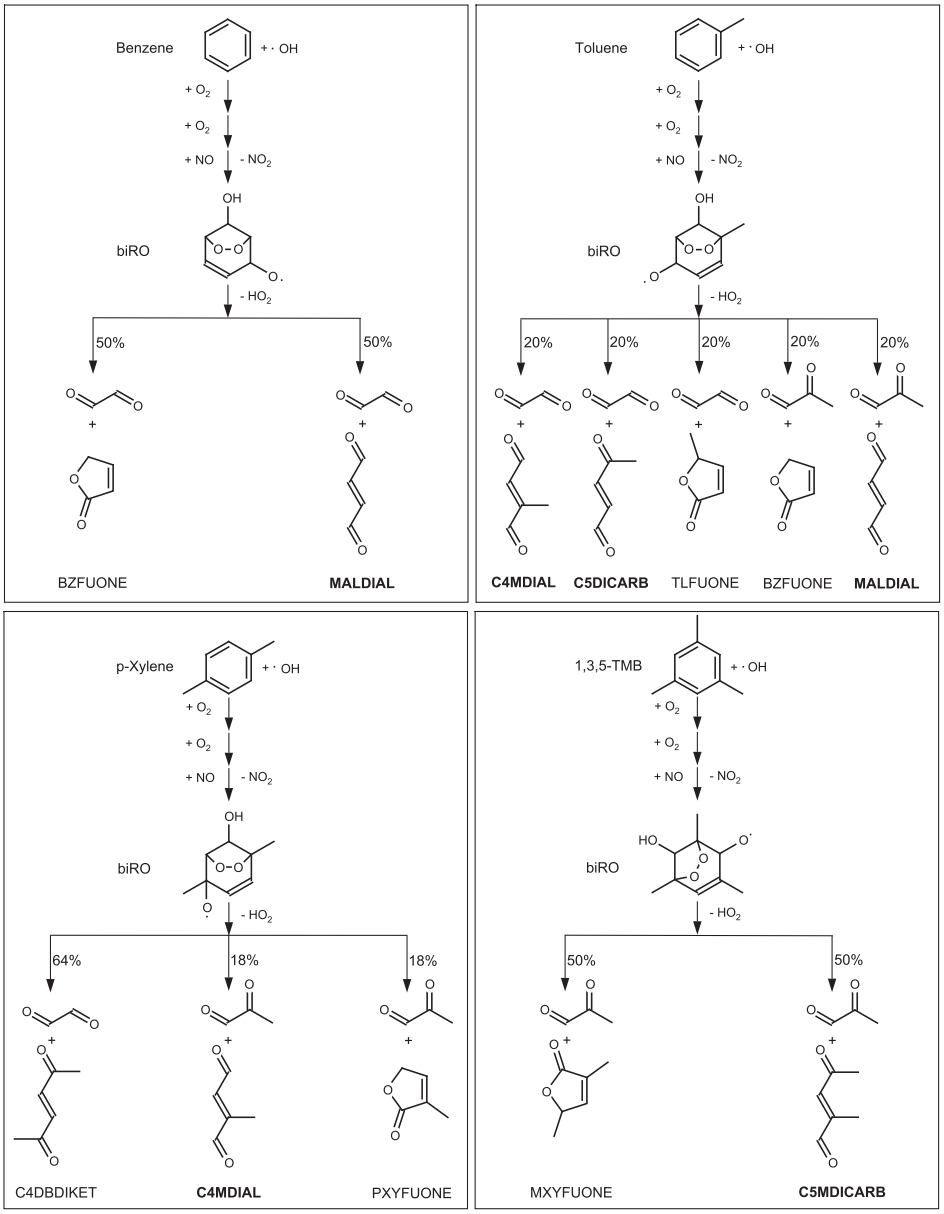

Figure 5.7: Schematic representation of ring scission channels of the atmospheric oxidation of aromatic hydrocarbons as implemented in MCMv3.2. Intermediately formed bicyclic alkoxy radicals (biRO) undergo fragmentation yielding α-DCs and corresponding co-products (unsaturated γ-DCs or furanones; denoted by their MCM designation). Note that the branching ratios for the fragmentation of toluene and *p*-xylene were assigned to reflect the ratios $\phi_{\mathrm{glyoxal}} : \phi_{\mathrm{methylglyoxal}}$ of 60:40 and 64:36, respectively. γ-DCs presented in bold face are assumed to form PAN-like derivatives in subsequent reactions with OH and NO_2 and the combined yields of these compounds are used as lumped parameters for the investigation of model sensitivity to $\phi_{\gamma-\mathrm{DC}}$.

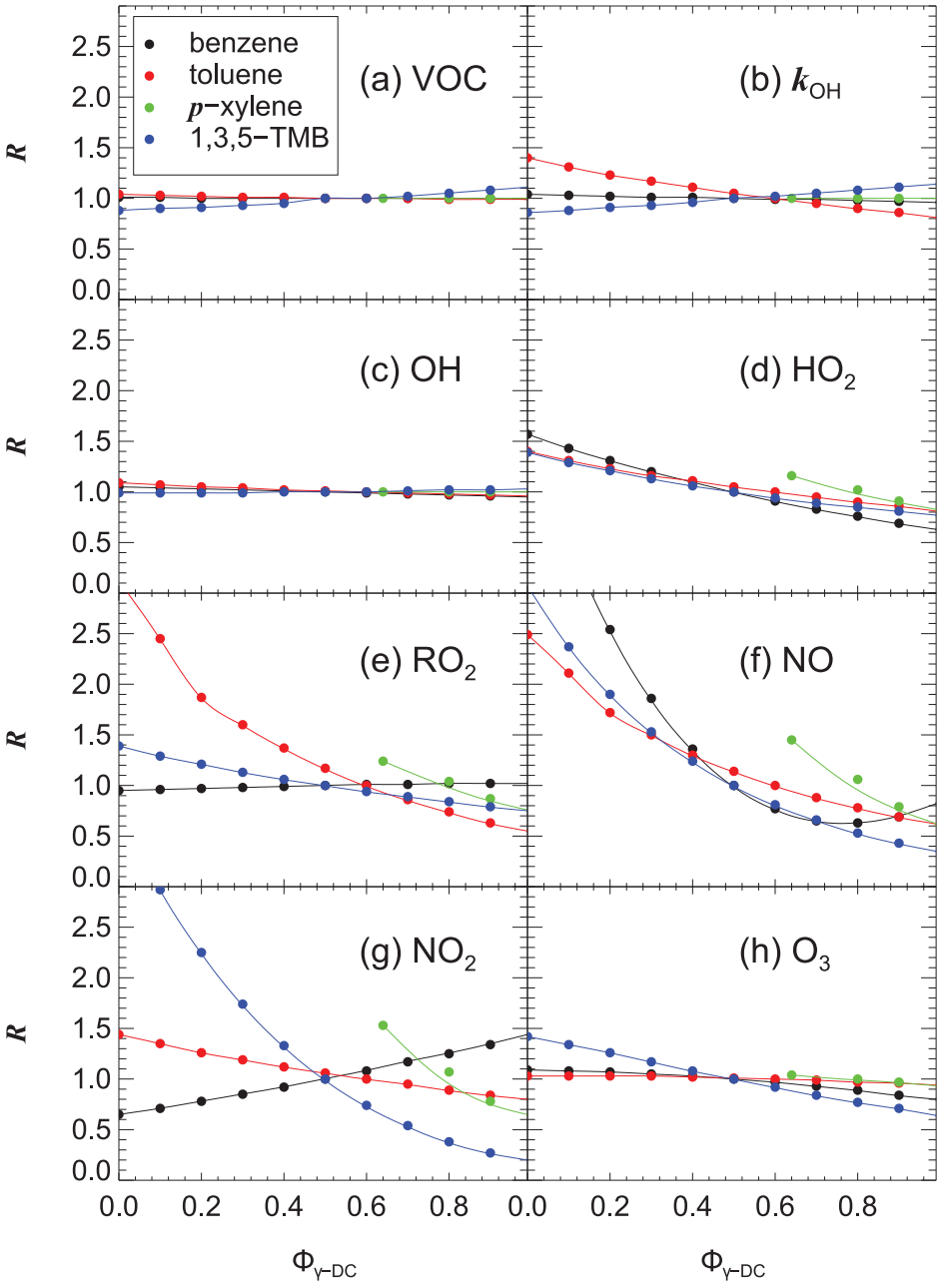

Figure 5.8: Analysis of MCMv3.2 performance as a function of γ-DC yields ($\phi_{\gamma-\mathrm{DC}}$). Model-measurement comparisons are evaluated on the basis of the normalized summed squared residuals R for different target species using the MCMv3.2 base case scenario $S_a(0)$ as reference. The sensitivity studies shown here correspond to low NO_x SAPHIR experiments with benzene, toluene, *p*-xylene, and 1,3,5-TMB performed in 2011 (see table 5.2). The analysis is restricted to the time period of illumination.

Model sensitivity to OH yields from biRO$_2$ + HO$_2$

The investigation of the model sensitivity to ϕ_{OH} reveals that especially the model performance for the prediction of peroxy radicals, NO_x, and O_3 is influenced by the implementation of a radical recycling pathway via biRO$_2$ + HO$_2$ (see fig. 5.9, panels (d)-(h)). For 1,3,5-TMB, the best agreement between model and measurements for all target quantities is achieved for values of ϕ_{OH} approaching unity. A different dependence on ϕ_{OH} is observed for the other aromatics. For example, the RO$_2$ residuals for toluene and *p*-xylene (fig. 5.9, panel (e)) show broad minima for values of ϕ_{OH} in the range of 0.2−0.8. A similar dependence is also observed for the NO residuals in the case of the benzene experiment (panel (f)) and for the NO$_2$ residuals in the case of the *p*-xylene experiment (panel (g)). Only for the RO$_2$ and O$_3$ residuals in the case of the benzene experiment, the implementation of the radical recycling pathway results in a significant deterioration of model performance for all values of ϕ_{OH} (see panels (e) and (h)). However, it is concluded that the implementation of the radical recycling reaction biRO$_2$ + HO$_2$ $\longrightarrow$ biRO + OH has the potential to significantly improve the overall model performance of MCMv3.2.

Model sensitivity to OH rate constants of bicyclic compounds

MCMv3.2 considers the formation of several bicyclic compounds (hydroperoxides, ketones, diols, nitrates) originating from radical terminating reactions (e.g. see fig. 2.2). These compounds are assumed to exhibit considerable reactivity towards OH, often on the order of $1-2\times10^{-10}$cm^{3}s^{-1}. The OH rate constants ($k_{OH+bicyclics}$) are estimated and were not assigned on the basis of experimental data. Here, the impact of these rate constants on the model performance is investigated. For convenience, values of $k_{OH+bicyclics}$ are varied simultaneously by applying a scaling factor F to all individual rate constants. A complete list of the OH rate constants of bicyclic compounds is given in the appendix B. F is varied from 0 to 1 and the impact on the model performance is shown in fig. 5.10. For nearly all target species and all aromatics, the normalized residuals R suggest that a decrease of $k_{OH+bicyclics}$ improves the model performance. The most striking exceptions are the RO$_2$ and NO$_2$ residuals for the *p*-xylene experiment and the NO$_2$ residuals for the benzene experiment (panels (e) and (g)). Major improvements are achieved for toluene and 1,3,5-TMB where especially the OH reactivity (panel (b)) and the NO$_2$ concentration (panel (g)) are affected. Values of F exceeding unity led to an deterioration of the model performance in all cases.

The scaling factor for the OH rate constants of bicyclic compounds is the

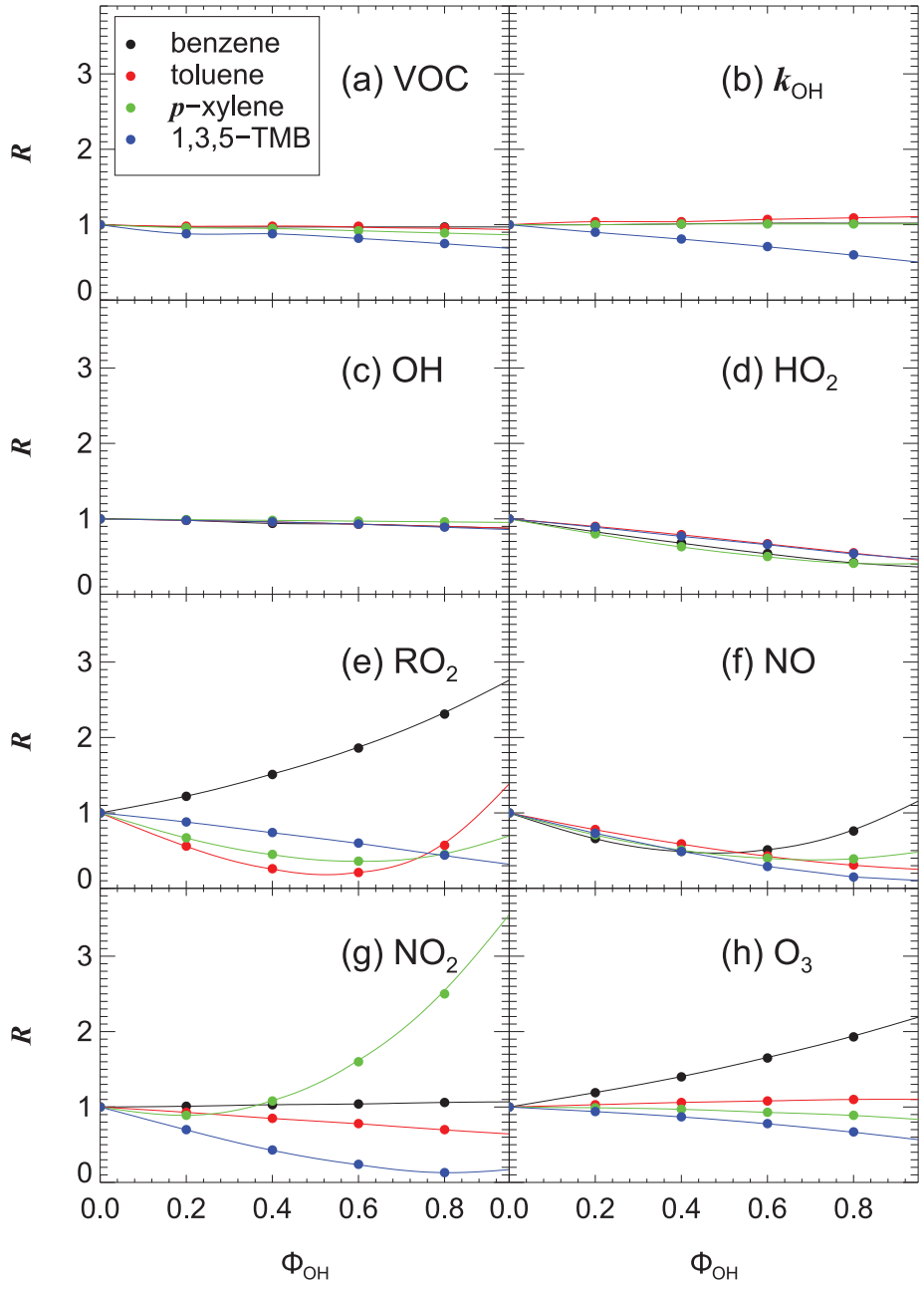

Figure 5.9: Analysis of MCMv3.2 performance as a function of OH yields (ϕ_{OH}) from the $biRO_2 + HO_2$ reaction. Model-measurement comparisons are evaluated on the basis of the normalized summed squared residuals R for different target species using the MCMv3.2 base case scenario $S_a(0)$ as reference. The sensitivity studies shown here correspond to low NO_x SAPHIR experiments with benzene, toluene, *p*-xylene, and 1,3,5-TMB performed in 2011 (see table 5.2). The analysis is restricted to the time period of illumination.

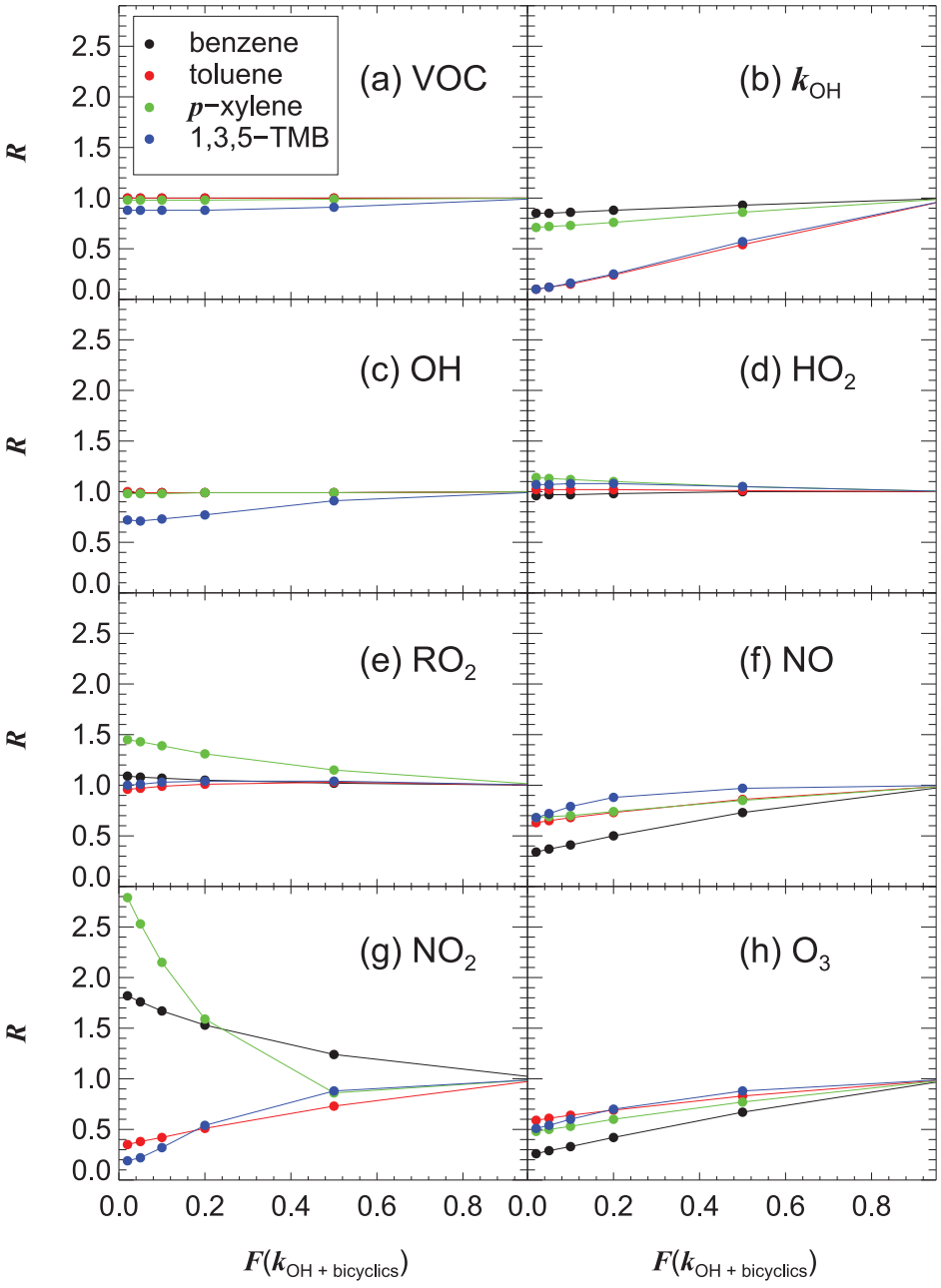

Figure 5.10: Analysis of MCMv3.2 performance as a function of OH rate constants of bicyclic compounds ($k_{OH+bicyclics}$). Model-measurement comparisons are evaluated on the basis of the normalized summed squared residuals R for different target species using the MCMv3.2 base case scenario $S_a(0)$ as reference. The sensitivity studies shown here correspond to low NO_x SAPHIR experiments with benzene, toluene, *p*-xylene, and 1,3,5-TMB performed in 2011 (see table 5.2). The analysis is restricted to the time period of illumination.

only model parameter investigated here that consistently improves the model performance with respect to k_{OH} for all aromatics. However, it is not possible to derive a recommendation for the values of the rate constants under consideration. It is merely concluded that MCMv3.2 overpredicts the OH reactivity in all aromatic photo-oxidation systems and that this observation can be rationalized by an overestimation of OH rate constants of bicyclic compounds. Additional sensitivity studies (not presented here) are performed to identify processes competing with the OH + bicyclics reactions that also reduce the OH reactivity in the photo-oxidation systems. Such processes might be condensational or photolytical losses of OH reactants. To obtain similar improvements of the model performance compared to those achieved for $F(k_{OH+bicyclics}) = 0.1$, a loss rate constant for bicyclic compounds of $1{\times}10^{-3}s^{-1}$ is required. Such a large condensational sink of bicyclics is neither consistent with wall deposition rates of OVOCs (see section 5.3.3 for details) nor with the small amounts of SOA formed during photo-oxidation experiments. Photolysis is another possible loss of bicyclics that competes with the OH reaction. MCMv3.2 resorts to the photolysis frequencies of 2-butanone, methylhydroperoxide, and isopropyl nitrate to account for the photolytical degradation of bicyclics. However, even scaling up the photolysis frequencies by a factor of up to 10^3 only slightly improves the model performance.

The tuned model scenario $S_a(1)$

Based on the sensitivity studies outlined above, a tuned version of MCMv3.2 incorporating the chamber auxiliary mechanism, the model scenario $S_a(1)$, is constructed for each investigated aromatic hydrocarbon. $S_a(1)$ generally assumes lower formation yields of bicyclic nitrates. The following numerical simulations resort to individual yields of ϕ_{biRNO_3} adapted from a recent study by Elrod.[57] Further, the yields of unsaturated γ-dicarbonyls are set to their maximum possible values to reflect the outcome of the sensitivity studies. As outlined above, the incorporation of the radical recycling via $biRO_2 + HO_2$ does not consistently improve the model performance for all aromatics and target quantities. However, an overall improvement is at least achieved for toluene and 1,3,5-TMB. Recently, Birdsall et al.[33,49] reported experimental evidence for OH recycling via $biRO_2 + HO_2$ and also estimated the corresponding rate constant. Therefore, this radical recycling pathway is considered in $S_a(1)$ for all aromatics and the corresponding OH yield of 0.5 is adapted from the findings by Birdsall et al.[33]. Finally, a scaling factor of F=0.1 for the OH rate constants of bicyclic compounds is applied. The factor is chosen to decrease $k_{OH+bicyclics}$ to values in the

range of $0.7-1.5\times10^{-11}\mathrm{cm^3s^{-1}}$ (see appendix B). This reflects the tendency to lower OH rate constants of substances with similar chemical properties like cyclohexene ($k_{\mathrm{OH+cyclohexene}} \approx 6\times10^{-11}\mathrm{cm^3s^{-1}}$) and 1-nitrocyclohexene ($k_{\mathrm{OH+1-nitrocyclohexene}} \approx 4\times10^{-11}\mathrm{cm^3s^{-1}}$).[149]
In summary, the following changes are incorporated in $S_a(1)$:

- $\phi^{\mathrm{toluene}}_{\mathrm{biRNO_3}} = 0.06$, $\phi^{p-\mathrm{xylene}}_{\mathrm{biRNO_3}} = 0.03$, and $\phi^{1,3,5-\mathrm{TMB}}_{\mathrm{biRNO_3}} = 0.02$
- $\phi_{\gamma-\mathrm{DC}} = 1$
- $\phi_{\mathrm{OH}} = 0.5$
- $F(k_{\mathrm{OH+bicyclics}}) = 0.1$

Comparison of MCMv3.2 scenarios $S_a(0)$ and $S_a(1)$

So far, the model sensitivity to individual parameters of the predominant $biRO_2$ pathway was investigated. In a next step, the performance of the base case scenario $S_a(0)$ is compared to the tuned mechanism $S_a(1)$. Diurnal profiles of the key quantities are consulted for the analysis and examples for typical low NO_x SAPHIR experiments are shown in figs. 5.11, 5.13, 5.15, and 5.17. $S_a(0)$ tends to overpredict k_{OH} and O_3 whereas OH, HO_2, and RO_2 are underestimated in almost all experiments listed in table 5.2. This necessarily results in a poor description of the NO_x profiles just after the aromatic compound is injected. To obtain more quantitative information, simulated values of the key observables (in the following indicated by the index Sim) are plotted as a function of the corresponding measurements (index Exp). The data in these scatter plots of numerical simulations and measurements (exemplified in figs. 5.12, 5.14, 5.16, and 5.18) are fitted linearly with intercepts set to zero. The fits are weighted by experimental errors and restricted to the time period of illumination and further to the presence of the aromatic hydrocarbon. The data sets shown in the scatter plots therefore contain less data points compared to the figures showing full diurnal profiles. Slopes exceeding unity are expected to indicate that the simulation overestimates the measurements whereas slopes <1 indicate an underprediction by the model. This evaluation procedure is applied for all photo-oxidation experiments with aromatics and a complete compilation of the results is given in table 5.3 where fitted slopes obtained for the different model simulations $S_a(0)$ and $S_a(1)$ are compared.

In the case of $S_a(0)$, the slopes for $[\mathrm{OH}]_{\mathrm{Sim}}$, $[\mathrm{HO_2}]_{\mathrm{Sim}}$, and $[\mathrm{RO_2}]_{\mathrm{Sim}}$ as functions of the respective experimental values are found to be in the range of 0.5−0.9 (OH), 0.4−0.9 (HO_2), and 0.3−0.9 (RO_2), respectively, for all

aromatics. Exceptions are the benzene experiment 4 where HO_2 is not underpredicted by $S_a(0)$ and the benzene experiment 5 where RO_2 is even overestimated. $S_a(1)$ generally increases the simulated radical concentrations and the corresponding slopes in the scatter plots for OH, HO_2, and RO_2 approach unity in some cases. However, in most experiments the description of peroxy radical formation by $S_a(1)$ is far from being perfect.

The scatter plots for NO and NO_2 reveal that concentrations of nitrogen oxides are overestimated by $S_a(0)$ after the aromatic is injected as indicated by slopes of 1.1−3.7 (NO) and 1.0−2.1 (NO_2, except for experiments 3, 4, and 5). The performance of $S_a(1)$ in predicting NO_x is significantly improved compared to the base case scenario for all aromatics.

Slopes obtained for the target quantities k_{OH} and O_3 using scenario $S_a(0)$ exceed unity in almost all cases. The most striking discrepancy between simulation $S_a(0)$ and the measured k_{OH} is found for 1,3,5-TMB. By using $S_a(1)$, slopes for k_{OH} generally approach unity whereas hardly any improvement is achieved for O_3.

In summary, $S_a(1)$ exhibits an improved performance compared to the base case MCMv3.2 scenario but major shortcomings still remain. Especially the O_3 formation is strongly overestimated.

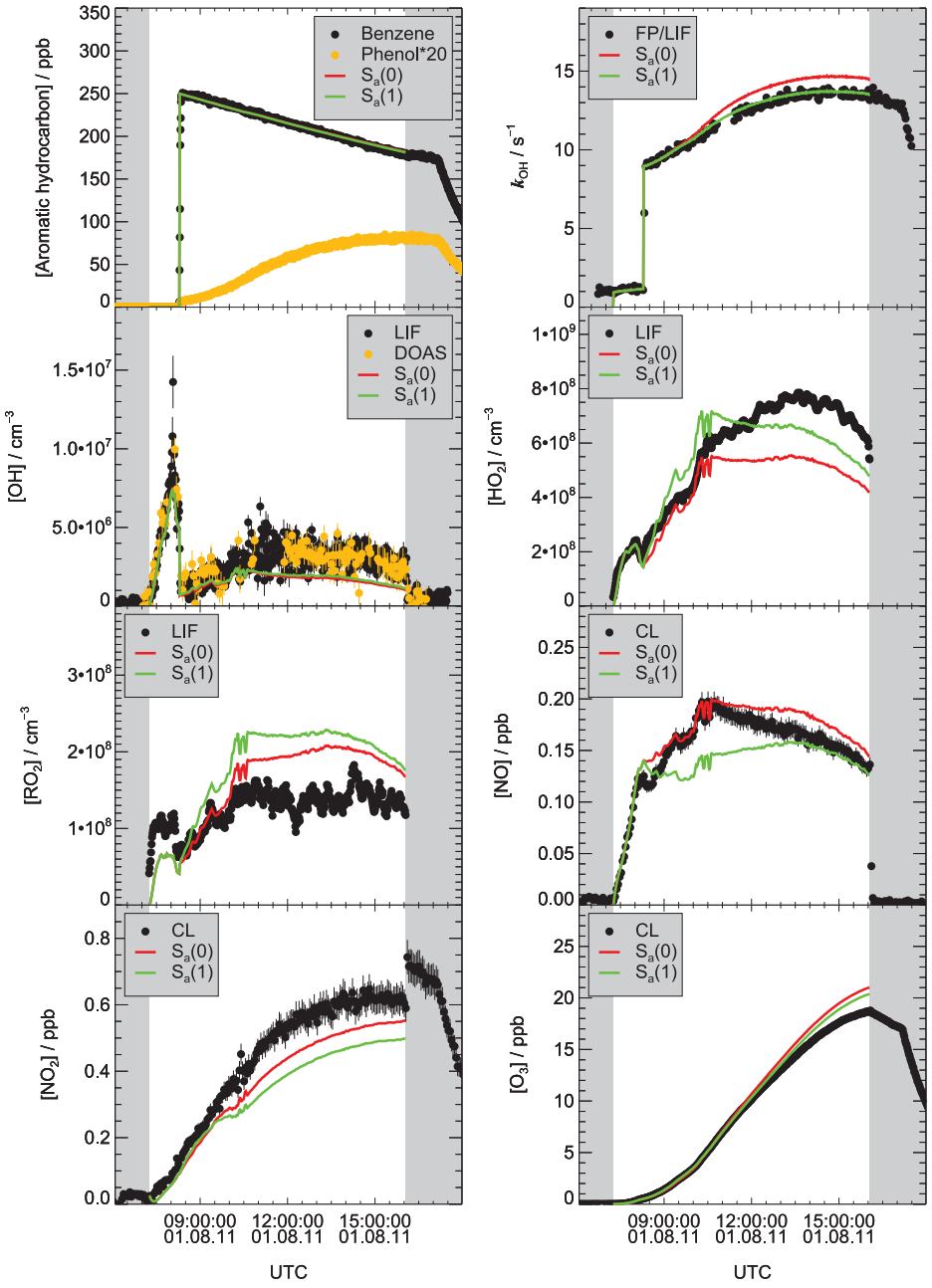

Figure 5.11: Model-measurement comparisons for a SAPHIR experiment with benzene performed on 01.08.2011. Black and yellow symbols represent measurements. Solid lines show MCMv3.2 model simulations for the base case scenario $S_a(0)$ (red) and the tuned scenario $S_a(1)$ (green). The concentration of benzene measured by PTR-MS is scaled to match the initial increase of k_{OH} (see section 5.3.3 for details).

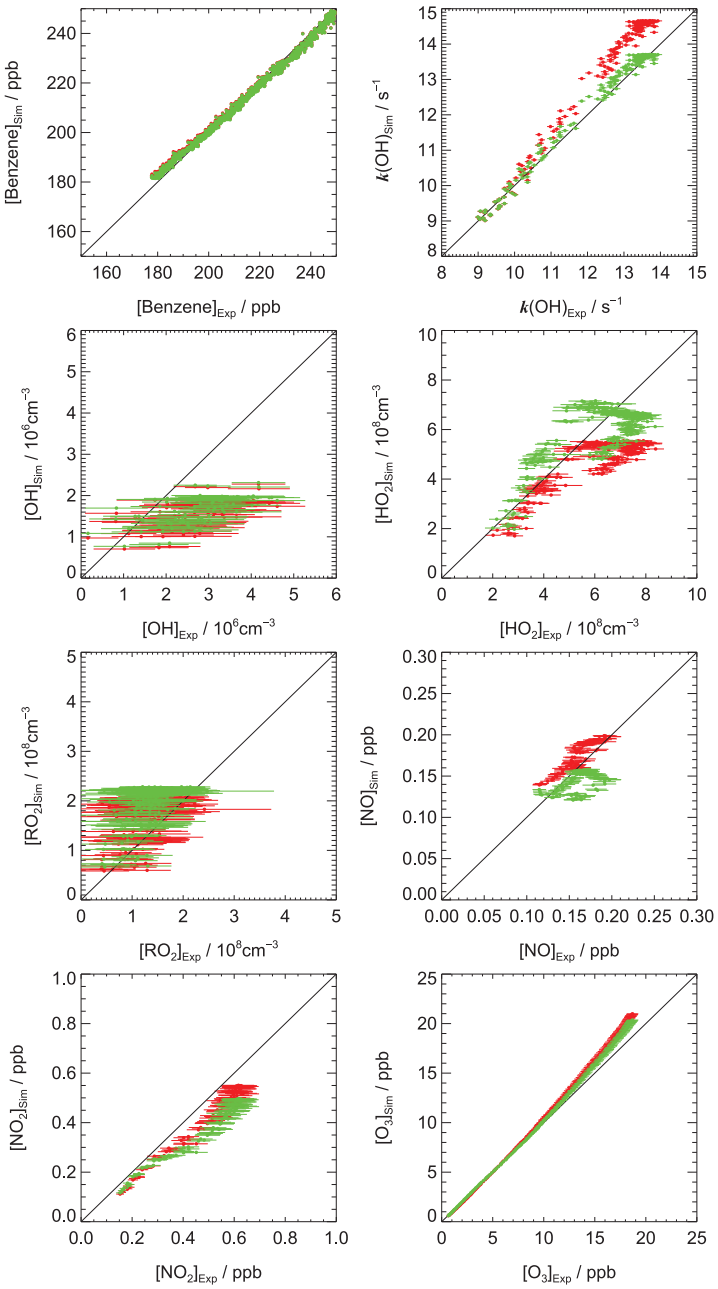

Figure 5.12: Scatter plots between key quantities numerically simulated and experimentally observed during a benzene photo-oxidation experiment under low NO_x conditions performed on 01.08.2011. Results for the MCMv3.2 base case scenario $S_a(0)$ and the tuned scenario $S_a(1)$ are represented by red and green symbols, respectively. Solid lines indicate perfect agreement between simulations and measurements. The model-measurement comparisons are restricted to the time period of illumination and to the presence of the aromatic hydrocarbon.

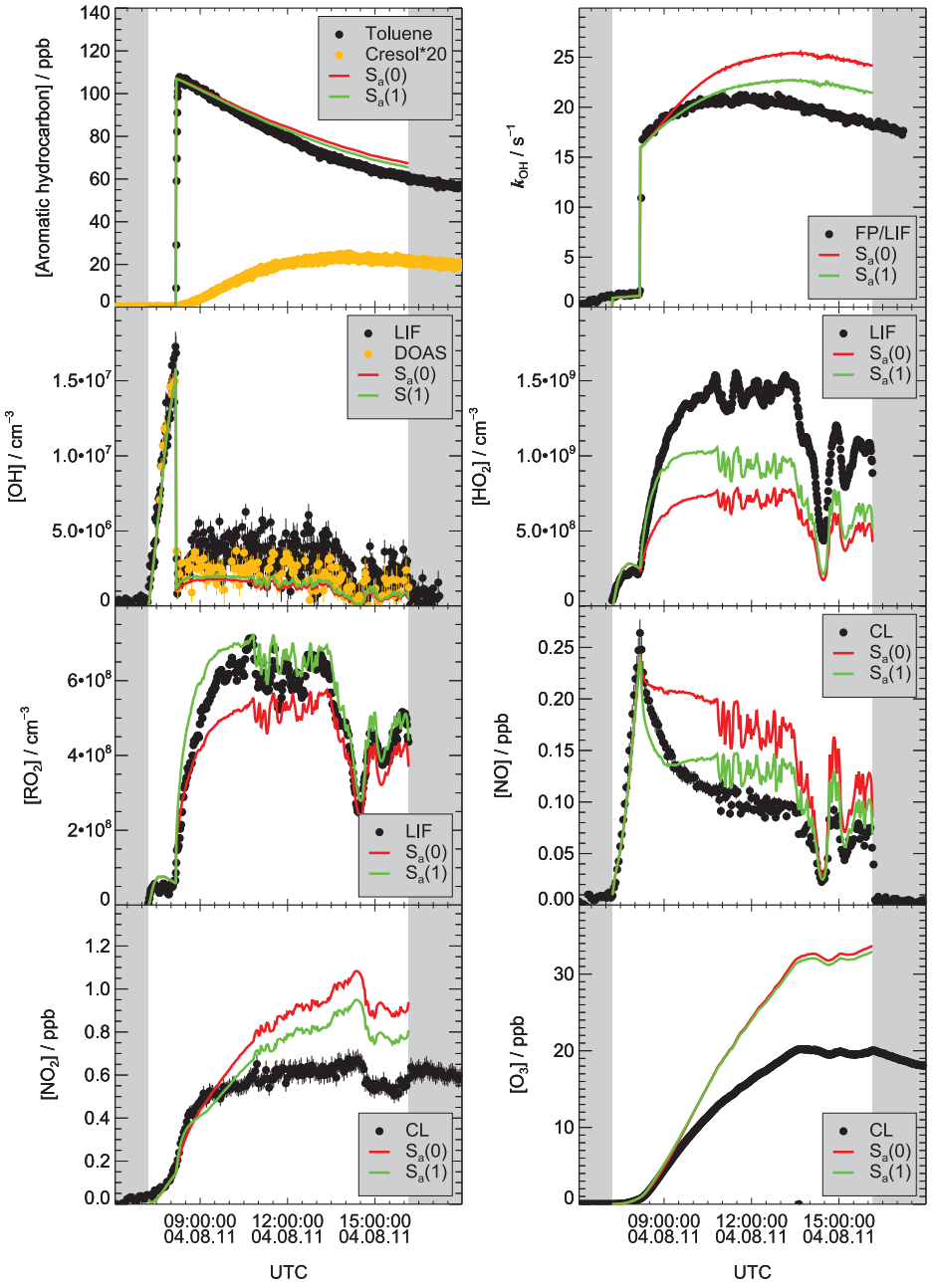

Figure 5.13: Model-measurement comparisons for a SAPHIR experiment with toluene performed on 04.08.2011. Black and yellow symbols represent measurements. Solid lines show MCMv3.2 model simulations for the base case scenario $S_a(0)$ (red) and the tuned scenario $S_a(1)$ (green). The concentration of toluene measured by PTR-MS is scaled to match the initial increase of k_{OH} (see section 5.3.3 for details).

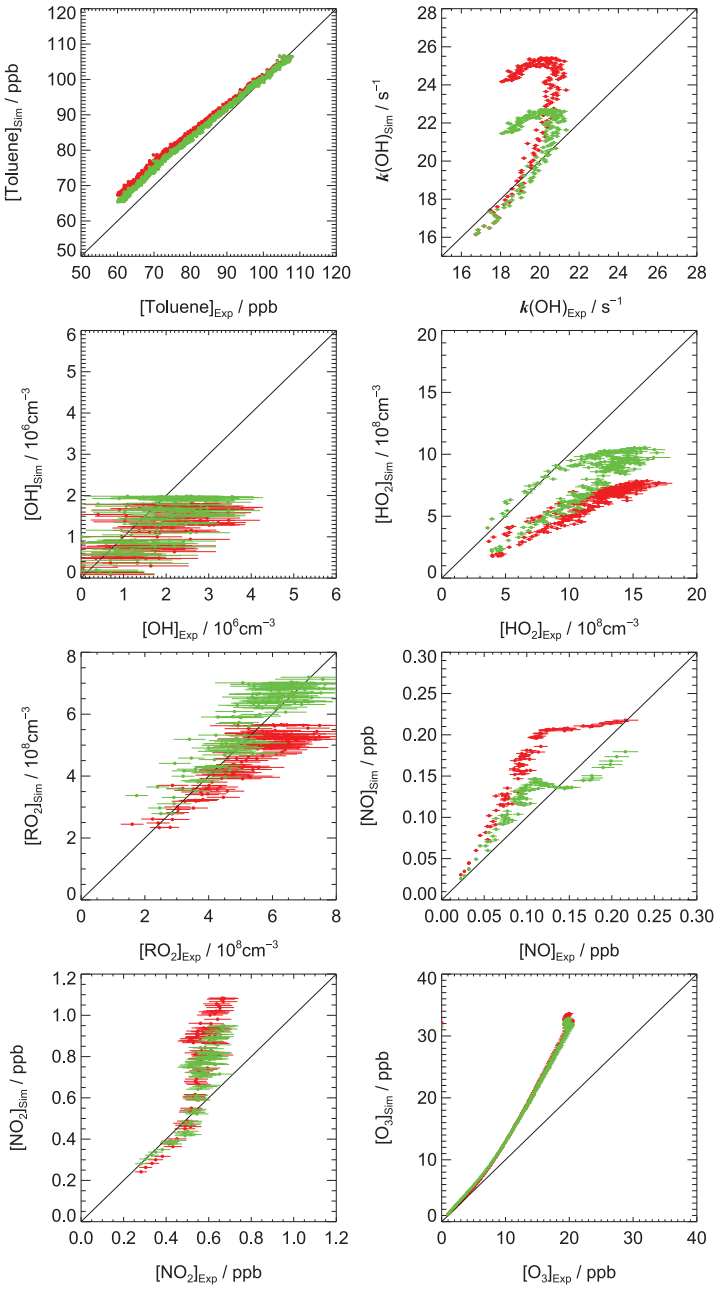

Figure 5.14: Scatter plots between key quantities numerically simulated and experimentally observed during a toluene photo-oxidation experiment under low NO_x conditions performed on 04.08.2011. Results for the MCMv3.2 base case scenario $S_a(0)$ and the tuned scenario $S_a(1)$ are represented by red and green symbols, respectively. Solid lines indicate perfect agreement between simulations and measurements. The model-measurement comparisons are restricted to the time period of illumination and to the presence of the aromatic hydrocarbon.

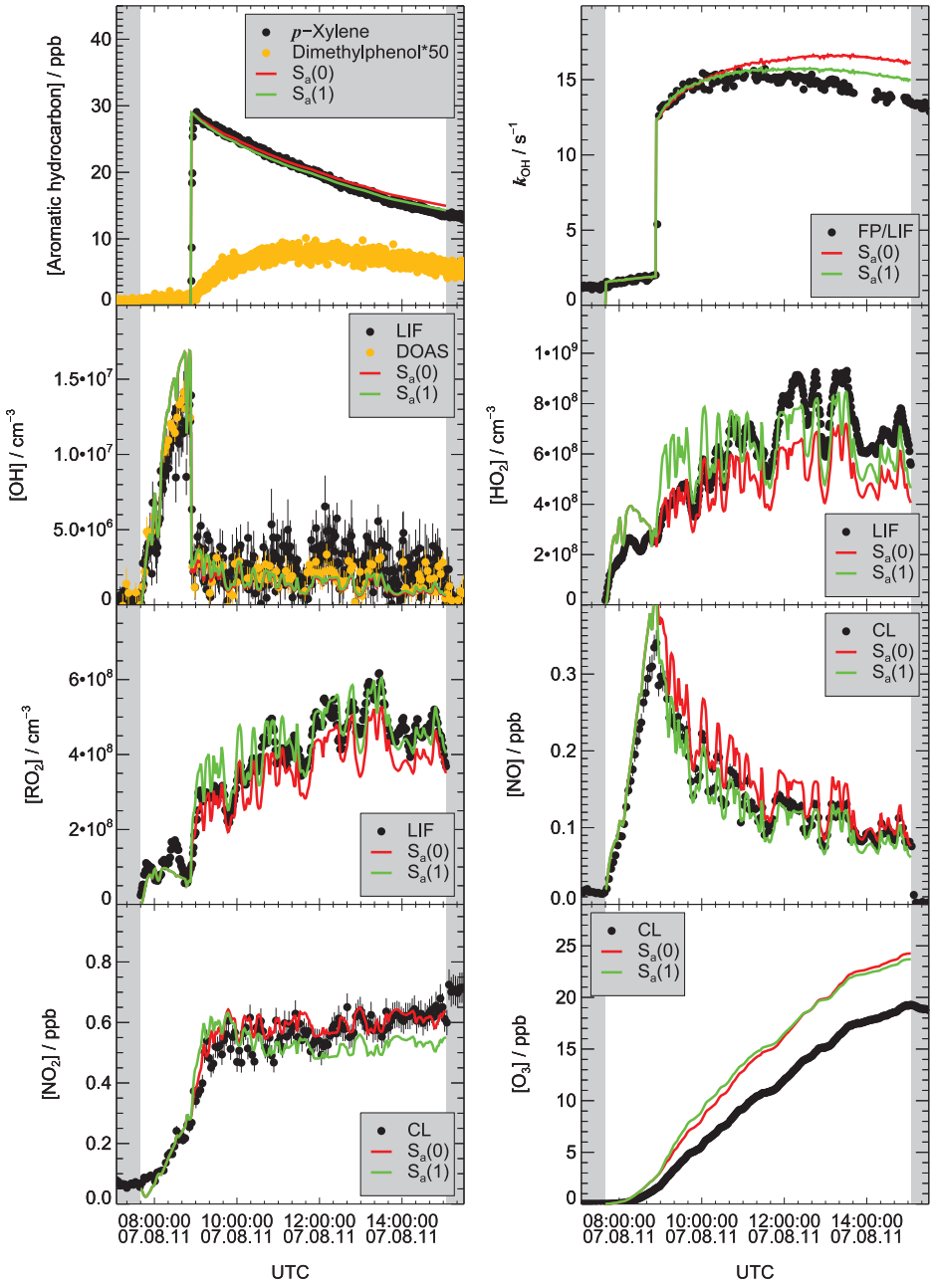

Figure 5.15: Model-measurement comparisons for a SAPHIR experiment with *p*-xylene performed on 07.08.2011. Black and yellow symbols represent measurements. Solid lines show MCMv3.2 model simulations for the base case scenario $S_a(0)$ (red) and the tuned scenario $S_a(1)$ (green). The concentration of *p*-xylene measured by PTR-MS is scaled to match the initial increase of k_{OH} (see section 5.3.3 for details).

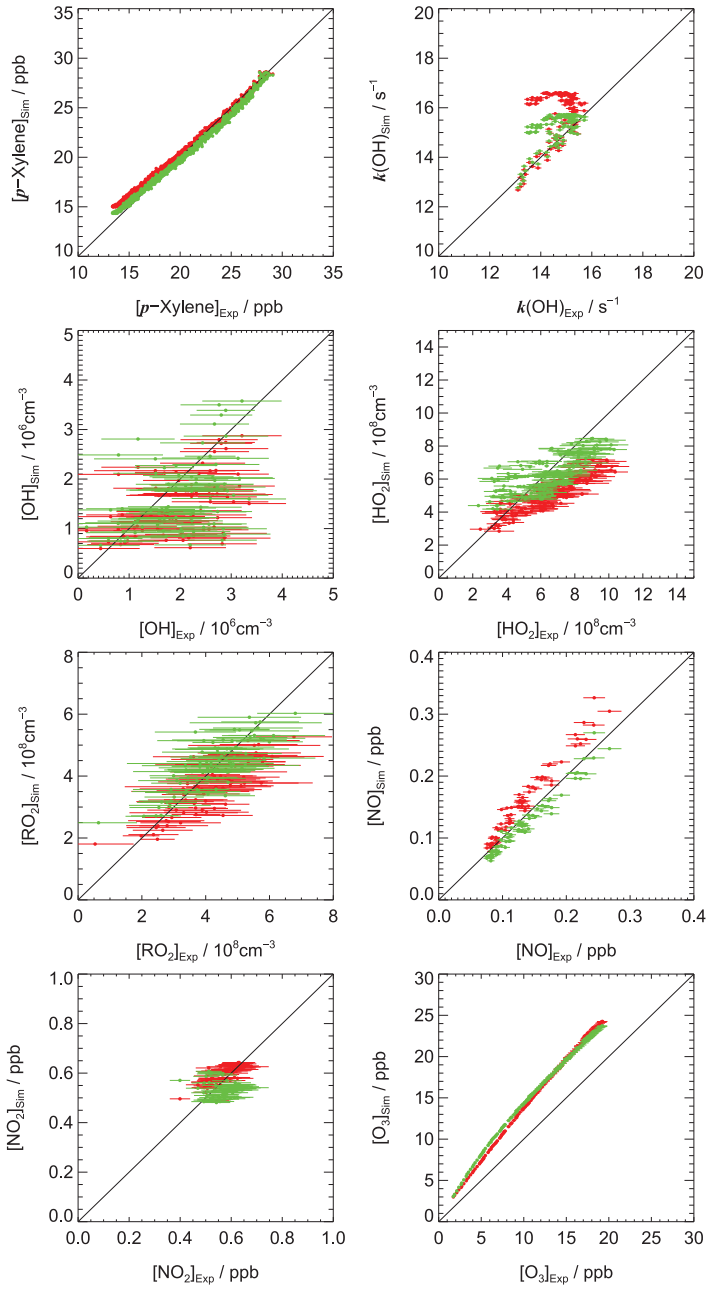

Figure 5.16: Scatter plots between key quantities numerically simulated and experimentally observed during a *p*-xylene photo-oxidation experiment under low NO_x conditions performed on 07.08.2011. Results for the MCMv3.2 base case scenario $S_a(0)$ and the tuned scenario $S_a(1)$ are represented by red and green symbols, respectively. Solid lines indicate perfect agreement between simulations and measurements. The model-measurement comparisons are restricted to the time period of illumination and to the presence of the aromatic hydrocarbon.

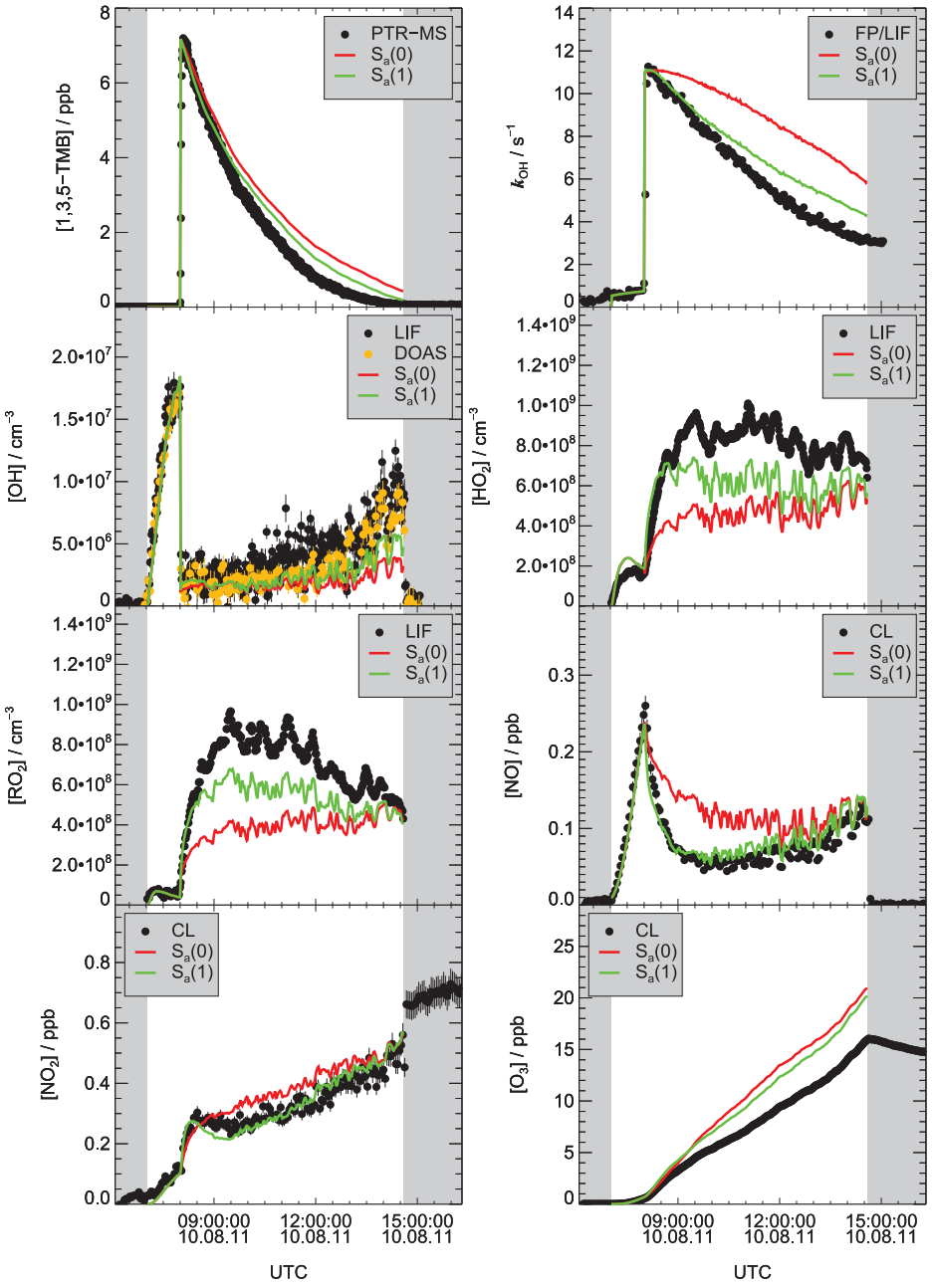

Figure 5.17: Model-measurement comparisons for a SAPHIR experiment with 1,3,5-TMB performed on 10.08.2011. Black and yellow symbols represent measurements. Solid lines show MCMv3.2 model simulations for the base case scenario $S_a(0)$ (red) and the tuned scenario $S_a(1)$ (green). The concentration of 1,3,5-TMB measured by PTR-MS is scaled to match the initial increase of k_{OH} (see section 5.3.3 for details).

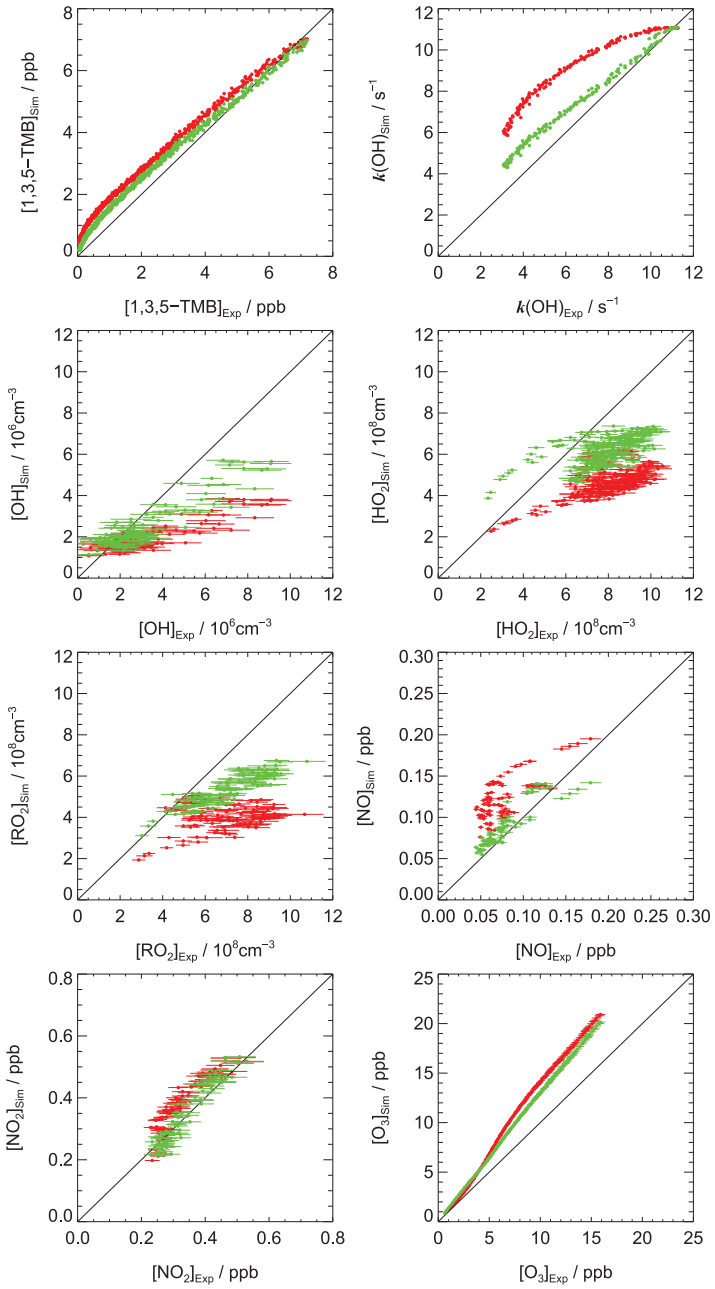

Figure 5.18: Scatter plots between key quantities numerically simulated and experimentally observed during a 1,3,5-TMB photo-oxidation experiment under low NO_x conditions performed on 10.08.2011. Results for the MCMv3.2 base case scenario $S_a(0)$ and the tuned scenario $S_a(1)$ are represented by red and green symbols, respectively. Solid lines indicate perfect agreement between simulations and measurements. The model-measurement comparisons are restricted to the time period of illumination and to the presence of the aromatic hydrocarbon.

Table 5.3: Fitted slopes for values of simulated key quantities as a function of corresponding measurements during SAPHIR experiments. Fits are restricted to the time period of illumination and further to the presence of aromatic hydrocarbon. OH-LIF data (experiments in 2010) and OH-DOAS data (experiments in 2011) are used for the evaluation.

			Key quantity							
Exp.	Date		[VOC]	k_{OH}	[OH]	$[HO_2]$	$[RO_2]$	[NO]	$[NO_2]$	$[O_3]$
					Benzene					
3	07.06.2010	$S_a(0)$	1.0	1.1	0.6	0.9	0.6	1.1	0.9	1.1
		$S_a(1)$	1.0	1.1	0.6	1.1	0.6	0.9	0.8	1.1
4	23.06.2010	$S_a(0)$	–	1.0	0.7	1.0	0.5	1.1	1.0	1.2
		$S_a(1)$	–	1.0	0.8	1.2	0.5	0.9	0.9	1.2
5	01.08.2011	$S_a(0)$	1.0	1.1	0.5	0.7	1.3	1.1	0.8	1.0
		$S_a(1)$	1.0	1.0	0.6	0.9	1.4	0.9	0.8	1.0
6*	08.06.2010	$S_a(0)$	1.0	1.1	0.6	0.4	0.4	1.5	1.2	1.0
		$S_a(1)$	1.0	1.1	0.6	0.6	0.4	1.1	1.1	1.1
7*	25.06.2010	$S_a(0)$	–	1.0	0.9	0.7	0.4	1.5	1.3	1.1
		$S_a(1)$	–	0.9	1.0	0.8	0.4	1.2	1.1	1.1
					Toluene					
8	05.07.2010	$S_a(0)$	–	1.2	0.6	0.6	0.4	1.4	1.1	1.3
		$S_a(1)$	–	1.1	0.6	0.8	0.5	1.1	0.9	1.3
9	04.08.2011	$S_a(0)$	1.1	1.2	0.6	0.5	0.9	1.6	1.4	1.6
		$S_a(1)$	1.0	1.1	0.7	0.7	1.1	1.2	1.2	1.5
10*	13.06.2010	$S_a(0)$	1.0	1.1	0.8	0.4	0.3	3.4	2.1	1.1
		$S_a(1)$	1.0	1.0	0.9	0.6	0.4	2.1	1.6	1.2
					***p*-Xylene**					
11	14.06.2010	$S_a(0)$	1.0	1.1	0.6	0.8	0.5	1.3	1.0	1.3
		$S_a(1)$	0.9	1.1	0.7	1.1	0.5	1.1	0.9	1.3
12	02.07.2010	$S_a(0)$	–	1.1	0.6	0.8	0.3	1.3	1.1	1.3
		$S_a(1)$	–	1.0	0.7	1.0	0.4	1.0	1.1	1.4
13	07.08.2011	$S_a(0)$	1.0	1.1	0.7	0.8	0.9	1.2	1.1	1.3
		$S_a(1)$	1.0	1.0	0.8	1.0	1.0	0.9	0.9	1.3
14*	16.06.2010	$S_a(0)$	1.1	1.2	0.6	0.7	0.4	1.7	1.2	1.0
		$S_a(1)$	1.0	1.1	0.7	0.9	0.5	1.1	1.0	1.1
15*	30.06.2010	$S_a(0)$	–	1.1	0.7	0.6	0.2	1.8	1.4	1.0
		$S_a(1)$	–	1.1	0.7	0.8	0.3	1.2	1.2	1.1
					1,3,5-TMB					
16	17.06.2010	$S_a(0)$	1.0	1.3	0.8	0.8	0.5	1.9	1.4	1.5
		$S_a(1)$	0.9	1.1	0.9	1.1	0.7	1.3	1.1	1.5
17	01.07.2010	$S_a(0)$	–	1.4	0.7	0.7	0.3	1.5	1.0	1.2
		$S_a(1)$	–	1.1	0.9	0.9	0.3	1.1	1.0	1.2
18	10.08.2011	$S_a(0)$	1.1	1.5	0.5	0.6	0.6	1.7	1.2	1.4
		$S_a(1)$	1.1	1.2	0.7	0.8	0.8	1.2	1.0	1.3
19*	21.06.2010	$S_a(0)$	1.3	1.6	0.6	0.3	0.2	3.7	1.7	0.7
		$S_a(1)$	0.9	1.2	0.9	0.7	0.4	1.5	1.2	1.0
20*	28.06.2010	$S_a(0)$	–	1.5	0.6	0.4	0.2	3.2	1.4	0.8
		$S_a(1)$	–	1.2	0.9	0.7	0.3	1.6	1.3	1.1

* High NO_x experiment.

5.3.3 Primary phenolic oxidation product yields

The evaluation of MCMv3.2 against SAPHIR experiments outlined in the previous section aimed at the identification of common parameters for the improvement of photochemical degradation mechanisms of aromatics. The evaluation procedure presented here is focused on the determination of primary phenolic product yields that are specific for each aromatic hydrocarbon.

A prerequisite for the determination of product yields is the knowledge of all loss processes of the phenolic compounds and the aromatic precursors. These losses are the dilution caused by the replenishment flow, the chemical losses due to reactions with OH, and possibly wall deposition. Dilution and chemical losses are accounted for in the data analysis by using the measured replenishment flow and additionally the OH-DOAS data as constraints in the numerical simulations. The influence of deposition of polar organic substances to the chamber walls was investigated in separate experiments where test injections of phenol, *o*-cresol, dimethylphenol, and trimethylphenol into the dark humidified chamber were done. Phenolic compounds were injected directly into the chamber via a heated flask without using the injection port to avoid contamination of the permanently installed tubings. Prior to the injection of VOCs, CO_2 was added that served as tracer for the dilution rate. VOC decay rates were observed by PTR-MS and the OH reactivity instrument for several hours and compared to the dilution rate of CO_2. For all phenolic compounds, decay rates of about $1 \times 10^{-5} s^{-1}$ were found which is in good agreement with the CO_2 dilution rate. Thus, wall losses of phenols are negligible for the data analysis.

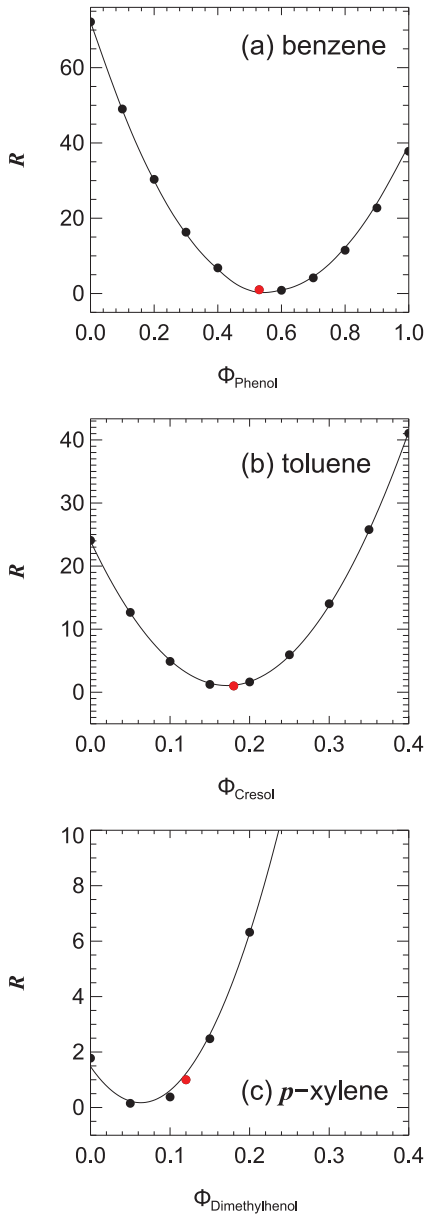

Figure 5.19: Analysis of MCMv3.2 performance in describing the formation of primary phenolic oxidation products as a function of the corresponding yields ϕ_{phenol}, ϕ_{cresol}, and $\phi_{\text{dimethylphenol}}$. Model-measurement comparisons are evaluated on the basis of the normalized summed squared residuals R using the MCMv3.2 base case scenario $S_a(0)$ as reference. Red points indicate these reference cases. The sensitivity studies shown here correspond to low NO_x SAPHIR experiments with benzene, toluene, and *p*-xylene performed in 2011 (see table 5.2). Model runs are constrained to OH-DOAS data and initialized with VOC concentrations corresponding to the initial increase of k_{OH} measured upon injection of the aromatic.

Phenolic oxidation product yields are determined from SAPHIR experiments performed in 2011 and diurnal profiles of phenol, cresol, and dimethylphenol are shown in figs. 5.11, 5.13, and 5.15 (yellow symbols) for photo-oxidation experiments with benzene, toluene, and *p*-xylene, respectively. In most photo-oxidation experiments (see table 5.2) and in the case of the test injections of phenolic compounds into the dark chamber, the initial concentration of the VOC measured by PTR-MS and the concentration calculated from the initial increase of k_{OH} (using MCM recommended rate constants) are found to be lower than calculated from the injected amount. This observation can be rationalized by uncertainties of the injection method. Moreover, in most cases, the initial PTR-MS measurements are found to be lower than the concentration inferred from the initial increase of k_{OH}. This discrepancy can be explained by calibration errors of the PTR-MS instrument, uncertainties of k_{OH}, or by errors of the rate constants used for the conversion of k_{OH} to VOC concentrations. However, the estimated combined uncertainties of k_{OH} and OH rate constants are too small to explain some of the observed discrepancies. Consequently, they are attributed to the PTR-MS calibration. This assumption is further supported by two observations: (i) During SAPHIR experiments with CO, the initial carbon monoxide concentration, as calculated from the injected amount and measured by RGA, is in very good agreement with the concentration inferred from the initial increase of k_{OH} (table 5.2) indicating that OH reactivity measurements are not subject to a systematic bias. (ii) For most of the photo-oxidation experiments with aromatics, the VOC concentration calculated from the injected liquid volume is also in fair agreement with the concentration calculated from the initial OH reactivity increase (table 5.2). For consistency reasons, all PTR-MS data of aromatic precursors are therefore treated as relative quantities and are scaled by individual factors to match the initial k_{OH}. The scaling factors for the phenolic compounds are determined independently during the test experiments performed under dark conditions.

Comparable to the data analysis deployed in the previous section, model-measurement comparisons are consulted and the normalized residuals for the respective phenolic compounds are minimized by varying the yields presumed in MCMv3.2. Fig. 5.19 shows the dependence of the normalized residuals for phenol from benzene degradation, cresol from toluene degradation, and dimethylphenol from *p*-xylene degradation. Minima are obtained for phenolic compound yields of $\phi_{\mathrm{phenol}}^{\mathrm{benzene}} = 0.55 \pm 0.10$, $\phi_{\mathrm{cresol}}^{\mathrm{toluene}} = 0.17 \pm 0.05$, and $\phi_{\mathrm{dimethylphenol}}^{p-\mathrm{xylene}} = 0.05 \pm 0.03$. Errors are estimated from the uncertainties of model-measurement comparisons. For the yield of trimethylphenol from 1,3,5-TMB degradation such an analysis is not presented because the

trimethylphenol data are too noisy and close to the detection limit. It is only concluded that the formation yield found in this study is well below 5%.

5.3.4 OH budgets during photo-oxidation experiments

The results obtained by model-measurement comparisons reveal that MCM tends to underestimate the OH concentration in aromatic photo-oxidation systems. This underprediction of OH concentrations is not necessarily reflected by an unbalanced OH budget. The analysis of the OH budget outlined in the following is widely independent of numerical MCMv3.2 simulations. Based on measured quantities, all OH sources and sinks are considered. The overall OH production rate P_{OH} is given by the OH recycling rate via the HO_2 + NO reaction (R7) plus the primary production rates mainly resulting from photolysis of HNO_2 and O_3.

$$\begin{aligned} P_{OH} &= k_{HO_2+NO} \times [HO_2] \times [NO] \\ &+ J_{HNO_2} \times [HNO_2] + J_{O^1D} \times [O_3] \times 2 \times c_{OH} \end{aligned} \quad (5.5)$$

c_{OH} denotes the fraction of $O(^1D)$ (formed by photolysis of O_3, see R1) that reacts with H_2O yielding two OH radicals (see R2, $c_{OH} \approx 0.1$). Note that the bulk of P_{OH} during SAPHIR experiments proceeds via R7 whereas the primary production caused by photolytical processes is of minor importance. The overall OH destruction rate D_{OH} is given by the product of the total OH reactivity and the OH concentration.

$$D_{OH} = k_{OH} \times [OH] \quad (5.6)$$

This is the first time that all quantities needed for the calculation of P_{OH} and D_{OH} are measured simultaneously during SAPHIR experiments. D_{OH} is a robust quantity since all chemical OH losses are accounted for by the measurement of the total OH reactivity k_{OH}. In contrast P_{OH} might suffer from unknown OH recycling processes and/or unknown primary OH sources. In a steady-state assumption for OH, its production rate should be balanced by an equally large destruction rate and measurements of P_{OH} and D_{OH} are used to check whether this is the case for the photo-oxidation experiments with aromatics. This experimental approach can help to clarify the question if OH is produced via pathways other than those considered in eq. 5.5. The OH budget analysis is widely independent of numerical model simulations. Only the HO_2 data are slightly corrected based on calculations using MCMv3.2 to account for the influence of interfering organic peroxy radicals (see section 5.2). An OH budget analysis using uncorrected HO_2 data leads to similar

Table 5.4: Properties of key instruments for the investigation of the OH budgets during SAPHIR experiments.

Instrument	Measurement time / s	1σ precision	Accuracy / %
OH (LIF)	47	0.3×10^6cm^{-3}	10
OH (DOAS)	205	0.8×10^6cm^{-3}	6.5
k_{OH}	180	0.3 s^{-1}	5
HO_2 (LIF)	47	1×10^7cm^{-3}	10
NO (CL)	90	0.05 ppb	7

results and does not change the conclusions outlined below. Therefore, only the corrected HO_2 data are deployed here.

OH budgets during photo-oxidation experiments in SAPHIR are evaluated by means of a correlation and regression analysis for the OH destruction rate (D_{OH}) as a function of the OH production rate (P_{OH}). OH turnover rates are exclusively calculated from measured quantities according to eqs. 5.5 and 5.6. For this analysis all experimental data are averaged to the time grid of the instrument with the lowest time resolution (either the OH reactivity instrument during experiments in 2010 or the DOAS instrument during experiments in 2011). The regression analysis[150] is weighted by the maximum errors for D_{OH} and P_{OH} resulting from the individual contributions (table 5.4) of all measured quantities (error propagation). The results of the correlation and regression analysis are listed in table 5.5 and also plotted in figs. 5.20−5.22 for all SAPHIR experiments with CO and aromatic compounds performed in 2010 and 2011. A typical linear correlation coefficient (R^2) of 0.7 (ranging between 0.56 and 0.93 with a single exception of 0.37) indicates that D_{OH} and P_{OH} are strongly correlated. Moreover, the summed squared residuals divided by the degrees of freedom (χ^2/DOF) are close to unity for most of the experiments confirming that the relation between D_{OH} and P_{OH} is consistent with a linear dependence within the experimental errors. The regression analysis almost exclusively gives slopes slightly exceeding unity. Obtained intercepts are small ($\pm$0.8 ppb h^{-1}) and not significantly different from zero in almost all experiments.

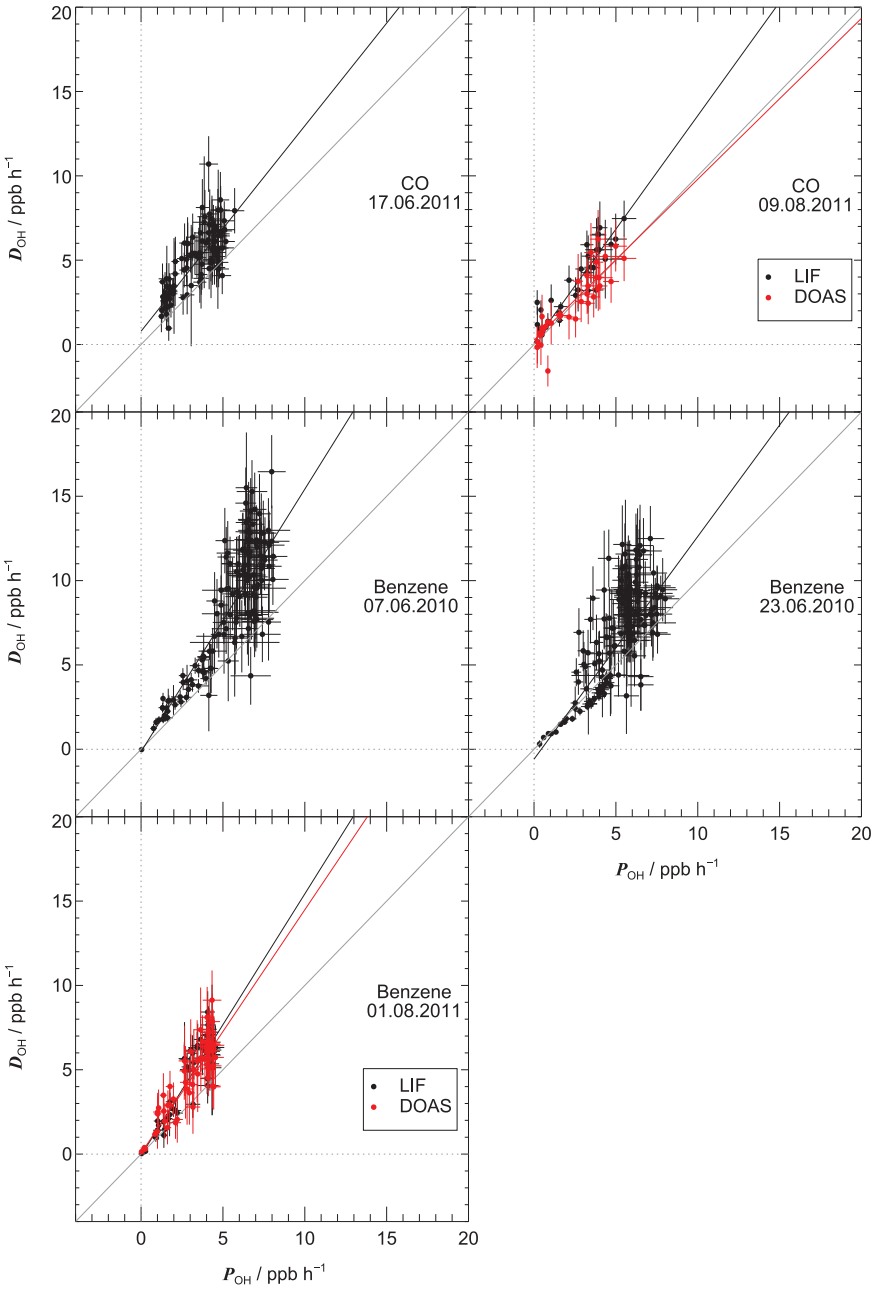

Figure 5.20: Correlation of OH destruction rates (D_{OH}) and production rates (P_{OH}) for SAPHIR experiments with CO and benzene under low NO_x conditions. Black and red lines represent the results of the regression analysis (as listed in table 5.5) using the OH-LIF and the OH-DOAS data for the calculation of D_{OH}, respectively.

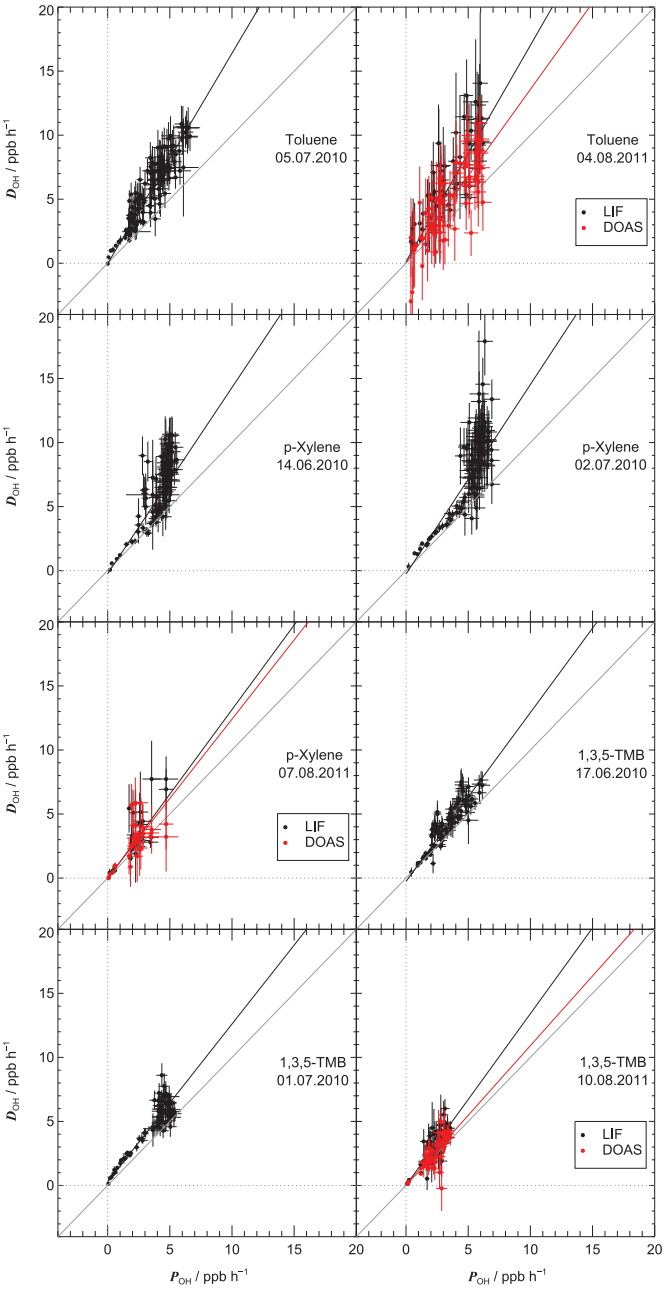

Figure 5.21: Correlation of OH destruction rates (D_{OH}) and production rates (P_{OH}) for SAPHIR experiments with toluene, *p*-xylene, and 1,3,5-TMB under low NO_x conditions. Black and red lines represent the results of the regression analysis (as listed in table 5.5) using the OH-LIF and the OH-DOAS data for the calculation of D_{OH}, respectively.

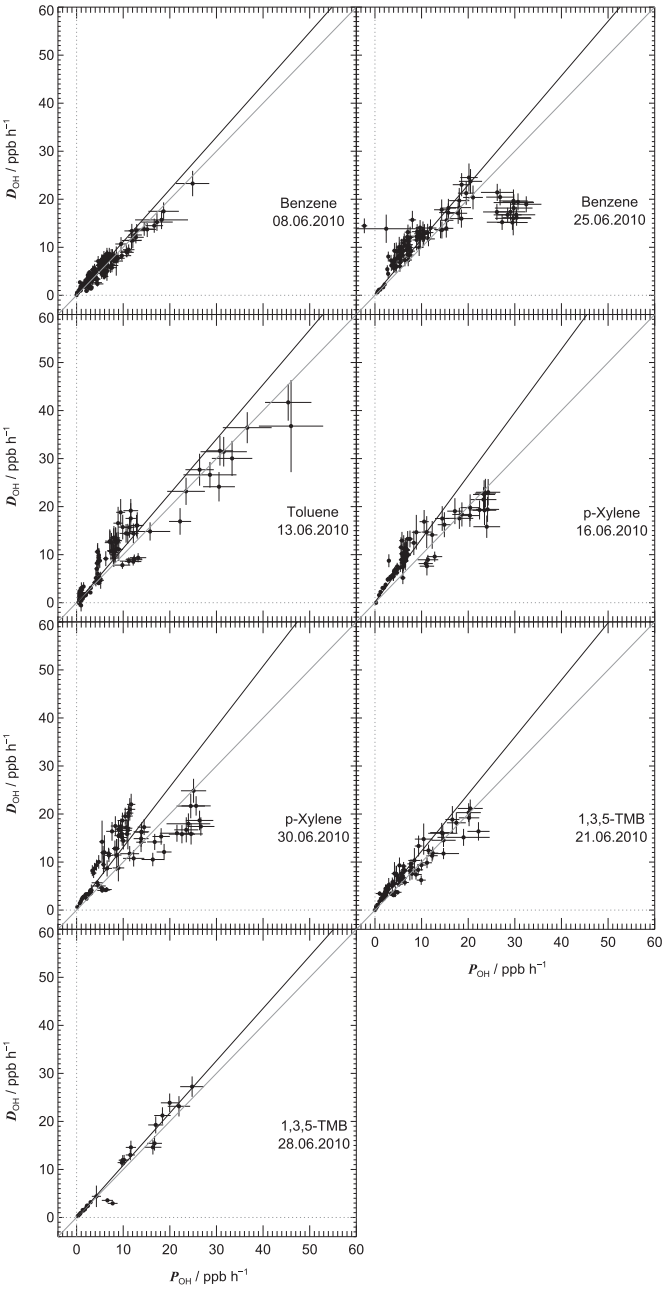

Figure 5.22: Correlation of OH destruction rates (D_{OH}) and production rates (P_{OH}) for SAPHIR experiments with benzene, toluene, *p*-xylene, and 1,3,5-TMB under high NO_x conditions. Black lines represent the results of the regression analysis (as listed in table 5.5) using the OH-LIF data for the calculation of D_{OH}.

Table 5.5: Results of the linear correlation and regression analysis for the OH radical turnover rates D_{OH} vs. P_{OH} measured in SAPHIR. Data are averaged to the time grid of the OH reactivity instrument for experiments performed in 2010 and to the time grid of the DOAS instrument for experiments performed in 2011. Results obtained using OH-DOAS data are indicated in bold face. N denotes the number of data points.

Exp.	Date	Slope	Intercept / ppb h^{-1}	χ^2/DOF	R^2	N
			CO			
1	17.06.2011	1.22±0.10	0.79±0.37	0.75	0.59	93
2	09.08.2011	1.35±0.09	0.11±0.25	1.11	0.87	38
		0.95±0.09	**0.26±0.26**	**0.59**	**0.80**	**38**
			Benzene			
3	07.06.2010	1.56±0.04	-0.14±0.26	1.04	0.74	137
4	23.06.2010	1.32±0.04	-0.58±0.26	1.71	0.56	148
5	01.08.2011	1.55±0.05	-0.08±0.22	0.79	0.85	58
		1.44±0.07	**0.05±0.30**	**0.49**	**0.78**	**58**
6*	08.06.2010	1.09±0.02	0.25±0.14	1.69	0.93	157
7*	25.06.2010	1.14±0.03	0.27±0.43	4.56	0.66	108
			Toluene			
8	05.07.2010	1.64±0.03	-0.03±0.15	1.31	0.82	129
9	04.08.2011	1.69±0.12	0.13±0.45	1.02	0.69	66
		1.35±0.12	**0.06±0.45**	**0.76**	**0.62**	**66**
10*	13.06.2010	1.14±0.04	-0.04±0.37	1.89	0.90	114
			***p*-Xylene**			
11	14.06.2010	1.45±0.04	-0.25±0.22	1.52	0.62	99
12	02.07.2010	1.48±0.05	-0.26±0.29	1.45	0.66	106
13	07.08.2011	1.32±0.10	-0.05±0.31	0.89	0.62	29
		1.24±0.10	**0.03±0.29**	**0.68**	**0.37**	**29**
14*	16.06.2010	1.32±0.04	0.13±0.43	2.40	0.83	77
15*	30.06.2010	1.26±0.04	0.51±0.44	4.05	0.60	87
			1,3,5-TMB			
16	17.06.2010	1.32±0.05	-0.26±0.19	0.86	0.80	91
17	01.07.2010	1.23±0.03	0.28±15	0.98	0.81	76
18	10.08.2011	1.34±0.06	0.02±0.18	0.87	0.63	51
		1.09±0.05	**0.04±0.15**	**0.65**	**0.57**	**51**
19*	21.06.2010	1.19±0.03	0.41±0.20	1.50	0.92	107
20*	28.06.2010	1.09±0.04	-0.03±0.46	1.50	0.96	26

* High NO_x experiment.

CO photo-oxidation experiments are regarded as a reference because all known OH production and destruction terms for the calculation of turnover rates are considered in eqs. 5.5 and 5.6. D_{OH} is expected to be balanced by an equally large value of P_{OH}. Two individual SAPHIR experiments are dedicated to the investigation of OH budgets during the photo-oxidation of CO under low NO_x conditions. Slopes for D_{OH} vs. P_{OH} scatter around unity with a range of 0.95±0.09 (09.08.2011, using OH-DOAS data) to 1.35±0.09 (09.08.2011, using OH-LIF data). These results confirm that the OH budget is closed during CO photo-oxidation experiments in SAPHIR and that eqs. 5.5 and 5.6 account for all important OH sources and sinks. Moreover, it is concluded that an error of about 30% should be considered as accuracy for the determination of OH turnover rates. This accuracy can be rationalized by the combined uncertainties of all measured quantities needed for the data analysis (see table 5.4 for the performance of the key instruments).

In addition to the OH measurements by LIF, the DOAS instrument, which is regarded as a calibration-free reference standard, is used to check for the possible influence of systematic errors. Simultaneous OH measurements by DOAS and LIF in 2011 during SAPHIR experiments with aromatics revealed good agreement between both detection techniques.[141] Only in the presence of toluene the OH-LIF data were found to be greater by 30% − 40% compared to the OH-DOAS data. To date the reason for this is unclear and further characterization experiments are required. In general it is expected that the analysis of the OH budget yields comparable results regardless of how D_{OH} is calculated (either by using OH-DOAS or OH-LIF data). For five experiments presented here (01.08., 04.08., 07.08., 09.08., and 10.08.2011) simultaneous OH measurements by DOAS and LIF are available. The regression analysis of D_{OH} vs. P_{OH} for the benzene experiment on 01.08. and the *p*-xylene experiment on 07.08. indeed give similar results when OH-DOAS and OH-LIF data are used (see figs. 5.20 and 5.21). However, minor discrepancies are observed for the toluene experiment on 04.08., the CO experiment on 09.08., and the 1,3,5-TMB experiment on 10.08. where the regression analysis yields slightly greater slopes ($\approx 30\%$) by using the OH-LIF data (see fig. 5.21). In contrast, the fitted intercepts for these three experiments are not significantly different when OH-DOAS and OH-LIF data are used. At least part of the discrepancy in the case of the toluene experiment on 04.08. can possibly be attributed to artifacts of the OH-LIF measurement as mentioned above. The actual reason for the observed mismatch remains unclear but is well within the overall accuracy for the determination of OH turnover rates.

In all SAPHIR experiments with benzene, toluene, *p*-xylene, and 1,3,5-TMB slopes for D_{OH} vs. P_{OH} are found to be within the range of $1.1 - 1.6$, $1.1 - 1.7$, $1.2 - 1.5$, and $1.1 - 1.3$, respectively. The fitted slopes in

the presence of aromatic hydrocarbons always slightly exceed unity with no clear trend for the homologous series of aromatics. Nonetheless, these results indicate that the OH budget during photo-oxidation experiments with aromatics is reasonably balanced within the accuracy for the determination of OH turnover rates.

5.4 Discussion

Despite MCM's tendency to underpredict radical concentrations, the model-independent OH budget analysis shows that OH destruction and production rates are very similar for all investigated aromatics. However, the results leave some scope for OH producing pathways that are not considered in the calculation of P_{OH} (see eq. 5.5). These aspects are discussed in section 5.4.1. Moreover, the following sections deal with model-dependent aspects of the data analysis. Uncertainties introduced by the SAPHIR auxiliary model are discussed in section 5.4.2 and differences observed for the individual aromatic compounds are highlighted in sections 5.4.3 and 5.4.4.

5.4.1 Model-independent investigation of OH budgets

OH turnover rates, exclusively calculated from measured quantities, were previously consulted for the analysis of OH budgets during field campaigns by comparing diurnal profiles of D_{OH} and P_{OH}.[72,82,151,152] In contrast to the comparison of diurnal profiles, the correlation and regression analysis facilitates a quantitative evaluation of OH budgets considering errors in both quantities (D_{OH} and P_{OH}).

In SAPHIR experiments with aromatics, D_{OH} is found to exceed P_{OH} by approximately 40% in the case of benzene and toluene and by 20% and 10% in the case of *p*-xylene and 1,3,5-TMB, respectively (table 5.5, using OH-DOAS data). At least for the photo-oxidation of benzene and toluene, the results are consistent with additional OH production processes like recycling via radical-radical reactions. Conventionally, $HO_2 + RO_2$ reactions are considered to be radical terminating reactions yielding hydroperoxides. Such hydroperoxides are again photolysed to radicals and therefore act as temporary radical reservoir. In contrast to this conventional reaction sequence, previous laboratory studies[153–155] confirmed the OH propagating reaction HO_2 + CH_3CO_3 (acetyl peroxy radical). CH_3CO_3, originating from OH + methylglyoxal, is also involved in aromatic photo-oxidation systems (except for benzene). As already outlined in section 2.2, such a recycling of radicals was also postulated for the HO_2 + $biRO_2$ reaction.[33,49]

Experiments performed under high NO_x conditions are consulted to check for the possible contribution of radical-radical reactions to P_{OH}. During these experiments the fate of organic peroxy radicals is expected to be governed by the reaction with NO and the potential OH recycling via reactions like $HO_2 + RO_2$ as well as the formation of hydroperoxides acting as photolytical OH precursor should be of vanishing importance resulting in slopes for D_{OH} vs. P_{OH} approaching unity. Indeed slopes of 1.1 obtained during two high NO_x experiments with benzene and a single high NO_x experiment with toluene are somewhat smaller compared to their corresponding values determined for low NO_x experiments. This supports the assumption of a OH recycling pathway via radical-radical reactions. By comparing the results of the low NO_x experiments (using OH-DOAS data) with benzene (01.08.2011) and toluene (04.08.2011) to their corresponding high NO_x experiments, up to 30% of P_{OH} might proceed via radical-radical reactions when the chemistry is not driven by NO. However, considering the limited number of experiments and the uncertainties for the determination of OH turnover rates ($\approx 30\%$), this is merely taken as a qualitative hint. The situation is somewhat different in the case of the high NO_x experiments with *p*-xylene and 1,3,5-TMB where the slopes for D_{OH} vs. P_{OH} are found to be very similar to those obtained for the corresponding low NO_x experiments. Consequently, for these compounds there is no evidence for increased OH recycling.

5.4.2 Impact of SAPHIR specific processes

To assess the maximum influence of the chamber auxiliary mechanism, photo-oxidation experiments with aromatics are also simulated without reactions R20, R21, and R22 (scenario S(0)) and model-measurement comparisons are shown in fig. 5.23 for the 1,3,5-TMB experiment performed on 10.08.2011. The only constraints for these model runs are the measured HNO_2 concentration, relative humidity, temperature, pressure, photolysis frequencies, and the replenishment flow. The chamber auxiliary mechanism significantly impacts the model-measurement comparisons during zero air periods where the consumption of OH is dominated by the auxiliary reaction R20. By omitting this reaction, OH is strongly overpredicted whereas HO_2 and RO_2 are underestimated. On the other hand, model-measurement comparisons are hardly affected during photo-oxidation periods where the consumption of OH is dominated by reaction with the aromatic hydrocarbon. Therefore, the influence of the auxiliary reaction R20 is of minor importance for the evaluation of photo-oxidation experiments with aromatics. For the OH reactivity, scenario S(0) results in a diurnal profile that is lower by the constant contribution of k_{OH}^{BG} compared to the scenario $S_a(0)$. Further, the implemen-

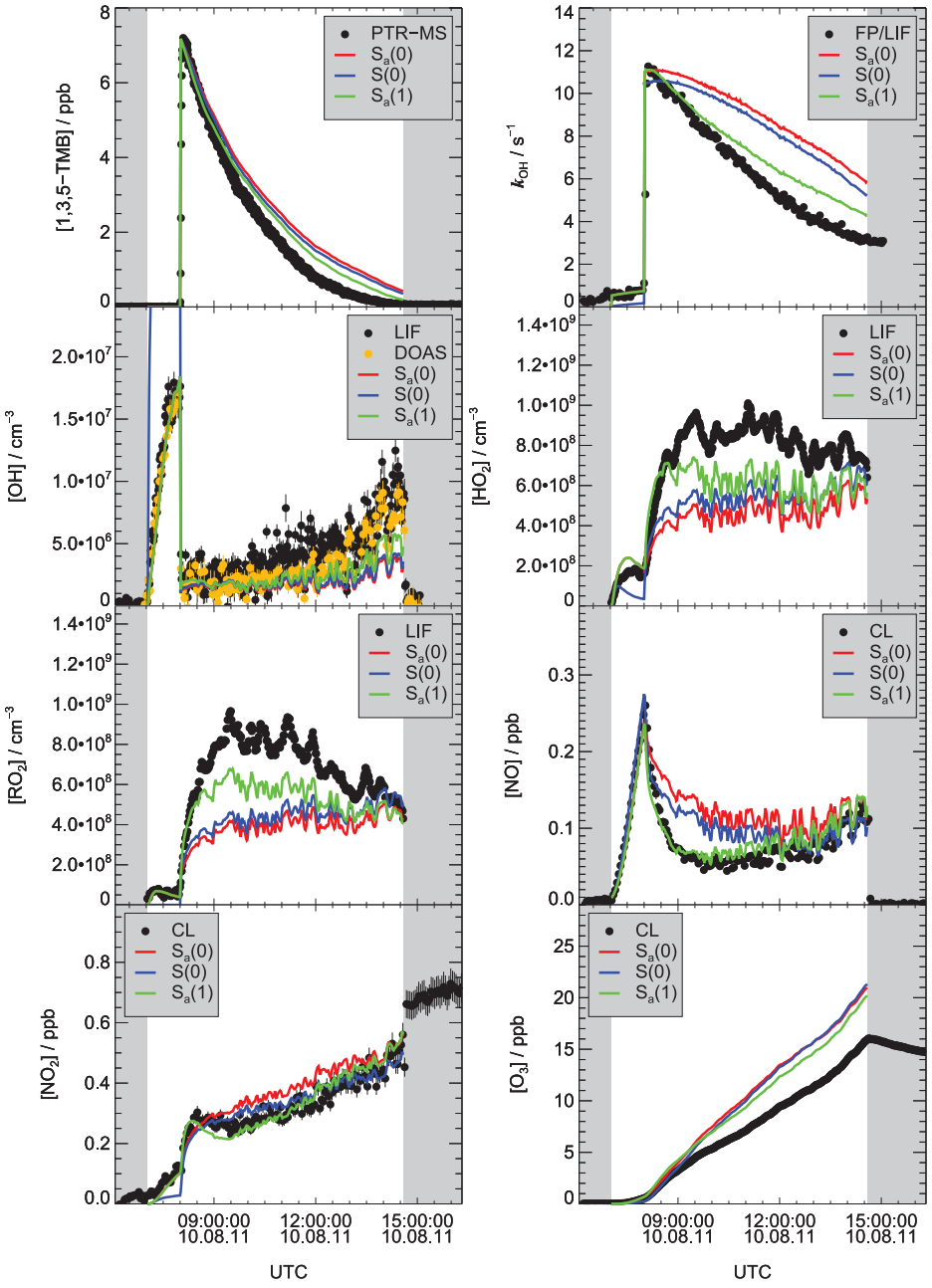

Figure 5.23: Model-measurement comparisons for a SAPHIR experiment with 1,3,5-TMB performed on 10.08.2011. Black and yellow symbols represent measurements. Solid lines show MCMv3.2 model simulations for the base case scenario with ($S_a(0)$, red) and without (S(0), blue) chamber auxiliary mechanism as well as the tuned scenario $S_a(1)$ that also incorporates the auxiliary chamber model (green). The concentration of 1,3,5-TMB measured by PTR-MS is scaled to match the initial increase of k_{OH} (see section 5.3.3 for details).

tation of the auxiliary chamber mechanism does not significantly change the model-measurement comparison for O_3 in aromatic photo-oxidation systems. Thus, the overestimation of O_3 concentrations, observed for most of the experiments with aromatics, cannot be attributed to uncertainties arising from the chamber auxiliary reactions. In summary, the numerical simulations are found to exhibit little sensitivity to the auxiliary mechanism and the chamber specific processes do not account significantly for the observed discrepancies between $S_a(0)$ and the measurements.

5.4.3 Comparison of phenol yields to literature values

Phenolic compound yields determined in this work are generally in line with the MCMv3.2 recommendations given by Bloss et al.[28]. The phenol yield from benzene photo-oxidation of $\phi_{\text{phenol}}^{\text{benzene}} = 0.55 \pm 0.10$ is in excellent agreement with a phenol yield of 0.53±0.07 obtained in chamber experiments by Volkamer et al.[25]. In a recent chamber study by Nakao et al.[145] a slightly lower phenol yield of 0.4 was determined. Berndt and Böge[46], Noda et al.[32], and Birdsall and Elrod[49] performed flow-tube studies and consistently reported phenol yields in the range of 0.5-0.6 (see section 4.3.1 for details).

The cresol yield of $\phi_{\text{cresol}}^{\text{toluene}} = 0.17 \pm 0.05$ is in accordance with yields of 0.18±0.03 and 0.23 determined in chamber studies by Klotz et al.[97] and Nakao et al.[145], respectively. Noda et al.[32], Baltaretu et al.[47], and Birdsall et al.[33] performed flow-tube studies under near-atmospheric conditions and reported cresol yields in the range of 0.2-0.3 (see section 4.3.2 for details).

The dimethylphenol yield of $\phi_{\text{dimethylphenol}}^{p-\text{xylene}} = 0.05 \pm 0.03$ is somewhat lower compared to the MCMv3.2 recommendation[28] of 0.12±0.03 based on chamber experiments reported by Volkamer.[108] A dimethylphenol yield in the range of 0.1-0.2 was consistently reported in a number of studies[32,45,49,53,59] (see section 4.3.3 for details). The slightly deviating value found in this work might be subject to unaccounted systematic errors possibly originating from the PTR-MS calibration procedure.

$\phi_{\text{trimethylphenol}}^{1,3,5-\text{TMB}} < 0.05$ determined in a SAPHIR experiment with 1,3,5-TMB is also in line with yields of 0.07, 0.04, and 0.03 determined in a previous chamber study by Volkamer[108] and in laboratory experiments by Smith et al.[45] and Birdsall and Elrod[49], respectively (see section 4.3.4 for details).

5.4.4 Evaluation of MCMv3.2 degradation schemes

For all SAPHIR experiments, the measured diurnal profiles of k_{OH} are overpredicted by the MCMv3.2 base case simulations ($S_a(0)$) whereas OH concentrations are underestimated. In the case of benzene, toluene, and *p*-

xylene, sensitivity studies show that the overprediction of k_{OH} cannot account for the underestimation of OH concentrations. Only for 1,3,5-TMB, improved model-measurement comparisons for OH are achieved at reduced k_{OH} (fig. 5.10, panel (c)). Possible reasons for the OH mismatch are unaccounted OH sources. However, it is shown by sensitivity studies that the implementation of the recently postulated radical recycling pathway via the HO_2 + $biRO_2$ reaction[33,49] has no significant impact on the simulated OH concentrations (fig. 5.9, panel (c)). Observed model-measurement discrepancies for hydroxyl radicals coincide with the underestimation of HO_2 and RO_2 (table 5.3). Therefore it is concluded that the underestimation of OH concentrations relates to mechanistic shortcomings concerning HO_2 and RO_2 production processes.

In photo-oxidation systems, the production of peroxy radicals leads to conversion of NO to NO_2. Accordingly, an underprediction of peroxy radical concentrations is expected to result in an overprediction of NO. This is indeed observed during most SAPHIR experiments (table 5.3). The largest discrepancies between MCMv3.2 base case simulations and measured NO profiles are found for toluene and 1,3,5-TMB. Examples are given in figs. 5.13 and 5.17 where NO is found to decay more rapidly than predicted by the model $S_a(0)$ just after the injection of the aromatic. A better simulation for NO can be achieved by an increase of peroxy radical concentrations. The resulting increase of NO to NO_2 conversion then also causes an elevated O_3 production. Most of the base case MCMv3.2 simulations already overestimate O_3 and therefore the combination of underestimated peroxy radical concentrations and overestimated NO concentrations represents a challenging task regarding the construction of an improved reaction mechanism. O_3 production from the photo-oxidation of aromatics is influenced by the efficiency of individual reaction channels in converting NO to NO_2 and further by conversion of reactive nitrogen oxides to reservoir species like PAN and its derivatives.[29] On the basis of these considerations, the tuned model scenario $S_a(1)$ is constructed. $S_a(1)$ enhances the formation of peroxy radicals by means of lower bicyclic nitrates yields from NO + $biRO_2$ (fig. 5.6, panels (d) and (e)) and by radical recycling via HO_2 + $biRO_2$ (fig. 5.9, panels (d) and (e)). These changes of MCMv3.2 are based on experimental results of flow-tube studies by Birdsall et al. and Elrod.[33,49,57] To counteract a further overprediction of O_3 concentrations, $S_a(1)$ resorts to an enhanced formation of NO_x reservoirs by assuming γ-DC yields of unity originating from ring fragmentation (fig. 5.8, panel (h)). γ-DCs are more efficient at generating PAN derivatives compared to furanones that are also considered to originate from ring scission but have not been quantified so far.[28,56,62] By setting γ-DC yields to 100%, the formation of furanones in the model is not completely suppressed

because MCMv3.2 also considers a photolytical furanone source.[64] $S_a(1)$ further assumes lower rate constants for OH + bicyclic compounds to reflect the tendency to lower values for OH rate constants of chemically similar cyclic alkenes.[149] This approach prolongs the simulated lifetimes of bicyclic nitrates and therefore has the potential to counteract the overprediction of O_3 (fig. 5.10, panel (h)).

The tuned model scenario $S_a(1)$ improves the performance of MCMv3.2 with respect to the formation of peroxy radicals and regarding the diurnal profiles of NO_x and k_{OH} for all experiments. However, major discrepancies still remain regarding the underestimation of OH, HO_2, and RO_2. Significant differences between low and high NO_x experiments are observed for *p*-xylene and 1,3,5-TMB (table 5.3). During high NO_x experiments with these compounds, numerical simulations using both scenarios, $S_a(0)$ and $S_a(1)$, are in fair agreement with measured O_3 concentrations. For all other experiments the O_3 concentrations are strongly overestimated. Additional sensitivity studies (not presented here) were performed to investigate the origin of MCM's tendency to overpredict O_3. MCMv3.2 considers chemical ozone losses proceeding via O_3 + unsaturated compounds. The simulated O_3 concentrations exhibit little sensitivity to these loss processes and uncertainties of the corresponding rate constants cannot account for the O_3 mismatch. O_3 uptake on aerosol particles would also explain the model-measurement discrepancies but is estimated unimportant (assuming uptake coefficients on the order of 1×10^{-4}).[156] The reason for the observed overestimation remains unclear but most likely results from shortcomings of the mechanistic representation of ring fragmentation channels that are most efficient at generating O_3.[29]

Similar results were reported by Wagner et al.[29] and Bloss et al.[27,28] who performed chamber experiments with a series of aromatic compounds in the presence of up to 400 ppb of NO and more recently by Metzger et al.[157] and Rickard et al.[56] who performed chamber experiments to investigate SOA formation from 1,3,5-TMB. Numerical simulations based on MCMv3.1 were used for the evaluation of these previous studies. Aromatic photo-oxidation mechanisms have not explicitly been updated in MCMv3.2 and therefore the previous results are comparable to those presented in the work at hand. This point was further verified by model test runs comparing the MCM versions 3.1 and 3.2. Bloss et al. found that the simulated OH concentrations were not sufficient to reproduce the observed aromatic hydrocarbon decay rates. They also reported that simulated NO to NO_2 conversion rates underpredict the observed values. It was further stated that MCM tends to overestimate the O_3 concentration in aromatic photo-oxidation systems.[29] Bloss and co-workers concluded that the observed discrepancies indicate mechanistic

shortcomings regarding the HO_x production processes and NO to NO_2 conversion by peroxy radicals.[27] The more recent studies by Metzger et al. and Rickard et al. are qualitatively in line with the Bloss results. Additional experimental information was provided by Rickard et al. who performed peroxy radical measurements by means of a peroxy radical chemical amplifier (PERCA). Peroxy radical concentrations were found to be underestimated by MCM.[56] The results of this work are in agreement with the results of previous chamber studies and provide a deeper insight into the origins of the MCM shortcomings: (i) The underprediction of OH concentrations most likely results from a considerable underestimation of peroxy radicals. (ii) Unaccounted OH recycling processes cannot be excluded. However, the simulated OH concentrations exhibit little sensitivity to the recently postulated radical recycling proceeding via HO_2 + $biRO_2$.[33,49] (iii) MCMv3.2 overestimates the OH reactivity for all aromatic photo-oxidation systems. Only in the case of 1,3,5-TMB, part of the OH underestimation results from the overestimation of k_{OH}.

6

Summary and conclusions

This work was focused on the investigation of OH-initiated atmospheric degradation mechanisms of aromatic hydrocarbons by means of pulsed kinetic laboratory experiments and outdoor simulation chamber studies. The key instrument deployed in both experimental approaches was the OH reactivity instrument based on the FP/LIF technique originally designed for the measurement of pseudo-first-order OH loss rate constants, k_{OH}, in ambient air.

For the pulsed kinetic studies, the OH reactivity instrument was extended to the detection of HO_2 radicals (HO_x measurement mode). In characterization experiments it was found that the LIF detection technique for HO_2 exhibits cross-sensitivity to specific RO_2 radicals. This RO_2 interference also affects ambient HO_2 measurements and the findings of this work initiated extensive studies to investigate potential interferences for a number of VOCs and, moreover, a re-evaluation of HO_2 data obtained during recent field campaigns. The extended OH reactivity instrument facilitates the alternating detection of OH and HO_x decay curves. Prompt HO_2 yields following the OH + aromatic hydrocarbon reactions were determined with reference to CO experiments by applying analytical solutions and curve fitting procedures. The prompt HO_2 yields determined in this work were compared to complementary results of previous product studies and confirm the currently proposed aromatic degradation mechanisms regarding the initial reaction steps. The postulated HO_2 co-products, as implemented in MCMv3.2, are phenols and epoxides. Formation yields of phenols were reported in a large number of studies whereas only few studies reported the formation of epoxides. Taking into account phenol yields reported in literature, the prompt HO_2 yields determined in this work help to set upper limits for the formation yields of epoxides. In future work, the pulsed kinetic approach will be extended for further substance classes (e.g. biogenic VOCs like terpenes) to check if

prompt HO_2 formation is also operative in other chemical systems.

The simulation chamber studies present an integrated approach for the evaluation of aromatic degradation schemes of MCMv3.2 against SAPHIR data. Numerical model simulations exhibit poor performance for the description of radical production, the NO to NO_2 conversion and O_3 formation. For example, MCMv3.2 was found to underpredict OH concentrations and to overpredict O_3. These tendencies have already been observed in previous chamber experiments with aromatics. The model performance for selected target quantities was analysed as a function of common key parameters of the aromatic degradation schemes to investigate the origins of the MCMv3.2 shortcomings. These sensitivity studies suggest that an overall improved model performance is achieved by: (i) reducing yields of bicyclic nitrates from $biRO_2$ + NO, (ii) suppressing the formation of furanones from ring fragmentation, (iii) considering radical recycling via $biRO_2$ + HO_2, and (iv) by reducing OH rate constants of bicyclic compounds. Based on the results of the sensitivity studies, an improved reaction mechanism was constructed but a perfect agreement with the measurements was not achieved. To further clarify the reasons for the mechanistic shortcomings, a model-independent OH budget analysis was performed for all aromatic photo-oxidation systems. For this analysis, OH production and destruction rates were calculated exclusively from measured quantities. OH destruction rates are assumed to be well-defined because they are calculated based on the measured OH reactivity k_{OH} that accounts for all chemical OH losses. Therefore, this evaluation procedure can help to check if all OH production processes are considered in the calculation of OH production rates. In a steady-state assumption for OH, its production rate should be balanced by an equally large destruction rate. This was the case for all aromatics. However, additional, so far unknown, OH production processes are possible considering the uncertainties for the determination of OH turnover rates. In the recent literature, OH recycling via radical-radical reactions was postulated. In this study, numerical simulations showed that these reaction pathways cannot account for the observed underestimation of OH in chamber experiments. The OH mismatch in aromatic photo-oxidation systems most likely originates from the underprediction of peroxy radical concentrations. Ring fragmentation channels are most efficient at generating peroxy radicals. Therefore, future SAPHIR campaigns should be dedicated to the investigation of the atmospheric chemistry of ring fragmentation products like dicarbonyls and furanones. Another promising approach is the investigation of phenolic compound degradation mechanisms in individual chamber experiments. This is especially of importance for phenol because it is a major oxidation product ($\approx 50\%$) of the benzene oxidation. SAPHIR experiments with phenol have already been per-

formed within the scope of this work and the evaluation is still in progress. In the future, another procedure for the evaluation of photo-oxidation models against SAPHIR data will be tested. By defining an objective function on the basis of selected target quantities, a global optimum for the model performance could be obtained by applying fitting procedures. However, such an approach is computationally expensive and the utility might be limited.

Appendix A

RO_2 radicals involved in the photo-oxidation of aromatics

A compilation of organic peroxy radicals stemming from benzene, toluene, *p*-xylene, and 1,3,5-TMB is given in table A.1. The list is based on MCMv3.2 degradation schemes and is restricted to RO_2 that are considered to be detectable by LIF. RO_2 presented here undergo reactions with NO to give RO with formation yields of c_{RO}. These RO again form HO_2 with yields of c_{HO_2} in subsequent reactions with O_2. For all SAPHIR experiments with aromatics, the simulated RO_2 concentrations consulted for comparison with measurements correspond to the sum of organic peroxy radicals listed in table A.1. Moreover, these RO_2 are considered to contribute to LIF HO_2 measurement interferences. HO_2 and RO_2 concentrations measured by LIF during SAPHIR experiments are therefore corrected for the RO_2 cross-sensitivity according to eqs. 5.1 and 5.2 based on the sum of simulated concentrations of the individual RO_2 species. Their relative detection sensitivities are assumed to be equal to the RO_2 detection sensitivity determined in experiments with benzene.[81] Values of $\alpha_{RO_2}^{benzene} = 0.86$ (for experiments in 2010) and $\alpha_{RO_2}^{benzene} = 0.17$ (for experiments in 2011) are applied. Further, the factors c_{RO} and c_{HO_2} are used to account for individual chemical properties of the different RO_2 species.

Table A.1: Organic peroxy radicals (MCM specific designation) detectable by LIF and their respective RO yields (c_{RO}) in RO_2 + NO reactions and subsequent HO_2 yields (c_{HO_2}) in RO + O_2 reactions as implemented in MCMv3.2.

RO_2	Stemming from the photo-oxidation of				c_{RO}	c_{HO_2}
	Benzene	Toluene	*p*-Xylene	1,3,5-TMB		
BZBIPERO2	×				0.92	1.00
BZEMUCO2	×				0.90	0.50
C5DIALO2	×				1.00	1.00
PHENO2	×				1.00	1.00
HCOCO3	×	×	×	×	1.00	1.00
HOCH2CO3	×	×	×	×	1.00	1.00
MALDIALCO3	×	×			1.00	1.00
C3DIALO2	×	×			1.00	1.00
MALDIALO2	×	×			1.00	1.00
NBZFUO2	×	×			1.00	0.50
BZFUO2	×	×			1.00	1.00
HCOCOHCO3	×	×	×		1.00	1.00
NCATECO2	×				1.00	1.00
C5CO2OHCO3	×				1.00	1.00
C4CO2DBCO3	×				1.00	1.00
C6H5CH2O2		×			0.90	1.00
TLBIPERO2		×			0.89	1.00
CRESO2		×			1.00	1.00
TLEMUCO2		×			0.90	0.50
C615CO2O2		×			1.00	1.00
C5CO14O2		×	×		1.00	0.17
C3MCODBCO3		×	×		1.00	1.00
MC3CODBCO3		×	×		1.00	0.65
C4M2ALOHO2		×	×		1.00	1.00
C5DICARBO2		×			1.00	1.00
TLFUO2		×			1.00	1.00
MNCATECO2		×			1.00	1.00
PXYFUO2		×			1.00	1.00
CO2H3CO3		×	×	×	1.00	1.00
C6CO2OHCO3		×			1.00	1.00
PXYLO2			×		0.90	1.00
PXYBIPERO2			×		0.86	1.00
PXYMUCO2			×		0.83	0.50
C6M5CO2O2			×		1.00	1.00
PXYOLO2			×		1.00	1.00
C3MDIALO2			×	×	1.00	1.00
DMKOHO2			×		1.00	0.30
PXYFUO2			×		1.00	1.00
C4CO2O2			×		1.00	0.50
CHOMOHCO3			×	×	1.00	1.00
PXNCATECO2			×		1.00	1.00
TL4OHNO2O2			×		1.00	1.00
C6MOHCOCO3			×		1.00	1.00
C5DBCO2CO3			×		1.00	1.00
TMBO2				×	0.90	1.00
TM135BPRO2				×	0.84	1.00
TM135OLO2				×	1.00	1.00
TM135MUCO2				×	0.94	0.50
C5MCO2OHO2				×	1.00	1.00
MXYFUO2				×	1.00	1.00
C4COMOHCO3				×	1.00	1.00

Appendix B

OH rate constants of bicyclic compounds

The photo-oxidation mechanisms of MCMv3.2 consider the formation of O_2-bridged bicyclic species originating from reactions of the bicyclic peroxy radical $biRO_2$ (fig. 2.2). Such compounds are bicyclic hydroperoxides from $biRO_2$ + HO_2 reactions, bicyclic ketones and diols from $biRO_2$ + RO_2 reactions, and bicyclic nitrates from $biRO_2$ + NO reactions. MCMv3.2 assumes both bicyclic compounds derived from the parent aromatic hydrocarbon and bicyclic compounds derived from primary phenolic oxidation products. The degradation of these compounds is considered to proceed via photolysis (using photolysis frequencies of methylhydroperoxide, 2-butanone, and isopropyl nitrate as proxies) and via fast reactions with OH. The corresponding OH rate constants of all O_2-bridged bicyclic hydroperoxides, ketones, diols, and nitrates originating from the photo-oxidation of benzene, toluene, *p*-xylene, and 1,3,5-TMB are listed in table B.1.

Table B.1: OH rate constants of bicyclic compounds (hydroperoxides, ketones, diols, nitrates) involved in the photo-oxidation of aromatics as incorporated in MCMv3.2. Compounds are termed with their MCM specific designation.

Compound	Chemical identity	$k_{\mathrm{OH+bicyclic}}$ / $10^{-11}\mathrm{cm^3s^{-1}}$
	Benzene	
BZBIPEROOH	Hydroperoxide	9.77
PHENOOH	Hydroperoxide	11.60
NPHENOOH	Hydroperoxide	10.70
BZOBIPEROH	Ketone	8.16
BZBIPER2OH	Diol	12.10
PHENOH	Diol	11.30
NPHENOH	Diol	10.40
BZBIPERNO3	Nitrate	7.30
	Toluene	
TLBIPEROOH	Hydroperoxide	9.64
CRESOOH	Hydroperoxide	11.50
NCRESOOH	Hydroperoxide	10.70
TLOBIPEROH	Ketone	7.99
TLBIPER2OH	Diol	12.00
CRESOH	Diol	11.10
NCRESOH	Diol	10.40
TLBIPERNO3	Nitrate	7.16
	***p*-Xylene**	
PXYBPEROOH	Hydroperoxide	7.65
PXYOLOOH	Hydroperoxide	15.10
NPXYOLOOH	Hydroperoxide	14.30
TLOBIPEROH	Ketone	7.99
PXYBPER2OH	Diol	11.20
PXYOLOH	Diol	11.10
NPXYOLOH	Diol	14.00
PXYBIPENO3	Nitrate	7.16
	1,3,5-TMB	
TM135BPOOH	Hydroperoxide	12.80
TM135OLOOH	Hydroperoxide	15.00
NTM135LOOH	Hydroperoxide	14.40
TM135OBPOH	Ketone	10.00
TM135BP2OH	Diol	12.80
TM135OLOH	Diol	14.70
NTM135OLOH	Diol	14.00
TM135BPNO3	Nitrate	9.45

Bibliography

[1] S. D. Piccot, J. J. Watson and J. W. Jones, *Journal of Geophysical research-Atmospheres*, 1992, **97**, 9897–9912.

[2] A. Guenther, C. N. Hewitt, D. Erickson, R. Fall, C. Geron, T. Graedel, P. Harley, L. Klinger, M. Lerdau, W. A. McKay, T. Pierce, B. Scholes, R. Steinberger, R. Tallamraju, J. Taylor and P. Zimmermann, *Journal of Geophysical Research-Atmospheres*, 1995, **100**, 8873–8892.

[3] R. Koppmann, *Volatile organic compounds in the atmosphere*, Blackwell Publishing Ltd, 2007.

[4] D. H. Ehhalt, *Physical Chemistry Chemical Physics*, 1999, **1**, 5401–5408.

[5] B. J. Finlayson-Pitts and J. Pitts, *Chemistry of the upper and lower atmosphere: Theory, experiments, and applications*, Academic Press, 2000.

[6] Y. Elshorbany, I. Barnes, K.-H. Becker, J. Kleffmann and P. Wiesen, *Zeitschrift für Physikalische Chemie*, 2010, **224**, 967–987.

[7] M. Hallquist, J. C. Wenger, U. Baltensperger, Y. Rudich, D. Simpson, M. Claeys, J. Dommen, N. M. Donahue, C. George, A. H. Goldstein, J. F. Hamilton, H. Herrmann, T. Hoffmann, Y. Iinuma, M. Jang, M. E. Jenkin, J. L. Jimenez, A. Kiendler-Scharr, W. Maenhaut, G. McFiggans, T. F. Mentel, A. Monod, A. S. H. Prevot, J. H. Seinfeld, J. D. Surratt, R. Szmigielski and J. Wildt, *Atmospheric Chemistry and Physics*, 2009, **9**, 5155–5236.

[8] WHO, *Air quality guidelines for Europe*, World Health Organisation, Regional office for Europe, 2000.

[9] J. L. Mauderly and J. C. Chow, *Inhalation Toxicology*, 2008, **20**, 257–288.

[10] Intergovernmental Panel on Climate Change (IPCC), *Climate Change 2007: The Physical Science Basis*, Cambridge University Press, UK, 2007.

[11] A. Patyk and U. Höpfner, *Differentiation of the components of motor vehicle hydrocarbon emissions, Research report UBA-FB–96-007/1*, German Federal Environmental Agency, 1995.

[12] R. Kurtenbach, R. Ackermann, K.-H. Becker, A. Geyer, J. A. G. Gomes, J. C. Lorzer, U. Platt and P. Wiesen, *Journal of Atmospheric Chemistry*, 2002, **42**, 395–411.

[13] A. Niedojadlo, K.-H. Becker, R. Kurtenbach and P. Wiesen, *Atmospheric Environment*, 2007, **41**, 7108–7126.

[14] J. G. Calvert, R. Atkinson, K.-H. Becker, R. M. Kamens, J. H. Seinfeld, T. J. Wallington and G. Yarwood, *Mechanisms of atmospheric oxidation of aromatic hydrocarbons*, Oxford University Press, 2002.

[15] T. J. Fortin, B. J. Howard, D. D. Parrish, P. D. Goldan, W. C. Kuster, E. L. Atlas and R. A. Harley, *Environmental Science & Technology*, 2005, **39**, 1403–1408.

[16] M. M. Johnson, R. Williams, Z. Fan, L. Lin, E. Hudgens, J. Gallagher, A. Vette, L. Neas and H. Ozkaynak, *Atmospheric Environment*, 2010, **44**, 4927–4936.

[17] S. Hawthorne, D. Miller, R. Barkley and M. Krieger, *Environmental Science & Technology*, 1988, **22**, 1191–1196.

[18] S. Hawthorne, D. Miller, J. Langenfeld and M. Krieger, *Environmental Science & Technology*, 1992, **26**, 2251–2262.

[19] A. R. Ravishankara, S. Wagner, S. Fischer, G. Smith, R. Schiff, R. T. Watson, G. Tesi and D. D. Davis, *International Journal of Chemical Kinetics*, 1978, **10**, 783–804.

[20] C. Warneke, J. A. de Gouw, P. D. Goldan, W. C. Kuster, E. J. Williams, B. M. Lerner, R. Jakoubek, S. S. Brown, M. Stark, H Aldener, A. R. Ravishankara, J. M. Roberts, M. Marchewka, S. Bertman, D. T. Sueper, S. A. McKeen, J. F. Meagher and F. C. Fehsenfeld, *Journal of Geophysical Research - Atmospheres*, 2004, **109**, D10309.

[21] M. E. Jenkin, S. M. Saunders and M. J. Pilling, *Atmospheric Environment*, 1997, **31**, 81–104.

[22] S. M. Saunders, M. E. Jenkin, R. G. Derwent and M. J. Pilling, *Atmospheric Chemistry and Physics*, 2003, **3**, 161–180.

[23] M. E. Jenkin, S. M. Saunders, V. Wagner and M. J. Pilling, *Atmospheric Chemistry and Physics*, 2003, **3**, 181–193.

[24] R. Volkamer, U. Platt and K. Wirtz, *Journal of Physical Chemistry A*, 2001, **105**, 7865–7874.

[25] R. Volkamer, B. Klotz, I. Barnes, T. Imamura, K. Wirtz, N. Washida, K.-H. Becker and U. Platt, *Physical Chemistry Chemical Physics*, 2002, **4**, 1598–1610.

[26] B. Klotz, R. Volkamer, M. D. Hurley, M. P. S. Andersen, O. J. Nielsen, I. Barnes, T. Imamura, K. Wirtz, K.-H. Becker, U. Platt, T. J. Wallington and N. Washida, *Physical Chemistry Chemical Physics*, 2002, **4**, 4399–4411.

[27] C. Bloss, V. Wagner, A. Bonzanini, M. E. Jenkin, K. Wirtz, M. Martin-Reviejo and M. J. Pilling, *Atmospheric Chemistry and Physics*, 2005, **5**, 623–639.

[28] C. Bloss, V. Wagner, M. E. Jenkin, R. Volkamer, W. J. Bloss, J. D. Lee, D. E. Heard, K. Wirtz, M. Martin-Reviejo, G. Rea, J. C. Wenger and M. J. Pilling, *Atmospheric Chemistry and Physics*, 2005, **5**, 641–664.

[29] V. Wagner, M. E. Jenkin, S. M. Saunders, J. Stanton, K. Wirtz and M. J. Pilling, *Atmospheric Chemistry and Physics*, 2003, **3**, 89–106.

[30] A. K. Mollner, S. Valluvadasan, L. Feng, M. K. Sprague, M. Okumura, D. B. Milligan, W. J. Bloss, S. P. Sander, P. T. Martien, R. A. Harley, A. B. McCoy and W. P. L. Carter, *Science*, 2010, **330**, 646–649.

[31] R. Atkinson and J. Arey, *Polycyclic Aromatic Compounds*, 2007, **27**, 15–40.

[32] J. Noda, R. Volkamer and M. J. Molina, *Journal of Physical Chemistry A*, 2009, **113**, 9658–9666.

[33] A. W. Birdsall, J. F. Andreoni and M. J. Elrod, *Journal of Physical Chemistry A*, 2010, **114**, 10655–10663.

[34] S. M. Aschmann, J. Arey and R. Atkinson, *Atmospheric Environment*, 2010, **44**, 3970–3975.

[35] A. Wahner and C. Zetzsch, *Journal of Physical Chemistry*, 1983, **87**, 4945–4951.

[36] F. Witte, E. Urbanik and C. Zetzsch, *Journal of Physical Chemistry* , 1986, **90**, 3251–3259.

[37] R. Knispel, R. Koch, M. Siese and C. Zetzsch, *Berichte der Bunsen-Gesellschaft - Physical Chemistry Chemical Physics*, 1990, **94**, 1375–1379.

[38] B. Bohn and C. Zetzsch, *Physical Chemistry Chemical Physics*, 1999, **1**, 5097–5107.

[39] B. Bohn, *Journal of Physical Chemistry A*, 2001, **105**, 6092–6101.

[40] S. Grebenkin and L. Krasnoperov, *Journal of Physical Chemistry A*, 2004, **108**, 1953–1963.

[41] S. Raoult, M. T. Rayez, J. C. Rayez and R. Lesclaux, *Physical Chemistry Chemical Physics*, 2004, **6**, 2245–2253.

[42] R. Koch, R. Knispel, M. Elend, M. Siese and C. Zetzsch, *Atmospheric Chemistry and Physics*, 2007, **7**, 2057–2071.

[43] R. Atkinson, D. Baulch, R. Cox, R. Hampson, J. Kerr and J. Troe, *Journal of Physical and Chemical Reference Data*, 1989, **18**, 881–1097.

[44] D. Smith, C. McIver and T. Kleindienst, *Journal of Atmospheric Chemistry*, 1998, **30**, 209–228.

[45] D. Smith, T. Kleindienst and C. McIver, *Journal of Atmospheric Chemistry*, 1999, **34**, 339–364.

[46] T. Berndt and O. Böge, *Physical Chemistry Chemical Physics*, 2006, **8**, 1205–1214.

[47] C. O. Baltaretu, E. I. Lichtman, A. B. Hadler and M. J. Elrod, *Journal of Physical Chemistry A*, 2009, **113**, 221–230.

[48] J. Zhao, R. Zhang, K. Misawa and K. Shibuya, *Journal of Photochemistry and Photobiology A-Chemistry*, 2005, **176**, 199–207.

[49] A. W. Birdsall and M. J. Elrod, *Journal of Physical Chemistry A*, 2011, **115**, 5397–5407.

[50] P. B. Shepson, E. O. Edney and E. W. Corse, *Journal of Physical Chemistry*, 1984, **88**, 4122–4126.

[51] B. Klotz, I. Barnes, K.-H. Becker and B. T. Golding, *Journal of the Chemical Society - Faraday Transactions*, 1997, **93**, 1507–1516.

[52] T. Berndt, O. Böge and H. Herrmann, *Chemical Physics Letters*, 1999, **314**, 435–442.

[53] R. Atkinson, S. Aschmann and J. Arey, *International Journal of Chemical Kinetics*, 1991, **23**, 77–97.

[54] B. Klotz, I. Barnes and K.-H. Becker, *Chemical Physics*, 1998, **231**, 289–301.

[55] K. P. Wyche, P. S. Monks, A. M. Ellis, R. L. Cordell, A. E. Parker, C. Whyte, A. Metzger, J. Dommen, J. Duplissy, A. S. H. Prevot, U. Baltensperger, A. R. Rickard and F. Wulfert, *Atmospheric Chemistry and Physics*, 2009, **9**, 635–665.

[56] A. R. Rickard, K. P. Wyche, A. Metzger, P. S. Monks, A. M. Ellis, J. Dommen, U. Baltensperger, M. E. Jenkin and M. J. Pilling, *Atmospheric Environment*, 2010, **44**, 5423–5433.

[57] M. J. Elrod, *Journal of Physical Chemistry A*, 2011, **115**, 8125–8130.

[58] N. Nishino, J. Arey and R. Atkinson, *Environmental Science & Technology*, 2010, **44**, 3644–3645.

[59] H. Bethel, R. Atkinson and J. Arey, *Journal of Physical Chemistry A*, 2000, **104**, 8922–8929.

[60] E. Gomez Alvarez, J. Viidanoja, A. Munoz, K. Wirtz and J. Hjorth, *Environmental Science & Technology*, 2007, **41**, 8362–8369.

[61] J. Arey, G. Obermeyer, S. M. Aschmann, S. Chattopadhyay, R. D. Cusick and R. Atkinson, *Environmental Science & Technology*, 2009, **43**, 683–689.

[62] J. F. Hamilton, A. C. Lewis, C. Bloss, V. Wagner, A. P. Henderson, B. T. Golding, K. Wirtz, M. Martin-Reviejo and M. J. Pilling, *Atmospheric Chemistry and Physics*, 2003, **3**, 1999–2014.

[63] J. F. Hamilton, P. J. Webb, A. C. Lewis and M. Martin-Reviejo, *Atmospheric Environment*, 2005, **39**, 7263–7275.

[64] L. P. Thüner, R. G. and J. C. Wenger, *Photolysis of butenedial and 4-oxo-2-pentenal*, CEAM technical report, 2001.

[65] N. L. Ng, J. H. Kroll, A. W. H. Chan, P. S. Chhabra, R. C. Flagan and J. H. Seinfeld, *Atmospheric Chemistry and Physics*, 2007, **7**, 3909–3922.

[66] B. Ervens and R. Volkamer, *Atmospheric Chemistry and Physics*, 2010, **10**, 8219–8244.

[67] R. M. Kamens, H. F. Zhang, E. H. Chen, Y. Zhou, H. M. Parikh, R. L. Wilson, K. E. Galloway and E. P. Rosen, *Atmospheric Environment*, 2011, **45**, 2324–2334.

[68] Y. Zhou, H. F. Zhang, H. M. Parikh, E. H. Chen, W. Rattanavaraha, E. P. Rosen, W. X. Wang and R. M. Kamens, *Atmospheric Environment*, 2011, **45**, 3882–3890.

[69] B. Calpini, F. Jeanneret, M. Bourqui, A. Clappier, R. Vajtai and H. van den Bergh, *Analusis*, 1999, **27**, 328–336.

[70] T. A. Kovacs and W. H. Brune, *Journal of Atmospheric Chemistry*, 2001, **39**, 105–122.

[71] Y. Sadanaga, A. Yoshino, K. Watanabe, A. Yoshioka, Y. Wakazono, Y. Kanaya and Y. Kajii, *Review of Scientific Instruments*, 2004, **75**, 2648–2655.

[72] A. Hofzumahaus, F. Rohrer, K. Lu, B. Bohn, T. Brauers, C.-C. Chang, H. Fuchs, F. Holland, K. Kita, Y. Kondo, X. Li, S. Lou, M. Shao, L. Zeng, A. Wahner and Y. Zhang, *Science*, 2009, **324**, 1702–1704.

[73] S. Lou, F. Holland, F. Rohrer, K. Lu, B. Bohn, T. Brauers, C. Chang, H. Fuchs, R. Häseler, K. Kita, Y. Kondo, X. Li, M. Shao, L. Zeng, A. Wahner, Y. Zhang, W. Wang and A. Hofzumahaus, *Atmospheric Chemistry and Physics*, 2010, **10**, 11243–11260.

[74] F. Holland, U. Aschmutat, M. Hessling, A. Hofzumahaus and D.-H. Ehhalt, *Journal of Atmospheric Chemistry*, 1998, **31**, 205–225.

[75] F. Holland, A. Hofzumahaus, R. Schäfer, A. Kraus and H.-W. Pätz, *Journal of Geophysical Research-Atmospheres*, 2003, **108**, 8246–8268.

[76] A. V. Ivanov, S. Trakhtenberg, A. K. Bertram, Y. M. Gershenzon and M. J. Molina, *Journal of Physical Chemistry A*, 2007, **111**, 1632–1637.

[77] NASA panel for data evaluation, *JPL publication*, 2011, **10-06**, evaluation NO. 17.

[78] D. C. McCabe, T. Gierczak, R. K. Talukdar and A. R. Ravishankara, *Geophysical Research Letters*, 2001, **28**, 3135–3138.

[79] S. Nehr, B. Bohn, H. Fuchs, A. Hofzumahaus and A. Wahner, *Physical Chemistry Chemical Physics*, 2011, **13**, 10699–10708.

[80] S. Nehr, B. Bohn and A. Wahner, *Journal of Physical Chemistry A*, 2012, **116**, 6015–6026.

[81] H. Fuchs, B. Bohn, A. Hofzumahaus, F. Holland, K. Lu, S. Nehr, F. Rohrer and A. Wahner, *Atmospheric Measurement Techniques*, 2011, **4**, 1209–1225.

[82] K. D. Lu, F. Rohrer, F. Holland, H. Fuchs, B. Bohn, T. Brauers, C. C. Chang, R. Häseler, L. Hu, K. Kita, Y. Kondo, X. Li, S. R. Lou, S. Nehr, M. Shao, L. M. Zeng, A. Wahner, Y. H. Zhang and A. Hofzumahaus, *Atmospheric Chemistry and Physics*, 2012, **12**, 1541–1569.

[83] C. Markwardt, *IDL library, http://cow.physics.wisc.edu/ craigm/idl/*, 2010.

[84] H.-J. Andreß, *Saarland University, Open-Access-Library, http://psydok.sulb.uni-saarland.de/volltexte/2004/268/html/surfstat/chi.htm*, 2001.

[85] A. Aluculesei, A. Tomas, C. Schoemaecker and C. Fittschen, *Applied Physics B - Lasers and Optics*, 2008, **92**, 379–385.

[86] T. Kovacs, M. A. Blitz, P. W. Seakins and M. J. Pilling, *Journal of Chemical Physics*, 2009, **131**, 204304.

[87] C. Jain, A. E. Parker, C. Schoemaecker and C. Fittschen, *ChemPhysChem*, 2010, **11**, 3867–3873.

[88] C. M. Mihele and D. R. Hastie, *Geophysical Research Letters*, 1998, **25**, 1911–1913.

[89] H. Fuchs, F. Holland and A. Hofzumahaus, *Review of Scientific Instruments*, 2008, **79**, 084104.

[90] M. Weber, *PhD thesis*, University of Cologne, 1998.

[91] R. Atkinson and J. Arey, *Chemical Reviews*, 2003, **103**, 4605–4638.

[92] MCM, *Master Chemical Mechanism, http://mcm.leeds.ac.uk/MCM/*, 2012.

[93] R. Atkinson, S. Aschmann, J. Arey and W. Carter, *International Journal of Chemical Kinetics*, 1989, **21**, 801–827.

[94] E. Bjergbakke, A. Sillesen and P. Pagsberg, *Journal of Physical Chemistry*, 1996, **100**, 5729–5736.

[95] T. Berndt and O. Böge, *Physical Chemistry Chemical Physics*, 2001, **3**, 4946–4956.

[96] R. Seuwen and P. Warneck, *International Journal of Chemical Kinetics*, 1996, **28**, 315–332.

[97] B. Klotz, S. Sorensen, I. Barnes, K.-H. Becker, T. Etzkorn, R. Volkamer, U. Platt, K. Wirtz and M. Martin-Reviejo, *Journal of Physical Chemistry A*, 1998, **102**, 10289–10299.

[98] N. Moschonas, D. Danalatos and S. Glavas, *Atmospheric Environment*, 1999, **33**, 111–116.

[99] N. Nishino, J. Arey and R. Atkinson, *Journal of Physical Chemistry A*, 2010, **114**, 10140–10147.

[100] B. Klotz, I. Barnes, B. T. Golding and K.-H. Becker, *Physical Chemistry Chemical Physics*, 2000, **2**, 227–235.

[101] R. Cartas-Rosado and M. Castro, *Journal of Physical Chemistry A*, 2007, **111**, 13088–13098.

[102] M. Hoshino, H. Akimoto and M. Okuda, *Bulletin of the Chemical Society of Japan*, 1978, **51**, 718–724.

[103] H. Forstner, R. Flagan and J. Seinfeld, *Environmental Science & Technology*, 1997, **31**, 1345–1358.

[104] M. Huang, W. Zhang, L. Hao, Z. Wang, W. Zhao, X. Gu, X. Guo, X. Liu, B. Long and L. Fang, *Journal of Atmospheric Chemistry*, 2007, **58**, 237–252.

[105] M. Huang, W. Zhang, L. Hao, Z. Wang, L. Fang, R. Kong, X. Shan, F. Liu and L. Sheng, *Journal of Environmental Sciences - China*, 2010, **22**, 1570–1575.

[106] H. Bandow and N. Washida, *Bulletin of the Chemical Society of Japan*, 1985, **58**, 2541–2548.

[107] M. Gery, D. Fox, R. Kamens and L. Stockburger, *Environmental Science & Technology*, 1987, **21**, 339–348.

[108] R. Volkamer, *PhD thesis*, University of Heidelberg, 2001.

[109] J. Z. Yu, H. E. Jeffries and K. G. Sexton, *Atmospheric Environment*, 1997, **31**, 2261–2280.

[110] J. Z. Yu and H. E. Jeffries, *Atmospheric Environment*, 1997, **31**, 2281–2287.

[111] E. S. C. Kwok, S. M. Aschmann, R. Atkinson and J. Arey, *Journal of the Chemical Society - Faraday Transactions*, 1997, **93**, 2847–2854.

[112] H. Bandow and N. Washida, *Bulletin of the Chemical Society of Japan*, 1985, **58**, 2549–2555.

[113] T. Berndt and O. Böge, *International Journal of Chemical Kinetics*, 2001, **33**, 124–129.

[114] D. Grosjean, *Science of the Total Environment*, 1991, **100**, 367–414.

[115] R. I. Olariu, B. Klotz, I. Barnes, K.-H. Becker and R. Mocanu, *Atmospheric Environment*, 2002, **36**, 3685–3697.

[116] T. Berndt and O. Böge, *Physical Chemistry Chemical Physics*, 2003, **5**, 342–350.

[117] C. Coeur-Tourneur, F. Henry, M.-A. Janquin and L. Brutier, *International Journal of Chemical Kinetics*, 2006, **38**, 553–562.

[118] D. Grosjean, *Environmental Science & Technology*, 1985, **19**, 968–974.

[119] R. Atkinson, D. Baulch, R. Cox, R. Hampson, J. Kerr and J. Troe, *Journal of Physical and Chemical Reference Data*, 1992, **21**, 1125–1568.

[120] J. Platz, O. Nielsen, T. Wallington, J. Ball, M. Hurley, A. Straccia, W. Schneider and J. Sehested, *Journal of Physical Chemistry A*, 1998, **102**, 7964–7974.

[121] M. Karl, T. Brauers, H.-P. Dorn, F. Holland, M. Komenda, D. Poppe, F. Rohrer, L. Rupp, A. Schaub and A. Wahner, *Geophysical Research Letters*, 2004, **31**, L05117.

[122] D. Poppe, T. Brauers, H.-P. Dorn, M. Karl, T. F. Mentel, E. Schlosser, R. Tillmann, R. Wegener and A. Wahner, *Chemical Physics Letters*, 2007, **57**, 203–214.

[123] R. Wegener, T. Brauers, R. Koppmann, S. R. Bares, F. Rohrer, R. Tillmann, A. Wahner, A. Hansel and A. Wisthaler, *Journal of Geophysical Research - Atmospheres*, 2007, **112**, D13301.

[124] B. Bohn and H. Zilken, *Atmospheric Chemistry and Physics*, 2005, **5**, 191–206.

[125] B. Bohn, F. Rohrer, T. Brauers and A. Wahner, *Atmospheric Chemistry and Physics*, 2005, **5**, 493–503.

[126] A. Jordan, S. Haidacher, G. Hanel, E. Hartungen, L. Märk, H. Seehauser, R. Schottkowsky, P. Sulzer and T. D. Märk, *International Journal of Mass Spectrometry*, 2009, **286**, 122–128.

[127] T. J. Kelly and C. R. Fortune, *International Journal of Environmental Analytical Chemistry*, 1994, **54**, 249–263.

[128] J. Heland, J. Kleffmann, R. Kurtenbach and P. Wiesen, *Environmental Science & Technology*, 2001, **35**, 3207–3212.

[129] E. R. Crosson, *Applied Physics B-Lasers and Optics*, 2008, **92**, 403–408.

[130] F. Rohrer and D. Brüning, *Journal of Atmospheric Chemistry*, 1992, **15**, 253–267.

[131] W. Schrimpf, K. P. Müller, F. Johnen, K. Lienaerts and J. Rudolph, *Journal of Atmospheric Chemistry*, 1995, **22**, 303–317.

[132] H. Fuchs, S. M. Ball, B. Bohn, T. Brauers, R. C. Cohen, H.-P. Dorn, W. P. Dube, J. L. Fry, R. Häseler, U. Heitmann, R. L. Jones, J. Kleffmann, T. F. Mentel, P. Muesgen, F. Rohrer, A. W. Rollins, A. A. Ruth, A. Kiendler-Scharr, E. Schlosser, A. J. L. Shillings, R. Tillmann, R. M. Varma, D. S. Venables, G. V. Tapia, A. Wahner, R. Wegener, P. J. Wooldridge and S. S. Brown, *Atmospheric Measurement Techniques*, 2010, **3**, 21–37.

[133] M. Hausmann, U. Brandenburger, T. Brauers and H.-P. Dorn, *Journal of Geophysical Research-Atmospheres*, 1997, **102**, 16011–16022.

[134] F. Holland, M. Hessling and A. Hofzumahaus, *Journal of the Atmospheric Sciences*, 1995, **52**, 3393–3401.

[135] C. Sioutas, E. Abt, J. M. Wolfson and P. Koutrakis, *Aerosol Science and Technology*, 1999, **30**, 84–92.

[136] J. T. Jayne, D. C. Leard, X. F. Zhang, P. Davidovits, K. A. Smith, C. E. Kolb and D. R. Worsnop, *Aerosol Science and Technology*, 2000, **33**, 49–70.

[137] F. Rohrer, B. Bohn, T. Brauers, D. Brüning, F. J. Johnen, A. Wahner and J. Kleffmann, *Atmospheric Chemistry and Physics*, 2005, **5**, 2189–2201.

[138] T. Brauers and F. Rohrer, *Easy atmospheric chemistry (Ver.2), http://www2.fz-juelich.de/icg/icg-2/downloads/*, 1999.

[139] M. Karl, *PhD thesis*, University of Münster, 2004.

[140] C. A. Richter, *PhD thesis*, University of Cologne, 2008.

[141] H. Fuchs, H.-P. Dorn, M. Bachner, B. Bohn, T. Brauers, S. Gomm, A. Hofzumahaus, F. Holland, S. Nehr, F. Rohrer, R. Tillmann and A. Wahner, *Atmospheric Measurement Techniques*, 2012, **5**, 1611–1626.

[142] H.-C. Wu, *MSc thesis*, University of Cologne, 2012.

[143] E. U. Emanuelsson, M. Hallquist, K. Kristensen, M. Glasius, B. Bohn, H. Fuchs, B. Kammer, A. Kiendler-Scharr, S. Nehr, F. Rubach, R. Tillmann, A. Wahner, H.-C. Wu and T. F. Mentel, *Atmospheric Chemistry and Physics Discussions*, 2012, **12**, submitted.

[144] D. Johnson, M. E. Jenkin, K. Wirtz and M. Martin-Reviejo, *Environmental Chemistry*, 2005, **2**, 35–48.

[145] S. Nakao, C. Clark, P. Tang, K. Sato and D. Cocker, *Atmospheric Chemistry and Physics*, 2011, **11**, 10649–10660.

[146] K. Sato, A. Takami, Y. Kato, T. Seta, Y. Fujitani, T. Hikida, A. Shimono and T. Imamura, *Atmospheric Chemistry and Physics Discussions*, 2012, **12**, 283–318.

[147] R. Atkinson, D. L. Baulch, R. A. Cox, R. F. Hampson, J. A. Kerr, M. J. Rossi, J. Troe and IUPAC Subcommittee Gas Kinetic Data Evaluation, *Journal of Physical and Chemical Reference Data*, 1999, **28**, 191–393.

[148] G. S. Tyndall, R. A. Cox, C. Granier, R. Lesclaux, G. K. Moortgat, M. J. Pilling, A. R. Ravishankara and T. J. Wallington, *Journal of Geophysical Research - Atmospheres*, 2001, **106**, 12157–12182.

[149] O. J. Nielsen, O. Jorgensen, M. Donlon, H. W. Sidebottom, D. J. O'Farrell and J. Treacy, *Chemical Physics Letters*, 1990, **168**, 319–323.

[150] W. H. Press, S. A. Teukolsky, W. T. Vetterling and B. P. Flannery, *Numerical recipes in C*, Cambridge University Press, 1992.

[151] T. R. Shirley, W. H. Brune, X. Ren, J. Mao, R. Lesher, B. Cardenas, R. Volkamer, L. T. Molina, M. J. Molina, B. Lamb, E. Velasco, T. Jobson and M. Alexander, *Atmospheric Chemistry and Physics*, 2006, **6**, 2753–2765.

[152] J. Q. Mao, X. R. Ren, S. A. Chen, W. H. Brune, Z. Chen, M. Martinez, H. Harder, B. Lefer, B. Rappenglück, J. Flynn and M. Leuchner, *Atmospheric Environment*, 2010, **44**, 4107–4115.

[153] A. S. Hasson, G. S. Tyndall and J. J. Orlando, *Journal of Physical Chemistry A*, 2004, **108**, 5979–5989.

[154] M. E. Jenkin, M. D. Hurley and T. J. Wallington, *Physical Chemistry Chemical Physics*, 2007, **9**, 3149–3162.

[155] T. J. Dillon and J. N. Crowley, *Atmospheric Chemistry and Physics*, 2008, **8**, 4877–4889.

[156] C. R. Usher, A. E. Michel, D. Stec and V. H. Grassian, *Atmospheric Environment*, 2003, **37**, 5337–5347.

[157] A. Metzger, J. Dommen, K. Gaeggeler, J. Duplissy, A. S. H. Prevot, J. Kleffmann, Y. Elshorbany, A. Wisthaler and U. Baltensperger, *Atmospheric Chemistry and Physics*, 2008, **8**, 6453–6468.

Acknowledgements

First and foremost, I wish to express my sincere gratitude to Dr. Birger Bohn without whose support the completion of this thesis would not have been possible and who was always there when I needed advice. His patience is gratefully acknowledged.

I want to thank:

Prof. Dr. Peter Wiesen for accepting the supervision of this thesis for the Bergische Universität Wuppertal,

Prof. Dr. Andreas Wahner for accepting the scientific supervision as second examiner and for providing the opportunity to work at IEK-8 (Forschungszentrum Jülich),

Dr. Theo Brauers, Dr. Hendrik Fuchs, and Dr. Franz Rohrer for numerous inspiring discussions and for providing assistance with numerical simulations,

Mathias Bachner, Dr. Sebastian Broch, PD Dr. Andreas Hofzumahaus, Dr. Frank Holland, and former members of the LIF group at IEK-8 who were significantly involved in the success of this thesis,

The SAPHIR team for operating the chamber and providing data even on Sundays and public holidays,

Dr. Ian Barnes and PD Dr. Andreas Hofzumahaus for proofreading of this thesis,

The Deutsche Forschungsgemeinschaft (DFG) for financial support.

Band / Volume 131
Release of Inorganic Trace Elements from High-Temperature Gasification of Coal
M. Bläsing (2012), XVIII, 145 pp.
ISBN: 978-3-89336-772-6

Band / Volume 132
Rauchgasseitige Korrosion Nickelbasislegierungen für zukünftige 700°C-Dampfkraftwerke
F. Lüttschwager (2012), 145 pp.
ISBN: 978-3-89336-773-3

Band / Volume 133
In-Situ Raman Spectroscopy: A Method to Study and Control the Growth of Microcrystalline Silicon for Thin-Film Solar Cells
S. Muthmann (2012), x, 134 pp.
ISBN: 978-3-89336-774-0

Band / Volume 134
Remote sensing of sun-induced fluorescence for improved modeling of gross primary productivity in a heterogeneous agricultural area
A. Schickling (2012), xvi, 135 pp.
ISBN: 978-3-89336-775-7

Band / Volume 135
Untersuchung der Ladungsträgerkonzentration und -beweglichkeit in mikrokristallinen Siliziumlegierungen mit Hall-Effekt undThermokraft
C. Sellmer (2012), 159 pp.
ISBN: 978-3-89336-778-8

Band / Volume 136
Development of thin film inorganic membranes for oxygen separation
H. J. Moon (2012), XII, 118 pp.
ISBN: 978-3-89336-781-8

Band / Volume 137
Influence of Material and Testing Parameters on the Lifetime of TBC Systems with MCrAlY and NiPtAl Bondcoats
P. Song (2012), V, 126 pp.
ISBN: 978-3-89336-783-2

Band / Volume 138
Strömungsmechanische Modellierung eines Brenngaserzeugungs-systems
F. Scharf (2012), vi, 223 pp.
ISBN: 978-3-89336-784-9

Band / Volume 139
Clouds and aerosol in infrared radiative transfer calculations for the analysis of satellite observations
S. Grießbach (2012), viii, 169 pp.
ISBN: 978-3-89336-785-6

Band / Volume 140
Untersuchung zum Thin Film Low Pressure Plasma Spraying (LPPS-TF) Prozess
A. Hospach (2012), 165 pp.
ISBN: 978-3-89336-787-0

Band / Volume 141
Development of thermal spray processes with liquid feedstocks
A. Guignard (2012), 128 pp.
ISBN: 978-3-89336-788-7

Band / Volume 142
Herstellung uranbasierter Keramiken mittels interner Gelierung zur Konversion trivalenter Actinoiden
H. Daniels (2012), 154 pp.
ISBN: 978-3-89336-794-8

Band / Volume 143
Experimental and numerical studies on solute transport in unsaturated heterogeneous porous media under evaporation conditions
M. Bechtold (2012), xviii, 131 pp.
ISBN: 978-3-89336-795-5

Band / Volume 144
Konzept und Kosten eines Pipelinesystems zur Versorgung des deutschen Straßenverkehrs mit Wasserstoff
D. Krieg (2012), 228 pp.
ISBN: 978-3-89336-800-6

Band / Volume 145
Mechanistic studies on the OH-initiated atmospheric oxidation of selected aromatic hydrocarbons
S. Nehr (2012), viii, 129 pp.
ISBN: 978-3-89336-804-4

Energie & Umwelt / Energy & Environment
Band / Volume 145
ISBN 978-3-89336-804-4

JÜLICH
FORSCHUNGSZENTRUM